# Silicon Photonic Multi-Analyte Sensing System and Surface Plasmon Enhanced Chirality Detection

by

Guangcan Mi

A thesis submitted in partial fulfillment of the requirements for the degree of

Doctor of Philosophy

in

Photonics and Plasmas

Department of Electrical and Computer Engineering
University of Alberta

# Abstract

Optical sensing and measurement technology provides one of the most accurate tools for detecting and characterizing materials. They are robust, can provide a rich amount of information about the analytes, and are amenable to miniaturization and large-scale integration on a chip for certain applications. In this thesis, we develop novel optical sensing and measurement methods for two important applications, namely environmental greenhouse gas monitoring and chiral compound analysis for pharmaceutical and biochemical research.

The first part of the thesis aims to develop an integrated multi-analyte gas sensor on a silicon photonic platform for the parallel detection of $CO_2$ and $H_2$ gas concentrations in the atmosphere. The development of a compact sensor that can measure $CO_2$ gas concentrations at the atmospheric level is motivated by the need for accurate monitoring of greenhouse gas for climate change study. A key contribution of the thesis is to demonstrate a silicon photonic refractometric $CO_2$ sensor based on a novel functional material that can be integrated with other gas sensors on the same chip. A prototype dual-gas sensor chip based on a wavelength-multiplexed microring array was also developed for the simultaneous detection of $CO_2$ and $H_2$ gases. Gas sensing experiments were conducted to evaluate the performance of each sensor in the presence of other analytes, and to address important issues related to multi-analyte sensing environment such as cross-sensitivity. The results obtained and knowledge gained from the study help lay the groundwork for future development of multi-analyte sensor systems on a chip for monitoring greenhouse gases and industrial emissions.

The second part of thesis aims to develop novel ellipsometric methods for measuring the chirality of biochemical compounds. In particular we explore the unique properties of chiral

surface plasmon polaritons for enhancing the detection sensitivity of these methods. The research is motivated by the important role of chirality in governing the biological functionalities of biochemical compounds. Measurement of chirality provides information about molecule conformation, enantiomeric purity or excess, and chiral compound concentrations, which are important in pharmaceutical research and other biomedical fields. The ellipsometric methods developed could offer crucial advantages over existing techniques in terms of accuracy, small sample size and the ability to measure multiple optical quantities in the same setup. In addition, chiral surface plasmon waveguide structures investigated offer promising solutions for realizing chiral sensors on an integrated platform.

# Acknowledgement

I would like to express my sincere gratitude to my supervisor Prof. Vien Van for his support, patience, and encouragement throughout my graduate studies. His guidance helped me in all the time of research and writing of this thesis. This graduate research would not have been possible without his support and immense knowledge. I am also very grateful for the chances of industrial and nanofabrication experiences that Prof. Vien Van have brought to me. I would also like to give thanks to the rest of my supervisory committee members: Prof. Stephane Evoy and Prof. Mojgan Daneshmand for their invaluable support during my PhD program.

My thanks go to Ashok P. Masilamani and Mirwais Aktary for the internship at Applied Nanotools. It has been a treasurable time and experience for me. I must also express my deep gratitude to Cameron Horvath for the countless help and technical input he provided.

I thank my fellow labmates Nanophotoincs Research Lab: Daniel Backman, Alan Tsay, Siamak Abdollahi and Ren Yang for the stimulating discussions, and all the fun we have had.

I would like to acknowledge the staff at the NanoFAB fabrication and characterization center for their training and support to my fabrication work. In particular, many thanks to Les Schowalter, Scott Munro, and Aaron Hryciw for the technical consulting and the knowledge I learned from them, Stephanie Bozic and Glenn Elaschuk for their support in times of need.

Thanks to my best friend, Guoqiang Chen, for all the late night and early morning phone calls that have kept me mentally healthy.

Finally, thanks to my mother for her love and greatness.

# Table of Contents

# List of Figures

# List of Tables

# List of symbols

| | |
|---|---|
| $\Delta\lambda$ | Shift of the resonant wavelength of a microring resonator in pm |
| $I$ | Transmitted light intensity of the microring sensor in W |
| $\Delta I$ | Variation in the transmitted light intensity of a microring resonator |
| $w_g$ | Coupling gap between the microring and the straight waveguide in nm |
| $n_{eff}$ | Effective index of a waveguide |
| $R$ | Radius of a microring resonator in μm |
| $m$ | The resonance mode number of a microring resonator |
| $\Delta\lambda_{\mathrm{FSR}}$ | Free Spectral Range of a microring resonator |
| $\lambda_0$ | Resonance wavelength of a microring resonator |
| $n_g$ | Group index of a waveguide |
| $\lambda$ | Free space wavelength in nm |
| $\Gamma_s$ | Interaction factor |
| $\lambda_{\mathrm{OP}}$ | Operation wavelength in nm |
| $n_i$ | Refractive index of medium *i* |
| $\Delta n_{\mathrm{s}}$ | Chang in the Refractive index of the functional material |
| $\eta_0$ | Free space admittance |

| | |
|---|---|
| $C$ | Analyte concentration |
| LOD | Limit of Detection |
| $\sigma_\lambda$ | Wavelength resolution of microring resonator sensor |
| $t_{90}$ | Time to reach 90% of the steady-state response of the microring sensor |
| $S_\lambda$ | Wavelength sensitivity of microring gas sensor in pm/ppm |
| $S_{\mathrm{RIU}}$ | Effective index sensitivity of microring gas sensor in RIU/ppm |
| $\delta C_{\mathrm{gas}}$ | Limit of Detection of a microring gas sensor |
| $A(\lambda)$ | Absorbance of a material at wavelength $\lambda$ |
| $\varepsilon_{\mathrm{L/R}}(\lambda)$ | Molar absorption coefficient of Left and Right circularly polarized light at wavelength $\lambda$ |
| $L$ | Optical path length of the sample cell |
| $c$ | Molar concentration of the chiral sample |
| $\mathbf{D}$ | Electric induction field vector |
| $\mathbf{B}$ | Magnetic induction field vector |
| $\mathbf{E}$ | Electric field vector |
| $\mathbf{H}$ | Magnetic field vector |
| $E$ | Electric field amplitude |
| $H$ | Magnetic H-field amplitude |

| | |
|---|---|
| $c_0$ | Speed of light in vacuum |
| $\kappa$ | Chirality factor as defined in [1] |
| $g$ | Chirality factor as defined in [2] |
| $\xi$ | Chiral admittance |
| $\mu_c$ | Permeability of a chiral medium |
| $\varepsilon_c$ | Permittivity of a chiral medium |
| $\omega$ | Frequency in rad/s |
| $\chi$ | Normalized chiral admittance (chiral parameter) |
| $\beta$ | Propagation constant along the longitudinal direction |
| $k_0$ | Free space wavenumber |
| $\theta$ | Ellipticity of circular dichroism spectroscopy in degree |
| $\theta_i$ | Incidence angle in degree |
| $r$ | Amplitude reflection coefficient of an interface |
| $t$ | Amplitude transmission coefficient of an interface |
| $R$ | Amplitude reflection coefficient for light reflection from a multilayer structure |
| $[\alpha]_D^{20}$ | Specific rotation of a chiral substance at 20˚C and 589nm in deg·ml/(g·dm) |
| $\theta_c$ | Critical angle of the achiral-chiral interface |

| | |
|---|---|
| $\rho$ | Ellipsometric ratio |
| $\psi$ | Ellipsometric amplitude angle in deg |
| $\Delta$ | Ellipsometric phase angle in deg |
| $P$ | Polarizer angle |
| $A$ | Analyzer angle |
| $\delta\Delta$ | Ellipsometric phase angle difference |
| $\theta_E$ | Input angle of the ellipsometer |
| $\kappa$ | Extinction coefficient |
| $\phi$ | Phase of electric field component |
| **M** | Transfer matrix for an interface |
| **P** | Propagation matrix for an optical medium with length $L$ |
| $\varphi$ | Phase of an electromagnetic planewave |
| $P$ | Degree of polarization |
| Depolarization | Depolarization factor |

# List of abbreviations

| | |
|---|---|
| IR | Infra red |
| SOI | Silicon-on-Insulator |
| OR | Optical Rotation |
| CD | Circular Dichroism |
| NOAA | National Oceanic and Atmospheric Administration |
| PHMB | Polyhexamethylene biguanide |
| NDIR | Non-Dispersive Infrared Spectroscopy |
| Q-factor | Quality factor |
| RIU | Refractive Index Unit |
| LOD | Limit of Detection |
| VASE | Varying Angle Spectroscopic Ellipsometry |
| IPA | Isopropyl Alcohol |
| MFC | Mass Flow Controller |
| LSP | Localized Surface Plasmons |
| SPR | Surface Plasmon Resonance |
| WDM | Wavelength Division Multiplexing |
| MMI | Multi-Mode Interference |

| | |
|---|---|
| VOC | Volatile Organic Compound |
| SNR | Signal-to-Noise Ratio |
| Pd-MRR | Pd-coated Microring Resonator |
| Ref-MRR | Reference Microring Resonator |
| PHMB-MRR | Microring Resonator functionalized with PHMB |
| EBL | Electron Beam Lithography |
| HSQ | Hydrogen Silsequioxane |
| ICP-RIE | Inductively Coupled Plasma Reactive Ion Etching |
| WGM | Whispering Gallery Mode |
| PVD | Physical Vapor Deposition |
| ORD | Optical Rotatory Dispersion |
| KK relation | Kramers-Kronig Relation |
| LP | Linearly Polarized |
| LCP | Left Circularly Polarized |
| RCP | Right Circularly Polarized |
| HC-PCF | Hollow-core Photonic Crystal Fiber |
| UV | Ultra-violet |
| VCD | Vibrational Circular Dichroism |

| | |
|---|---|
| DLR | Differential Linear Reflectance |
| DCR | Differential Circular Reflectance |
| CRDP | Cavity Ringdown Polarimeter |
| VASE | Variable Angle Spectroscopic Ellipsometer |
| PSRA | Polarizer-Sample-Rotating Analyzer |
| PCSA | Polarizer-Compensator-Sample-Analyzer |
| PSCA | Polarizer-Sample-Compensator-Analyzer |
| SPP | Surface Plasmon Polariton |
| LR-SPR | Long Range Surface Plasmon Resonance |
| MOF | Metal Organic Frameworks |
| DI | De-Ionized |
| TMAH | Tetramethyl-ammonium Hydroxide |

# Chapter One.

# Introduction

## 1.1 Research Motivation

Over the past few decades, integrated optic sensors have found application in various disciplines and industries. Unlike mass-sensitive or electrical sensors, optical sensors are capable of more than merely detecting the analyte presence but can also provide information such as chemical composition and bioactivity in addition to its optical properties. The wide selection of materials available allows optical sensors to be tailored for different application requirements, such as in extreme environmental conditions or for in-vivo medical diagnostics. With the advancement in material science and micro/nano fabrication technology, sensors based on integrated photonics and plasmonics have gained increasing interest as low-cost sensing solutions which can provide high throughput, multi-analyte detection and large scale integration on a chip.

This thesis focuses on two optical sensing applications. The first objective is to develop an integrated silicon photonic sensor system for parallel detection of multiple gases for environmental monitoring applications. The second objective is to develop new ellipsometric techniques, including surface plasmon enhanced techniques, for accurate measurement of chiral compounds, with target applications in biochemical research, drug discovery and toxicological analysis. Each of these main objectives will be described in more detail below.

### *1.1.1 Silicon photonic multi-gas sensor on a chip*

Conventional gas sensors are based on infrared (IR) spectroscopy. These sensors tend to be expensive because of the high power lasers required, bulky because of the long optical path lengths

needed for adequate absorption, and difficult to achieve multi-analyte detection due to the wide spread of gas molecular fingerprints over the IR spectrum. Over the past decade, there has been a push within the sensor industry toward multi-functional, cost-effective and portable platforms, with the ultimate goal of achieving a sensing system on a chip. It is also desirable in terms of reduced cost and improved sensor robustness to integrate as much as possible signal conditioning and processing circuitries on the same chip. In this respect, the silicon-on-insulator (SOI) material has emerged as a cost-effective platform for implementing integrated photonic circuits and sensors that can be seamlessly interfaced with CMOS electronics.

In this thesis we propose to exploit the multiplexed sensing capability of integrated photonic refractometric sensors based on microring resonators for multi-gas detection. The challenges in developing such a sensor system include management of multiple sensor signals on a chip, fabrication complexity, and compatibility among different functional materials for different gas analytes. As a step toward addressing these challenges, we aim to demonstrate a silicon photonic sensor chip based on a wavelength-multiplexed microring array for the simultaneous detection of two gases, carbon dioxide and hydrogen. Both of these gases are closely monitored in the gas and energy industry for environmental and safety compliance. In addition, $CO_2$ is an important greenhouse gas whose atmospheric concentration is continuously being monitored for climate change study.

Photonic $CO_2$ gas sensors which can operate at room temperature and in dry air environment have rarely been reported because of the chemical stability of $CO_2$ and the lack of a suitable functional material. One of the main objectives of the thesis is to explore the use of a guanidine-based polymer as a functional material for photonic refractometric $CO_2$ sensors. In particular, we aim to demonstrate that the proposed polymer exhibits reversible refractive index change when absorbing and releasing $CO_2$ gas molecules at room temperature and in dry air condition. The proposed functional polymer will also be used to functionalize an integrated optic sensor based on a microring resonator and demonstrate refractometric sensing of $CO_2$ gas at atmospheric concentration levels.

For achieving multi-gas sensing on a chip, it is also important to investigate the possibility of incorporating different functional materials on different photonic sensor elements on the chip. We will address this issue by developing a procedure for integrating two microring sensors, one for detecting $CO_2$ gas and the other for $H_2$ gas, on a silicon chip. The performance of the prototype

dual-gas sensor will be experimentally evaluated in terms sensitivity, crosstalk, and limit of detection. The results obtained and the knowledge gained from the study will be valuable for future development of fully-fledged sensor systems on a chip for monitoring greenhouse gases and industrial emissions.

### *1.1.2 Development of optical and surface plasmon enhanced techniques for chiral sensing*

Chirality refers to the stereochemical property of a molecule whose mirror images cannot be superimposed on each other, like the left and right hands. The two mirrored molecules, referred to as enantiomers, have the same chemical formula but different three-dimensional structures, which cause them to have different chemical properties and biological functionalities. The importance of chirality and chiral analysis is well acknowledged in clinical and pharmaceutical applications, biochemistry and environmental chemistry [3-5].

Optically, chirality manifests itself in the different ways chiral molecules interact with left and right circular polarized light. Traditionally, two optical detection techniques, polarimetry and circular dichroism spectroscopy, are employed to measure the two types of chirality, optical rotation (OR) and circular dichroism (CD). Since these techniques depend on measurements of chirality-induced changes in either the polarization or optical absorption of light propagating through a chiral sample, long optical path lengths and hence large sample volumes are required to achieve good signal-to-noise ratios. Also, it is difficult to integrate these techniques with other optical characterization tools to measure other optical parameters of the sample such as its refractive index and extinction coefficient.

Ellipsometry is a widely-used optical characterization technique which measures the change in the polarization state of light upon reflection from the sample, providing information on thin film thickness, uniformity, and material refractive index [6-8]. Thanks to its capabilities of real-time monitoring and non-destructive measurement, ellipsometry has shown promising potential in refractometric and affinity biosensing applications [9, 10]. However, the use of ellipsometry for chiral measurement has rarely been reported. Such a measurement can provide important chiroptical information about the functionality of a biochemical compound. In the second part of the thesis, we aim to develop new ellipsometric methods for measuring the chiral parameter of small-volume samples based on reflection from multi-layer dielectric-chiral and metal-chiral structures.

Since naturally-occurring chiral substances have very weak chirality, the biggest challenge in developing a reflection-based ellipsometric method for chiral detection is to improve its sensitivity and reduce the effect of system noise. Here we propose a differential ellipsometric method for measuring the optical rotation of chiral compounds which is robust enough that it can be implemented with a lamp-based light source instead of expensive tunable lasers. We implemented the method in a commercial ellipsometer and demonstrated its application for broadband measurement of the optical rotation dispersion of chiral samples.

Another objective of this part of the thesis is to investigate the unique properties of chiral surface plasmon polaritons existing at a chiral-metal interface, and exploit them for enhancing the sensitivity of ellipsometric chiral measurements. To accomplish this, we will first investigate how the chiral strength influences the propagation characteristics of chiral SPPs at a chiral-metal interface and suggest how to exploit these effects to realize integrated chiral sensors based on plasmonic waveguides. We will then turn our focus to investigate how the excitation of chiral-SPP modes influences the ellipsometric response of light reflection from a multi-layer chiral-metal structure. Two multi-layer structures for exciting chiral SPPs will be analyzed, namely, the Kretschmann and Otto configurations, and their ellipsometric responses will be compared to determine the optimum configuration for achieving SPR-enhanced measurement of the sample chirality. Finally we also aim to investigate the feasibility of implementing such method in a commercial ellipsometer.

## 1.2 Statement of Research Objectives

The research consists of two main parts: (i) development of an integrated silicon photonic sensor system for environmental gas monitoring, and (ii) development of ellipsometric methods for chirality measurement. The specific objectives for each part are described below.

*Development of silicon photonic dual-gas sensor system*

The main objective of this part is to develop a multiplexed silicon photonic sensor system for parallel detection of $CO_2$ and $H_2$ gases. The specific research goals are:

- Explore suitable functional materials for refractometric sensing of $CO_2$ gas at room temperature and in dry air environment

- Develop silicon photonic refractometric gas sensors for atmospheric $CO_2$ gas monitoring applications
- Design a silicon photonic dual-gas sensing system on a chip based on wavelength division multiplexing for parallel detection of $CO_2$ and $H_2$ gases
- Develop processes for selectively functionalizing sensor elements on a silicon chip for different target gas analytes ($CO_2$ and $H_2$)
- Implement the dual-gas sensor and experimentally evaluate its performance for parallel detection of $CO_2$ and $H_2$ gases

*Development of ellipsometric methods for chirality measurement*

The main objective of this research is to develop new ellipsometric methods for measuring the chiral parameter based on reflection from multi-layer dielectric-chiral and metal-chiral structures. The specific research goals are:

- Develop and experimentally demonstrate a broadband ellipsometric method for chiral measurement based on reflection from a dielectric-chiral interface
- Investigate the unique properties of chiral surface plasmon polaritons and their role in enhancing the ellipsometric response of chiral thin films
- Propose and theoretically evaluate surface resonance enhanced ellipsometric methods for measurement of optical rotation and circular dichroism properties of chiral materials
- Experimentally investigate the feasibility of implementing the proposed surface resonance enhanced ellipsometry methods in a commercial spectroscopic ellipsometer

## 1.3 Organization of the Thesis

This thesis is organized as follows. In Chapter 2, we will investigate a guanidine-based polymer for use as a functional material for refractometric sensing of $CO_2$ gas, and develop a silicon photonic $CO_2$ microring sensor based on the new functional material for atmospheric $CO_2$ gas monitoring. The performance of the sensor in terms of sensitivity, limit of detection and selectivity will be experimentally evaluated. In Chapter 3, we will report the design and implementation of a silicon photonic dual-gas sensor for parallel detection of $CO_2$ and $H_2$ gases. Results of sensing experiments performed to evaluate the sensitivity, resolution and crosstalk of the dual-gas sensor will be presented and discussed. In Chapter 4, we will propose a differential

ellipsometric method for chirality measurement based on reflection from a dielectric-chiral interface and demonstrate its implementation in a commercial ellipsometer. Chapter 5 presents our study of the unique properties of chiral surface plasmon polaritons, with a view of how to exploit them for chiral sensing. Surface plasmon resonance enhanced ellipsometric methods for measuring both the optical rotation and circular dichroism of chiral samples will be proposed and analyzed. Preliminary experimental results of our attempt to demonstrate surface plasmon enhanced ellipsometry technique using a commercial ellipsometer will also be presented and discussed. Chapter 6 provides a summary of the thesis and recommends directions for future research.

# Chapter Two.

# A Silicon Photonic Refractometric $CO_2$ Gas Sensor

## 2.1 Introduction

Carbon dioxide is well known as a major contributor to global warming due to the greenhouse effect. The importance of monitoring and reduction of $CO_2$ gas in the atmosphere has been advocated more widely than ever in recent years due to the alarming rate at which atmospheric $CO_2$ level has been increasing. Figure 2.1 shows the growing trend of the global atmospheric $CO_2$ concentration over the past half century as reported by the National Oceanic and Atmospheric Administration (NOAA) [11]. The global average concentration of atmospheric $CO_2$ gas reached 400 ppm in 2015, which is well above the threshold of 350ppm beyond which the effects of climate change are deemed irreversible [12]. The growth rate of atmospheric $CO_2$ level has also shown an increasing trend over the past few decades. According to a recent report in 2016 from NOAA, the warming effect of $CO_2$ in the atmosphere has increased by 50% since 1990 as a direct result of human activities [13]. Given these alarming statistics, an urgent need arises to develop compact, accurate and low-cost $CO_2$ gas sensors that can be efficiently deployed in large-area sensor networks to monitor trends in greenhouse gas concentrations over wide geographic areas.

(a)

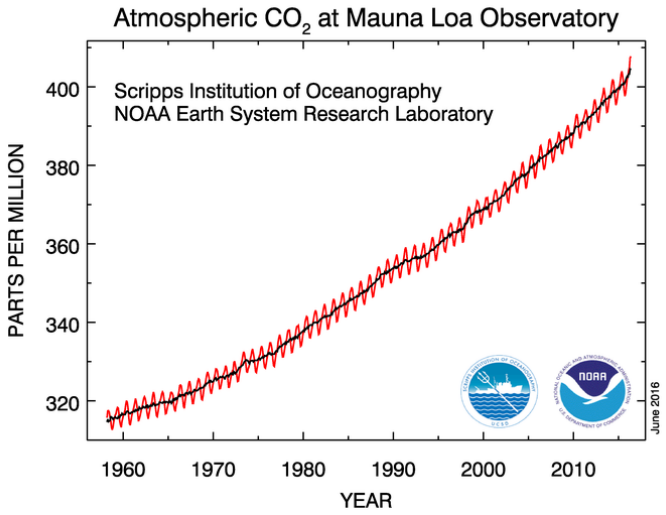


(b)

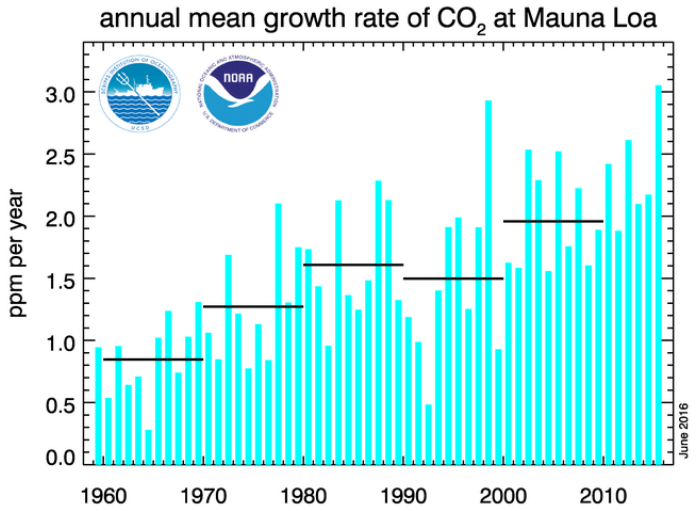


Figure 2.1 (a) Atmospheric $CO_2$ level and (b) its growth rate from 1960 to 2016. Images adopted from [14].

In addition to its effect on climate change, the concentration of $CO_2$ gas in the ambient air which we breathe everyday also has a non-negligible effect on our health, with serious implications to work environment safety [15]. Acute exposure to $CO_2$ of 2-3% can cause shortness of breath, with even more severe symptoms showing at higher concentrations[16]. Long-term exposure to low-level $CO_2$ concentrations also has potential adverse effect on human health; for example, 20-day exposure to $CO_2$ of 850ppm has been shown to correlate to increased lung dead space volume of relative healthy young adults [17]. Therefore, $CO_2$ concentration has been employed as a key indicator of air quality and adequate ventilation in buildings, with a recommended threshold value of 800ppm [18]. Accurate $CO_2$ sensors are commonly integrated in heating, ventilation and air

conditioning systems for the purpose of monitoring indoor air quality. Finally, we note that accurate detection of $CO_2$ gas is important in health science research since $CO_2$ plays an important role in many biological activities.

One of the main objectives of this thesis is to develop compact, accurate and low-cost $CO_2$ gas sensors for environmental monitoring applications. Toward this aim, we propose an integrated optics refractometric sensor solution based on compact silicon microring resonators. A key contribution of our research is to demonstrate a novel functional material based on a guanidine polymer derivative for the specific detection of $CO_2$ gas. In particular, we demonstrate that polyhexamethylene biguanide (PHMB) exhibits reversible refractive index change upon absorbing and releasing of $CO_2$ gas molecules. By functionalizing a silicon microring resonator with a thin PHMB layer, we show that the resonance wavelength of the microring changes with the $CO_2$ gas concentration, thus providing a mechanism for detecting and measuring $CO_2$ gas. Furthermore, the device is capable of direct detection of $CO_2$ gas at atmospheric concentration level, making it suitable for environmental monitoring applications. Compared to other types of $CO_2$ sensors, our refractometric microring sensor has the advantages of operating at room temperature and non-humidified environment.

This chapter is organized as follows. In Section 2.2, we will give a review of existing $CO_2$ gas sensing technologies and discuss the advantages of the proposed refractometric photonic sensing platform. This is followed by a description of the principle of operation of refractometric gas sensors based on microring resonators. Performance metrics of the sensor in terms of sensitivity and limit of detection will also be discussed. In Section 2.4, we will propose a novel functional material based on PHMB for our $CO_2$ sensor and investigate its optical properties in the presence of $CO_2$ gas molecules. We will then describe the fabrication of the silicon photonic sensor chips and the apparatus used for performing $CO_2$ gas sensing experiments. The performance of the sensors will be investigated and discussed in Section 2.6. The chapter will be concluded with a summary in Section 2.7.

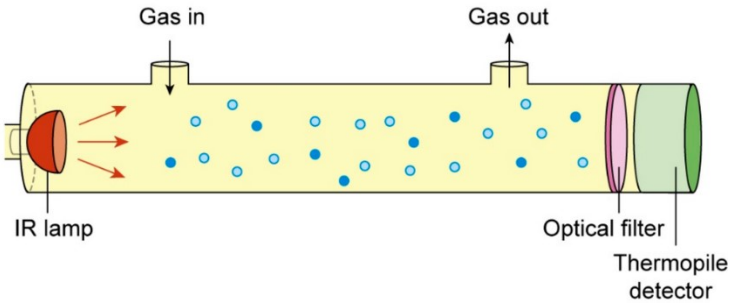


Figure 2.2 Schematic of a NDIR $CO_2$ sensor. Image adopted from [19].

## 2.2 $CO_2$ Gas Sensing Technology

Currently the dominant commercial $CO_2$ sensing technology is Non-Dispersive Infrared Spectroscopy (NDIR). Figure 2.2 shows a schematic of a basic NDIR $CO_2$ sensor. Broadband infrared light from an IR lamp is transmitted through a gas chamber with a typical path length ranging from several centimeters to decimeters. The bandpass filter transmits light around the 4.26μm wavelength, which is the signature absorption band of $CO_2$. The light intensity recorded by the photodetector thus depends on the $CO_2$ concentration and the optical path length. Performance improvement of NDIR sensors has been achieved by biasing the output with a reference signal created using a reference beam with a different optical path length [20], and/or a reference wavelength in the non-absorbing band of $CO_2$ [21]. State-of-the-art NDIR sensors can detect $CO_2$ concentrations down to 10ppm but they tend to be bulky due to the large apparatus required to achieve long optical path lengths for adequate signal absorption [22]. Furthermore, for multi-gas sensing, the wide spread of gas molecular fingerprints over the IR spectrum means that multiple wavelength sources are required, which increases cost and presents impediment to miniaturization and integration.

An alternative $CO_2$ sensing technology that is widely used is electrochemical sensors, which detect reversible resistance or capacitance changes in metal oxides and metal carbonates such as CaO [23], $BaCO_3$ [24], $La_2O_3$ [25] when exposed to $CO_2$ gas. However, activation of the metal oxides typically requires heating the functional material to high temperatures (200-500°C), rendering these sensors unsuitable for room-temperature operation [26] and integration with other sensing technologies for multi-gas detection. Another type of $CO_2$ sensors employs fluorescent dyes whose optical properties are sensitive to changes in the pH level caused by the formation of $HCO_3^-/CO_3^{2-}$ upon $CO_2$ absorption. These fluorescence sensors are widely used in in-vivo blood

gas sensing [27] and the food industry [21, 28], but are prone to photo bleaching which reduces the sensor lifetime.

Recently, integrated photonic refractometric sensors have emerged as a promising technology for the development of compact, high-throughput multi-analyte sensor systems. Generally speaking, a refractometric gas sensor consists of an optical waveguide device whose optical mode is perturbed due to the presence of an analyte in the surrounding medium. Such perturbation may be detected as a change in the absorption/loss of a transmitted optical signal, or a shift in the resonance frequency of an optical cavity. Microring resonators are one of the most widely-used photonic structures for integrated optical sensors. They offer competitive resolution and sensitivity even in undesirable working conditions by virtue of their extremely high quality factor (Q-factor) and hence lengthened interaction path. The wavelength multiplexing capability also makes microring resonators an ideal candidate for multi-analyte sensing, and their micron-scale dimensions offer the advantages of compact sensor size, minimum sample volume, and easy implementation of multiplexed or distributed sensing networks. Optical microring sensors can also be easily integrated with other sensing mechanisms including absorption spectroscopy and fluorescence spectroscopy.

A microring sensor translates the index change caused by an analyte into a shift in the resonance frequency, or a variation in the transmitted light intensity. To achieve specificity, the microring resonator is coated with a functional material, which exhibits a change in its optical properties upon interaction with a specific target analyte. Refractometric gas sensors based on microring resonators have been reported for chemically-active gas species such as volatile organic compounds [29]. A group from Ghent University reported ammonia [30] and ethanol vapor sensors [31] by coating microring resonators with thin films of target selective materials. Another group in Cornell University exploited the enhanced electric field in slot waveguides to improve the sensitivity of gas detection, demonstrating a large interaction factor of 64% and device sensitivity of 490nm/RIU (refractive index unit) with a microring Q-factor of 5000 [32]. However, integrated photonic refractometric sensors for $CO_2$ gas have not been reported to date, due to the lack of a suitable functional material.

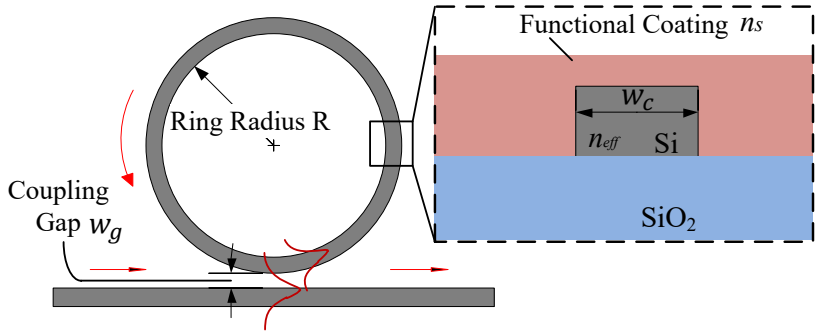


Figure 2.3. Schematic of an optical gas sensor using a microring resonator.

## 2.3 Principle of Operation of a Microring Refractometric Gas Sensor

A basic microring sensor consists of a microring resonator, which is formed by bending an integrated optical waveguide into a circular loop of radius *R*. A schematic of a microring resonator is shown in Figure 2.3. Light is coupled into and out of the microring cavity by evanescent wave coupling between the microring waveguide and a straight waveguide placed in close proximity. The coupling gap $w_g$ between the microring and the straight waveguide determines the coupling strength. Resonances in the microring cavity occur at wavelengths λ satisfying the condition

$$2\pi R = m\lambda / n_{eff} \,, \tag{2.1}$$

where $n_{eff}$ and $m$ are the effective index of the microring waveguide and the resonance mode number, respectively. At each discrete resonance wavelength, light circulating in the ring constructively interferes with itself, resulting in a buildup of light intensity in the resonator. The transmitted signal in the straight waveguide exhibits a corresponding sharp transmission drop. The wavelength separation between two adjacent resonances is called the Free Spectral Range (FSR) of the microring and is given by

$$\Delta\lambda_{\mathrm{FSR}} = \frac{\lambda_0^2}{2n_g \pi R} \tag{2.2}$$

where $n_g = n_{eff} - \lambda \partial n_{eff} / \partial\lambda$ is the group index.

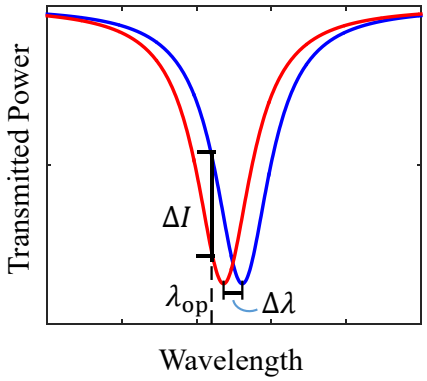


Figure 2.4 Microring resonance shift due to index perturbation caused by an analyte. The blue curve represents the initial resonance spectrum of the microring sensor. Upon absorption of the target gas molecules, the resonance is shifted by Δλ and represented by the red curve.

Equation (2.1) indicates that the resonance wavelength depends on the effective index of the microring waveguide, which can be modified by the presence of an analyte localized near the waveguide surface. For gas sensing applications, the microring waveguide is covered with a layer of a functional material that is sensitive to the target gas, as shown in Figure 2.3. The role of the functional layer is similar to that of the ligand monolayer in biochemical sensors. It selectively absorbs target gas molecules, which cause a change in the refractive index in the cladding layer near the waveguide surface. This in turn causes a shift in the resonance spectrum of the microring that is proportional to the analyte concentration. The translation from the analyte concentration into a shift in the waveguide effective index is called sensor transduction. This index shift can be detected by either tracking a particular resonance wavelength, or by measuring the change in the output light intensity at a fixed wavelength $\lambda_{op}$ located near the resonance, as depicted in Figure 2.4. This measurement is called sensor interrogation.

Suppose an analyte of a certain concentration causes an index change $\Delta n_s$ in the functional layer, the resulting effective index change of the microring waveguide is given by $\Delta n_{eff} = \Gamma_s \Delta n_s$, where $\Gamma_s$ is the interaction factor. The interaction factor represents the fraction of light in the functional layer and determines the strength of the interaction between the optical mode and the functional material [32, 33]. We can determine the interaction factor from the formula

$$\Gamma_s = \frac{\eta_0 n_s \int_s |\mathbf{E}|^2 dA}{\int_\infty (\mathbf{E} \times \mathbf{H}^*)\bullet} \quad , \tag{2.3}$$

where **E** and **H** are the electric and magnetic field distributions of the waveguide mode, $n_s$ is the index of the functional layer, $\eta_0$ is the free space admittance and $\hat{z}$ in the unit vector in the propagation direction. The integral in the numerator is calculated over the area of the functional layer. Taking the total derivative of Equation (2.1) with respect to the wavelength and index changes, we obtain

$$0 = \partial\left(\frac{n_{eff}}{\lambda}\right)_{\lambda}\Delta\lambda + \partial\left(\frac{n_{eff}}{\lambda}\right)_{n_{eff}}\Delta n_{eff} = (-\frac{n_{eff}}{\lambda_{res}^2} + \frac{\partial n_{eff}}{\partial\lambda})\Delta\lambda + \frac{\Delta n_{eff}}{\lambda_{res}}. \tag{2.4}$$

From the above expression, we solve for the resonance wavelength shift due to the index change $\Delta n_s$ in the functional material layer to get

$$\Delta\lambda = \frac{\lambda_{res}}{n_{eff} - \partial n_{eff}/\partial\lambda}\Delta n_{eff} = \frac{\lambda_{res}}{n_g}\Delta n_s\Gamma_s. \tag{2.5}$$

In practice, the sensor is calibrated by determining the direct relationship between the analyte concentration ($C$) and the resonance wavelength shift $\Delta\lambda$ (at a fixed temperature). This relationship is typically nonlinear, although over a small range of concentrations it may be approximated by a linear curve in order to simplify measurement readout.

When a microring sensor is used to detect a target gas at a certain concentration, the transmitted power measured at an operation wavelength $\lambda_{op}$ will be changed by $\Delta I$ due to the shift of the resonance spectrum, as indicated in Figure 2.4. The corresponding resonance wavelength shift can be calculated by

$$\Delta\lambda = \frac{\partial\lambda_{op}}{\partial I}\Delta I. \tag{2.6}$$

where the slope $\partial\lambda_{op}/\partial I$ is calculated from the resonance curve at the operation wavelength. Compared to the wavelength interrogation method, the intensity interrogation technique can provide real-time readout of sensor measurements and is much simpler to implement since it does not require the use of a spectrometer either on-chip or off-chip.

The performance of a sensor is usually evaluated by two metrics, sensitivity and limit of detection. These metrics are described below for a microring sensor.

*Sensitivity*

The sensitivity of a microring sensor is defined as $S = \partial\lambda/\partial n_s = \lambda_{res}\Gamma_s/n_g$, which specifies how much the resonance spectrum moves due to a change in the cladding index. The sensitivity strongly depends on the interaction factor $\Gamma_s$ of the optical mode with the sample, as indicated in Equation (2.5) by $\Gamma_s$, and can thus be enhanced by increasing the fraction of the optical mode interacting with the functional layer [34]. In the particular application of gas sensing, the sensitivity also depends on the ability of the functional material to bind to gas molecules, which determines the relationship between the refractive index change $\Delta n_s$ to the gas concentration.

*Limit of Detection*

Another important performance metric of a sensor is the limit of detection (LOD), which specifies the smallest change in the analyte concentration that can be measured above the noise uncertainty of the system. The LOD is defined by the ratio of the sensor resolution $\sigma_\lambda$ to the sensitivity *S*: LOD = $\sigma_\lambda/S$, where the sensor resolution represents the smallest resonance wavelength shift that can be accurately and repeatedly measured [34]. Various noise sources affecting a sensor's LOD include light source fluctuations, temperature fluctuations, and detector noise. Interference and referencing techniques can be employed to reduce noise influence. For microring sensors which rely on measurement of the magnitude of the wavelength shift, the LOD is also limited by the spectral resolution of the wavelength measurement system, e.g., the frequency resolution of the optical spectrum analyzer or the accuracy of the tunable wavelength source. In general, high-Q resonators give low LOD since the resonance wavelength can be more accurately determined.

## 2.4 A New Functional Material for Refractometric $CO_2$ Sensing

As discussed in Section 2.1, the selection of a suitable functional material is an important step in the design of integrated optics refractometric gas sensors. While a functional material provides sensor selectivity to the target gas and determines the sensitivity of the device, it may also impose constraints on the sensor operation conditions, for example, requiring high temperature or humidified environment, which may render the sensor unsuitable for certain applications. For example, electrochemical $CO_2$ sensors using metal oxides requires elevated operation temperatures to activate the functional material. Refractometric $CO_2$ sensors using other functional materials

have also been reported; however, they typically require a humidified gas environment to operate. For example, a fiber Bragg grating sensor was reported in [35] which employs polyallylamine-amino-carbon nanotubes for detecting $CO_2$ at fairly large concentrations, in the 1000 – 4000 ppm range, under a constant relative humidity of 47%. A surface plasmon resonance sensor functionalized with a polymer blend was also reported in [36] for detecting dissolved and humidified gaseous $CO_2$. Although a low detection limit of 10ppm was reported for the 150 – 1500 ppm range, the sensor showed no response to dry gas mixtures with $CO_2$, rendering it unsuitable for environmental gas monitoring. The prerequisite of humidity also presents challenges to the integration of these sensing technologies with other gas sensors with different functional materials and operating conditions.

For environmental gas monitoring applications, it is desirable that the sensor can operate at room temperature and in dry air condition. We have identified a guanidine-based polymer called PHMB for $CO_2$ detection which satisfies the above requirements and also has the advantages of ease of fabrication and integration with other functional materials. PHMB is commonly used as a safe disinfectant and antiseptic and can also be found in contact lens solutions [37]. It belongs to a class of guanidine derivatives which have been known to function in both solution and solid states to reversibly bind with $CO_2$ gas molecules. Figure 2.5 shows the chemical structures of PHMB and general guanidines. These compounds share the common chemical structure of $(R^1R^2N)(R^3R^4N)C{=}N\text{-}R^5$, which reacts readily with $CO_2$ molecules through a simple base-acid interaction of two amine functional sites and one $CO_2$ molecule without requiring catalysis by heat or humidity [38]

$$2R_2NH + CO_2 \rightleftarrows \quad {}^{+}_{2} + R_2NCOO^{-}. \tag{2.7}$$

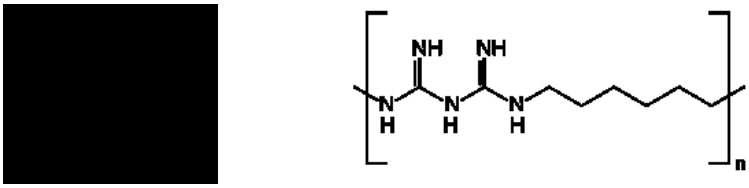


Guanidine PHMB

Figure 2.5 Chemical structures of general Guanidine and PHMB.

It is this reactivity with $CO_2$ which makes guanidine derivatives very useful for developing $CO_2$ absorbent for carbon capture and storage technology [39]. Recently, PHMB was also used as a transducer coating in a capacitive ultrasonic sensor [40], which detects the mass-load change of the functional layer caused by $CO_2$ absorption. However, the use of PHMB for photonic refractometric sensing has not been investigated before since the effect of $CO_2$ absorption on the refractive index of the polymer has not been studied. One of the main objectives of our work is to investigate the change in the optical property of PHMB when exposed to $CO_2$ gas, and evaluate its suitability as a functional material for refractometric sensing of $CO_2$.

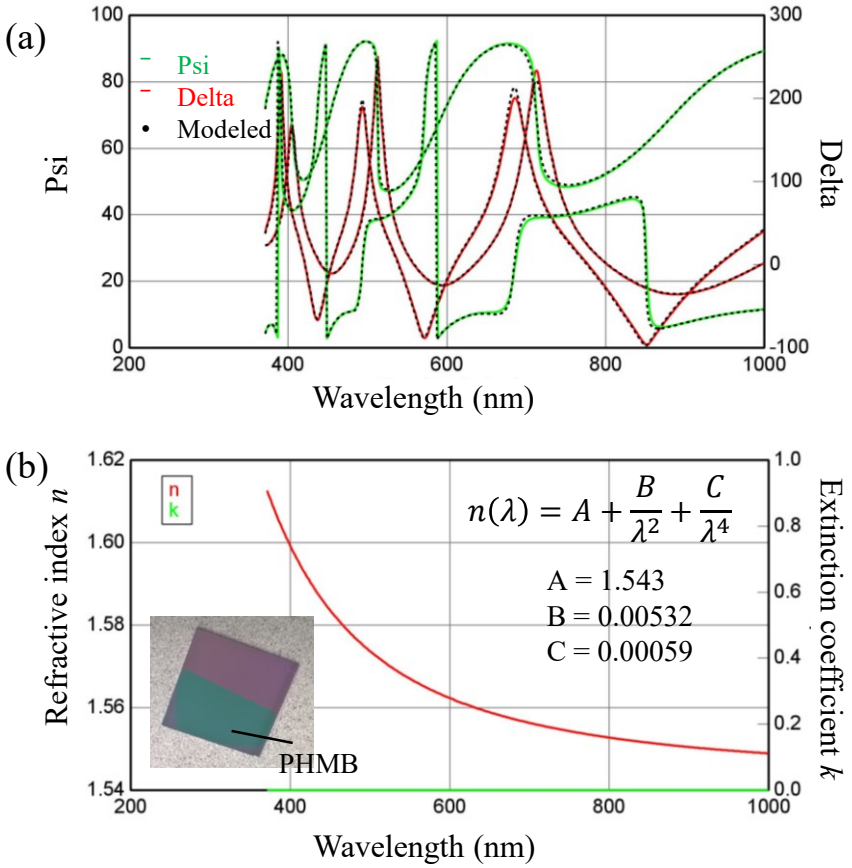


Figure 2.6 (a) VASE data (ellipsometric angles ψ and Δ) of PHMB thin film coated on a test chip measured at incidence angles of 65˚ and 75˚. (b) Refractive index (red curve) and extinction coefficient (green curve) of PHMB thin film vs. wavelength. The inset picture shows the test chip partially coated with PHMB thin film.

We acquired the PHMB polymer from Canada Colors and Chemicals Ltd. as a water solution of 20% (wt%). The polymer can be applied to a chip simply by spin-coating or ink-jet printing, which greatly simplifies the functionalization process. We first characterized the refractive index of PHMB thin films as a function of wavelength using Varying Angle Spectroscopic Ellipsometry (VASE). We spin-coated a test chip with PHMB and removed the polymer layer from one side of the chip for thickness measurement by washing it with DI-water. An optical image of the chip is shown in Figure 2.6(b). Using an AlphaQ profilometer, we measured the polymer thickness to be 303nm. Next we performed VASE measurements of the PHMB film with an M-2000V Ellipsometer (J. A. Woollam Inc.) over the 400-1000nm wavelength range at incidence angles of 65˚ and 75˚. The wavelength scans of the ellipsometric angles Ψ and Δ are shown in Figure 2.6(a). Using the CompleteEase software (J. A. Woollam Inc.) along with the measured polymer thickness value, we computed the refractive index of the PHMB and fitted its wavelength dependence with a Cauchy model [41]

$$n_s(\lambda) = A + \frac{B}{\lambda^2} + \frac{C}{\lambda^4}, \tag{2.8}$$

where $A = 1.543$, $B$ =0.00532, and $C = 0.00059$. Figure 2.6(b) plots the refractive index of the PHMB thin film vs. wavelength. We obtain $n_s = 1.56$ at 632nm wavelength and by extrapolating the data using the Cauchy model, determined $n_s = 1.54$ at 1550nm. We also find that the polymer has negligible optical absorption over the wavelength range of measurement.

The thickness of the PHMB layer can be controlled by varying the spin speed as well as the solution concentration. For example, we obtained a thickness of 240nm with a 3000 RPM spin speed using a 15% PHMB water solution. For thickness less than 150nm, Isopropyl Alcohol (IPA) was added to the solution to obtain evenly coated polymer film. IPA is a more evaporative solvent which results in thinner films with the same volume concentration using the spin-coating technique.

### 2.5 Silicon Photonic Microring $CO_2$ Gas Sensor

In this section, we investigate the use of PHMB as a functional layer for a silicon microring $CO_2$ gas sensor. We will first describe the microring device and the functionalization procedure for the sensor in Section 2.5.1. The apparatus for performing $CO_2$ gas sensing experiments will be described in Section 2.5.2, with the experimental results discussed in Section 2.6.

### *2.5.1 Silicon microring device*

We have designed the silicon microring device with on-chip grating couplers, and employed the foundry service of the Washington Nanofabrication Facility to fabricate the bare sensor chip. The sensor chip used a silicon-on-insulator substrate consisting of a 300nm-thick silicon layer on a 1μm-thick $SiO_2$ buffer layer. The silicon waveguides had a nominal width of 450nm and were designed to operate in the fundamental TE mode around the 1550nm wavelength. The microring resonators had a radius of 10μm and a coupling gap of 170nm to the straight waveguide, as shown in Figure 2.7(b). A schematic of the cross-section of the microring waveguide with a functional layer is shown in Figure 2.7(a). Grating couplers etched on the silicon chip were used for coupling light between the silicon waveguides and optical fibres. The focusing grating couplers were designed for TE polarization with 600nm grating period, 50% duty cycle, 100nm etch depth and 12.5μm focal length. The couplers were spaced a distance of 250μm apart to match with the channel spacing of the fiber array block (from Oz Optics). The resonance spectrum of the microring resonator near the 1550nm wavelength was measured before functionalization and is shown by the black curve in Figure 2.8. We observe a splitting of the resonance dip for the bare microring resonator, which resulted from the coupling between the forward-propagating mode in the microring and the backward-propagating mode caused by scattering from waveguide surface roughness [42, 43].

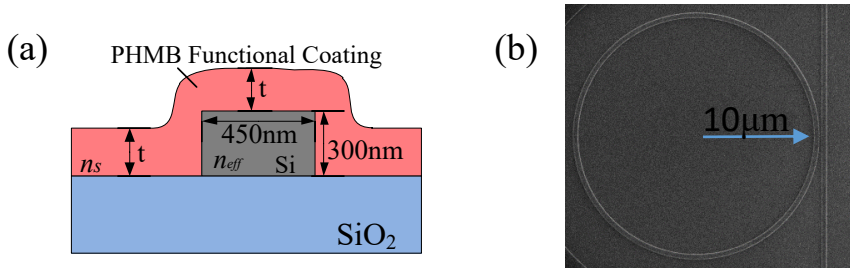


Figure 2.7. (a) Cross-section view of silicon microring with a PHMB functional layer coating over the microring waveguide. (b) SEM image of the silicon microring resonator

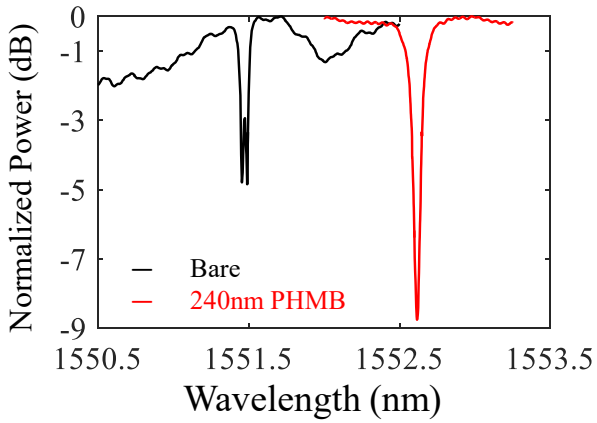


Figure 2.8 Resonance spectrum of the fabricated microring device before and after functionalization.

Next, we functionalized the microring by spin-coating a 15% PHMB solution at 3000RPM onto the silicon device chip. The chip was then baked for 5minutes at 120˚C, which is below the decomposition temperature of PHMB [44]. The thickness of the PHMB layer was measured using a Filmetrics reflectometer to be 240nm. After the functionalization, we bonded the sensor chip using a UV-curable epoxy to a pigtailed fiber array block. The fiber-to-grating coupler alignment was done using the alignment stage shown in Figure 2.9. Optimum coupling was achieved by maximizing the output power with the input laser light at a fixed wavelength. For the sensor chip with a 240-nm thick PHMB coating, the alignment was performed at the 1550nm wavelength, which is near the microring resonance used in the sensing experiments. After functionalization and packaging, the resonance spectrum of the microring was measured again in the ambient lab environment. The result is shown by the red curve in Figure 2.8. We observe that the resonance spectrum of the microring has been slightly red-shifted due to the presence of the PHMB functional layer. In addition, the microring exhibited a deeper extinction at resonance due to better matching between the coupling and loss (critical coupling condition). The quality factor of the resonator is determined to be about 19,000.

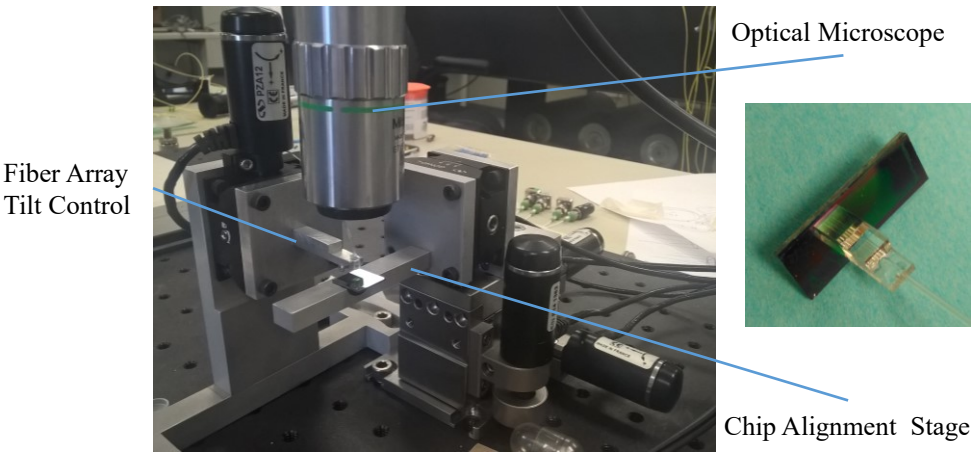


Figure 2.9 A picture of the setup used to perform coupling alignment of the fiber array to the fiber grating couplers on the sensor chip [courtesy of Applied Nanotools Inc.]. Also shown is the sensor chip bonded to a fiber block array.

### *2.5.2 Sensing experimental setup*

A schematic of the gas sensing experiment is shown Figure 2.10. The setup consisted of a gas supply system, a gas testing chamber, and an optical measurement system. Each of these components is described below.

For the gas supply, we acquired gas tanks containing 99.998% $N_2$ gas (primary standard) and $CO_2$ gas of 1% balanced in $N_2$ (certified standard), respectively, from Praxair Canada Inc. Gas flow from each tank is regulated by a separate mass flow controller (MFC, Alicat Scientific Inc.). The MFC controlling $N_2$ carrier gas has a tuning capacity of up to 1SLPM (square litre per minute) with 10sccm increment, while the MFC controlling the $CO_2$ gas has a tuning capacity of up to 500sccm with 1sccm increment. The gas sensing chamber shown in Figure 2.10 was manufactured using Teflon by the machine shop at the University of Alberta. The chamber has a relatively large volume of about $1dm^3$, with gas inlet and exhaust ports placed at the top of the chamber. A plastic plate is placed between the O-rings embedded in the chamber body and the bottom lid to hold the sensor chip and provide sealing of the gas chamber.

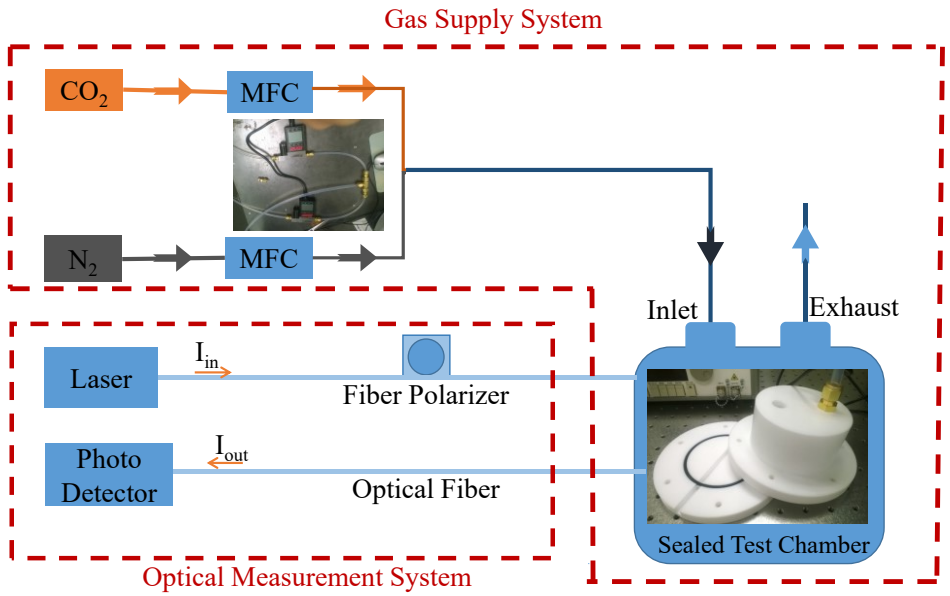


Figure 2.10 Schematic of the experimental setup for $CO_2$ gas sensing (MFC = mass flow controller). Inset pictures show the Teflon gas chamber and the MFC flow connection.

The optical measurement system consists of a CW tunable laser source (SANTEC TSL-210V), a fiber polarization controller to maximize light coupling to the sensor through the on-chip grating coupler, photodetector and power meter to record the sensor output power, and a computer with a LabView program to synchronize the laser and power meter. This experimental setup can be used to perform both steady-state measurements under various gas conditions and transient measurements of the sensor output power at a fixed wavelength during a series of gas flow events.

## 2.6 $CO_2$ Gas Sensing Experiments

### *2.6.1 Demonstration of refractometric $CO_2$ sensing with PHMB*

In this section, we report the results of $CO_2$ gas sensing experiments to demonstrate the feasibility and investigate the performance of refractometric microring sensors based on PHMB. Most of the experiments involved monitoring the transmitted power of the microring resonator at a fixed wavelength to detect shifts in the resonance spectrum caused by the presence of $CO_2$ gas. A typical sensing experiment consists of the following steps:

1) **Precondition**. Before each experiment, the sealed gas chamber with the packaged sensor chip is preconditioned for 10 minutes by flooding it with the carrier gas ($N_2$

gas). The chamber seal is checked by closing the outlet valve briefly and observing an increase in the chamber pressure as indicated by the MFC controlling $N_2$ gas. With the input light set to TE polarization, an initial resonance spectrum of the microring is collected as the reference spectrum, which will be later used to relate the transmitted power changes to relative wavelength shifts. Next, the laser is tuned to the operating wavelength, which is set at the point of half-maximum transmission of the resonance curve, and left to be stabilized for several minutes.

2) **Acquiring the baseline of sensor response**. With the power meter recording the microring transmitted power at the fixed operating wavelength, the gas sensing experiment begins with a 3-minute flow of carrier $N_2$ gas into the chamber to obtain the sensor baseline.
3) **Gas sensing cycle**. Subsequently, $CO_2$ gas at a certain concentration level is introduced into the gas chamber for 3 minutes, followed by a 3-minute flow of the carrier gas ($N_2$) to regenerate the PHMB layer.
4) **Multi-cycle experiment**. Steps 2 and 3 are repeated for the same or different gas concentrations if multiple sensing cycles are needed. Various $CO_2$ gas concentrations are obtained by changing the flow rate ratio between $CO_2$ gas (1% in $N_2$ carrier gas) and $N_2$ gas. The total gas flow rate is maintained at 200sccm for all the experiments, except those requiring small $CO_2$ concentrations. For example, the smallest $CO_2$ concentration that can be obtained is 50ppm, where the flow rates are set at 1sccm $CO_2$ and 200sccm $N_2$, which is limited by the tuning capability of the MFCs.

The microring sensor chip used in the experiments was designed and fabricated as described in Section 2.3.1 and functionalized with a 240nm-thick layer of PHMB. The initial resonance spectrum around the 1.55μm wavelength after preconditioning of the sensing chamber is shown by the black curve in Figure 2.11. From the measured spectrum we obtained a loaded Q factor of $1.92\times10^4$ (±2%) for the microring resonator. We then tuned the wavelength of the laser to the half-max transmission point, introduced 0.5% $CO_2$ gas flow into the chamber and monitored the

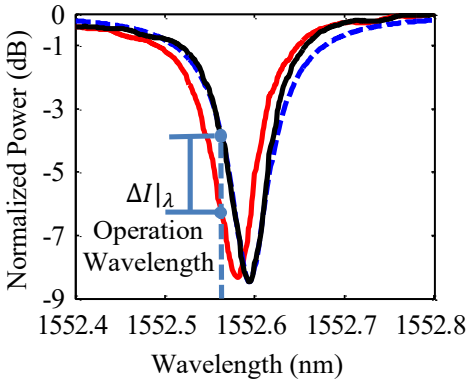


Figure 2.11. Measured resonance spectrum of the functionalized microring resonator. Black curve is the initial spectrum in $N_2$ gas; red curve is the spectrum in the presence of 0.5% $CO_2$ gas concentration. The blue dashed line is the resonance curve fit, which is used to relate the transmitted powers to relative wavelength shifts.

transmitted power for 2 minutes until it had stabilized. The new resonance spectrum in the presence of $CO_2$ gas was recorded and is shown by the red curve in Figure 2.11. The loaded Q factor was determined to be $1.87\times10^4$ (±2%), which is the same as the Q factor of the initial spectrum within experimental uncertainty. Thus the two resonance spectra can be considered to be identical except for a small blue shift in the resonance wavelength. This indicates that around the 1.55μm wavelength, $CO_2$ absorption causes a decrease in the refractive index of the PHMB polymer while having negligible effect on the optical absorption. The exact physical mechanism causing this change in the refractive index of PHMB still needs to be determined, but from the behaviours of similar polymers upon $CO_2$ absorption, we can hypothesize that this index change can be explained in terms of a redistribution of the electron density of the polymer's repeating units due to the binding of $CO_2$ molecules, which results in a change in its polarizability and therefore, its refractive index.

Having confirmed that the PHMB functional layer does respond optically to $CO_2$ gas, we next investigated the sensor response to varying $CO_2$ concentrations, ranging from 50ppm to 5000ppm. For this experiment, we fixed the wavelength of the input laser light at 1552.545nm, which is near the point of steepest slope on the left shoulder of the resonance dip, as indicated in Figure 2.11. Three-minute flows of $CO_2$ gas of varying concentrations were then introduced into the gas chamber, each followed by a 3-minute purging period with $N_2$ gas. Figure 2.12 shows the transmitted power of the microring as a function of time, which consists of a train of inverted pulses in response to input pulses of varying $CO_2$ gas concentrations. We observe that upon

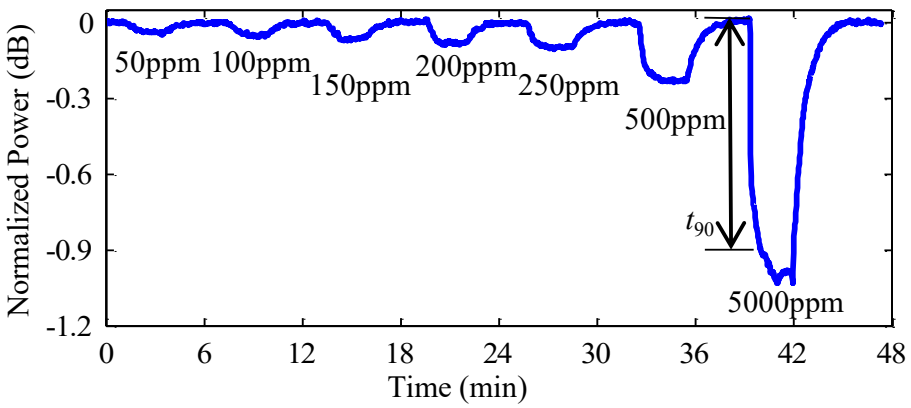


Figure 2.12 Transmitted power of the microring sensor at a fixed wavelength, in response to 3-minute pulses of $CO_2$ gas flow with various concentrations. The sensor is regenerated by purging the chamber with $N_2$ gas for 3 minutes after each $CO_2$ cycle. The transmitted power response was normalized to the baseline power (in $N_2$ gas).

exposure to $CO_2$ gas, the transmitted power abruptly decreases, which corresponds to a blue shift of the microring resonance spectrum, and after some time reaches an equilibrium stage of stable response. When the $CO_2$ gas flow is turned off and the chamber is purged with $N_2$, the power rises back to the baseline as $CO_2$ is released from the PHMB layer and the functional layer is being regenerated. The height of the output inverted pulse increases with increasing $CO_2$ concentration, indicating a larger blue shift in the resonance wavelength of the microring. Also, since the resonance spectrum is unchanged by the absorption of $CO_2$ except for a wavelength shift, the return of the transmitted power to the baseline during the regeneration period proves that the refractive index change in the PHMB functional layer is reversible. This regenerability without requiring heating is an advantage of PHMB over other functional materials such metal oxides [45]and metal carbonate [24].

The fall time $t_{90}$ of the inverted pulse, which characterizes the time required for the sensor to reach 90% of the steady-state response, is around one minute. This fall time primarily depends on the time required by the PHMB layer to reach equilibrium after absorbing or releasing gas molecules under a constant $CO_2$ flow. It is also limited by the gas chamber volume and can be decreased by using a smaller chamber. We also calculated the recovery time (the output power returning from 90% of steady-state response to baseline) to be 2.45mins, 2.9mins, 3.5mins for 50ppm, 500ppm and 5000ppm respectively. These recovery times are about three times of that required to refresh the chamber gas with $N_2$ (~1min at flow rate of 200sccm and ~200$cm^3$ chamber volume). The recovery time is dominated by the regeneration of the functional material from

exposure to different $CO_2$ gas concentrations. The recovery time is longer at higher $CO_2$ concentration since it takes longer to remove $CO_2$ molecules immobilized at binding sites occurring deeper inside the PHMB film.

### *2.6.2 Performance of silicon microring $CO_2$ gas sensors*

In this section, we evaluate the performance of silicon microring $CO_2$ gas sensors by determining their sensitivity and limit of detection. These performance metrics will also be compared against those reported for other $CO_2$ gas sensors in the literature.

*Sensitivity*

From the measured transmitted powers of the sensor at different $CO_2$ concentrations, we calculated the corresponding shifts in the resonance wavelength of the microring resonator using Equation (2.6) and plotted the results in Figure 2.13(a). We observe that the resonance shift has a strong linear correlation to the $CO_2$ gas concentration up to 500ppm, which is the range of interest for atmospheric $CO_2$ monitoring. For higher $CO_2$ concentrations, the sensor response has a declining slope, as shown in Figure 2.13(b), which is likely due to saturation of $CO_2$ absorption in the functional layer.

The slope of the best-fit curve of the data in Figure 2.13(a) in the linear response range (50 - 500ppm) is $S_\lambda = \partial\lambda/\partial C_{gas} = 3.54\times10^{-3}$pm/ppm. This is the sensitivity of the sensor in terms of the resonance wavelength change. Using Equation (2.5), we calculate the sensor sensitivity in terms of the effective index change to be

$$S_{\mathrm{RIU}} = \frac{\partial n_{eff}}{\partial C_{gas}} = \frac{\partial n_{eff}}{\partial \lambda}\frac{\partial \lambda}{\partial C_{gas}} = \frac{n_g}{\lambda_{res}} S_\lambda \approx 1.2\times10^{-8}\,\mathrm{RIU/ppm}, \tag{2.9}$$

where $n_g \approx 5.4$ for a silicon waveguide covered with a 240nm-thick PHMB layer.

The wavelength sensitivity value $S_\lambda = 3.54\times10^{-3}$ pm/ppm of the microring sensor is comparable to that of a fiber optic $CO_2$ sensor using Carbon-Nanotube functional coating, which has a reported sensitivity of approximately $1.5\times10^{-3}$ pm/ppm for $CO_2$ concentration range between atmospheric level and 80% [46]. A long period grating fiber optic $CO_2$ sensor using phenol and its derivative as the functional coating was reported to have a much lower wavelength sensitivity of ~$7.5\times10^{-5}$pm/ppm for $CO_2$ concentrations in the range of 10% - 50%; however, the device requires a saturated humidity environment [47] .

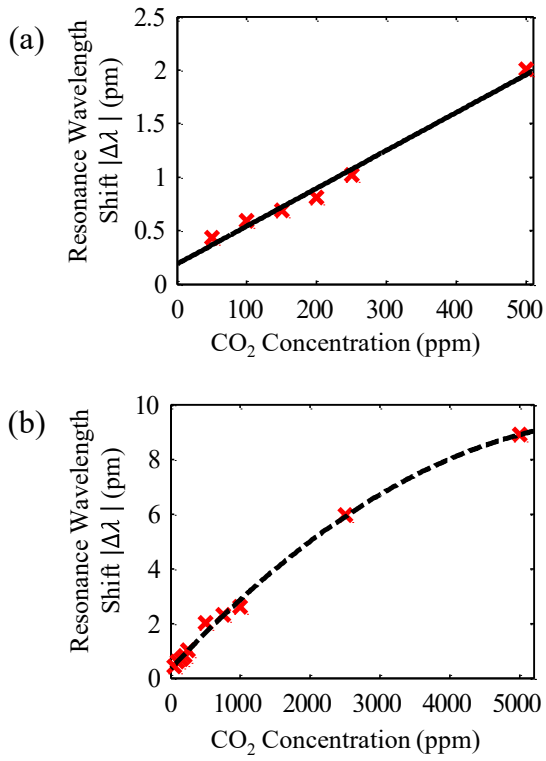


Figure 2.13 (a) Plot of calculated resonance wavelength shifts vs. $CO_2$ gas concentrations. The black line is the linear curve fit of the data up to 500ppm concentration. (b) Plot of resonance wavelength shifts over a wider $CO_2$ concentration range of 0-5000ppm.

As discussed in Section 2.1, the sensitivity of a microring sensor strongly depends on the interaction of the optical mode with the functional layer. To investigate the influence of the PHMB layer thickness on the sensitivity of the $CO_2$ sensor, we functionalized microring resonators with PHMB of different thicknesses and repeated the above experiments to determine their sensitivities. The microring devices were fabricated using the same waveguide dimensions in the same fabrication run at the U. of Washington Nanofabrication Facility, so they had similar optical mode profiles and quality factors. Figure 2.14(a) plots the change in the effective index of the microring waveguide versus the $CO_2$ concentration for PHMB layer thicknesses of 80nm, 130nm, 180nm and 240nm. The effective index change $\Delta n_{eff}$ is calculated from the measured resonance wavelength shift using Equation (2.5), assuming a group index of 5.4 for all the sensor chips. Although the sensors exhibit a slightly nonlinear response over the wide range of gas concentrations shown (0-5000ppm), we can approximate each response by a linear line (dashed lines in the plot) and calculate the average sensitivity for each sensor over this range of

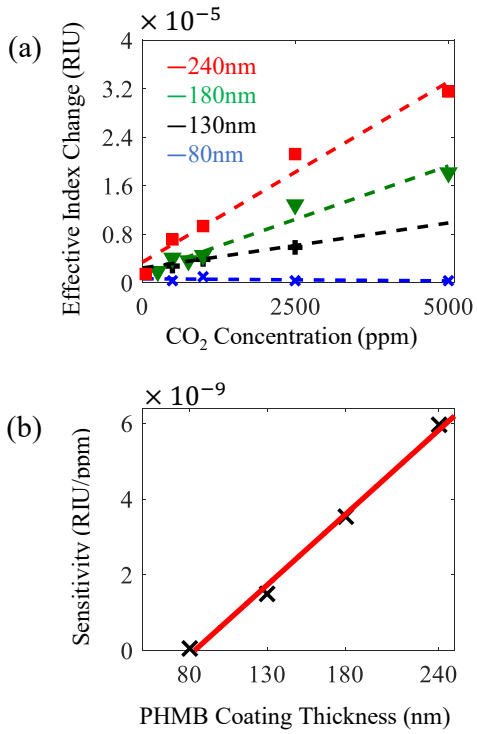


Figure 2.14. (a) Change in effective index of the microring waveguide vs. $CO_2$ gas concentration for PHMB layer thickness of 80nm, 130nm, 180nm and 240nm. (b) Dependence of the sensor sensitivity (averaged over 0-5000ppm range) on the thickness of the PHMB functional layer.

concentrations. The result is plotted vs. the PHMB thickness in Figure 2.14(b), which shows that the sensitivity increases with thicker PHMB. This trend is expected since the interaction factor $\Gamma_s$ in Equation (2.3) increases with increasing thickness of the functional layer. The dependence of the sensitivity on the PHMB layer thickness also provides evidence that the $CO_2$ gas molecules infiltrate into the PHMB polymer rather than adsorb to its surface. This infiltration occurs through a number of mechanisms, including physical diffusion of gas molecules and permeation process, which is caused by molecule transportation from $CO_2$-binding functional groups near the polymer surface to empty groups inside the polymer. The latter mechanism has, in particular, been used to develop $CO_2$-selective permeable polymeric membranes facilitated with functional groups [48].

Although the sensitivity of the microring sensor can be increased by increasing the PHMB layer thickness, it also takes more time for $CO_2$ gas to infiltrate the functional material, which increases the sensor response time. Also, it is more difficult to remove all the $CO_2$ molecules from a thicker functional layer, so the sensor response may not completely return to the baseline upon

purging the chamber with $N_2$ gas. Thus, depending on the application, the thickness of the PHMB layer must be carefully optimized to achieve a balance between sensitivity, sensor response time and precision.

In addition to increasing the functional layer thickness, the sensor sensitivity can also be improved by optimizing the microring waveguide dimensions to increase the fraction of optical mode interacting with the functional layer (i.e., maximizing the interaction factor $\Gamma_s$). For example, a slot waveguide structure has been employed in [32] to construct a microring resonator sensor with enhanced sensitivity to refractive index change of the surrounding environment

*Limit of Detection*

To determine the LOD of the sensor, we first estimated the steady-state noise of the experimental system in terms of the fluctuations in the resonance wavelength measurements. We recorded the transmitted power of the sensor under 50ppm $CO_2$ gas flow for 2 minutes after the sensor response had stabilized and collected a total of $N$ = 100 data points. We calculated the resonance wavelength shift $\Delta\lambda_i$ associated with each transmitted power data point $i$. The standard deviation in the measured resonance wavelength shifts was then determined using the formula

$$\sigma_{static} = \sqrt{\frac{\sum_{i=1}^{N}(\Delta\lambda_i - \Delta\lambda_a)^2}{N-1}},\ \Delta\lambda_a = \frac{\sum_{i=1}^{N}(\Delta\lambda_i)^2}{N}. \tag{2.10}$$

where $\Delta\lambda_a$ = 0.46pm is the average wavelength shift. We obtained $\sigma_{static} = \pm 0.016$pm. This value represents the total uncertainty in the measured resonance wavelength, which includes all relevant sources of noise in the system such as laser wavelength precision, photodetector noise, and noises due to scattering and thermal fluctuations. The sensor LOD specified in terms of the uncertainty in the measured gas concentration, $\delta C_{static}$, can be calculated from the relation $\delta C_{static} = \sigma_{static}/S_\lambda$ to be ±4.5ppm

To determine the repeatability of the sensor system, we performed a sensing experiment with 50ppm $CO_2$ gas consisting of 10 repeated sensing cycles, where each cycle consisted of a 3-minute sensing period and a 3-minute regeneration period. A 3-minute baseline acquisition procedure was performed at the beginning of the experiment. From the wavelength shift data collected over the 10 cycles of 50ppm $CO_2$ gas flows, we calculated the average resonance wavelength shift to be 0.46pm, with a standard deviation of $\sigma_\lambda = \pm 0.071pm$. We note that the value $\sigma_\lambda$ is larger than

the steady-state noise ($\sigma_{static}$ = ±0.016pm) measured above. This is due to the fact that the latter measurements also included noise in the gas flows, fluctuations in the initial chamber condition, as well as noise caused by the regeneration of the PHMB layer. Thus the value $\sigma_\lambda = \pm 0.071pm$ gives a more realistic estimate of the uncertainty in the wavelength shift during normal sensor operation.

Since the detected gas concentration is related to the resonance wavelength shift through the linear slope $S_\lambda$, we obtain the 1σ-resolution of the sensor in terms of uncertainty in the $CO_2$ gas concentration to be $\delta C_{gas} = \sigma_\lambda / S_\lambda = \pm 20ppm$. This value represents the LOD of our microring gas sensor system, which is among the lowest reported for refractometric $CO_2$ gas sensors. For example, a recently reported $CO_2$ sensor based on localized surface plasmons (LSP) for detecting $CO_2$-induced refractive index change in a Carbon-Nanotube coating showed a much larger LOD of 150ppm [46]. A surface plasmon resonance (SPR) sensor using a functional polymer blend in [36] reported a LOD as low as 10ppm for gaseous $CO_2$; however, its operation is limited to a humidified gas environment. Furthermore, the angle measurement setup required for SPR sensors renders them unsuitable for the development of compact and low cost $CO_2$ sensors. We also note that the LOD performance of our silicon microring sensor is comparable to some commercial NDIR $CO_2$ sensors, such as the dual beam NDIR sensor ZG1683R(U) from ZyAura [49], which has a reported sensor repeatability of ±20ppm.

For a refractometric microring sensor, the uncertainty $\sigma_\lambda$ in the measured resonance wavelength shift is approximately inversely proportional to the Q factor of the resonator up to around $10^6$, above which $\sigma_\lambda$ becomes constant [34, 50]. Since $\delta C_{gas} = \sigma_\lambda / S_\lambda$, the detection limit of the microring sensor is thus proportional to $1/QS_\lambda$. Our current sensor has a Q factor of around 20,000, which is relatively low and can be further enhanced by at least a factor of five to achieve a corresponding five-fold reduction in the detection limit. The SNR of the sensor system is also shown to influence the uncertainty $\sigma_\lambda$ through an exponential relationship of $\sigma_\lambda \propto 1/\mathrm{SNR}^{0.25}$ [34]. For our interrogation method of monitoring the transmitted power at a fixed operating wavelength, the SNR can be improved by using a microring resonator with a deeper extinction, which can be achieved at near critical coupling. The steeper transmission slope of such a resonator provides a larger change in the transmitted power in response to the same resonance wavelength shift and hence the same gas concentration. Since we define sensitivity as $\partial\lambda/\partial C$, the sensitivity doesn't change with extinction ratio, but with the same Δλ shift, the change in transmitted power $\Delta I$ is

bigger as depicted in Equation (2.6), and suppose a stable noise in power measurement, thus improved SNR. Our current sensor has an extinction ratio of ~10dB, which can be much further improved by changing the width of the coupling gap to obtain near critical coupling condition.

### *2.6.3 Sensor selectivity against hydrogen gas*

We also investigated the selectivity of PHMB as a functional layer for $CO_2$ gas against hydrogen gas. Being the smallest gas molecule, hydrogen readily penetrates and diffuses into many polymeric materials, so it is important to verify that $H_2$ gas does not induce unwanted refractive index change in the PHMB layer and cause false detection of $CO_2$. In addition, with the emergence of $H_2$ as an important fuel source for sustainable development and $CO_2$ being the major by-product of $H_2$ generation [51, 52], the development of a low-cost and compact $CO_2$ gas sensor with good selectivity against $H_2$ is important for in-line monitoring of $H_2/CO_2$ separation in hydrogen generation processes.

Figure 2.15 shows the response of a PHMB-functionalized microring sensor to 3-minute pulses of 0.5% $CO_2$ gas and 0.5% $H_2$ gas followed by $N_2$ carrier gas chamber purge. The sensor had a 180nm PHMB thickness. As shown by the red trace, the transmitted power remained near the baseline level during two cycles of $H_2$ gas flow, which are indicated by the blue dashed rectangles. The transient fluctuations observed at the beginning of each cycle are attributable mainly to gas flow transitions. It is evident that the sensor showed no response to $H_2$ or $N_2$ gas and only reacted to the presence of $CO_2$ gas. This experiment thus demonstrates that PHMB has good selectivity against hydrogen gas.

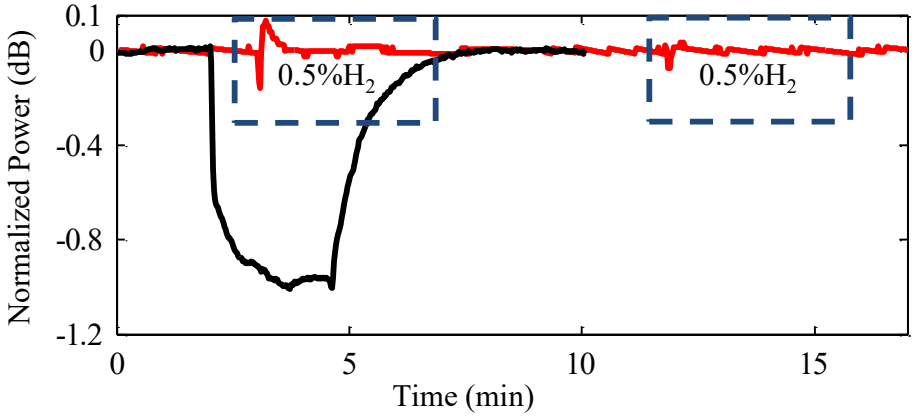


Figure 2.15. Transmitted power response of the microring sensor to 3-minute pulses of 0.5% (5000ppm) $CO_2$ gas concentration (black trace) and 0.5% $H_2$ gas concentration (red trace). $N_2$ gas was used as carrier for both tests.

## 2.7 Summary

In this chapter, we reported a refractometric silicon photonic $CO_2$ gas sensor based on a microring resonator. The sensor used a novel functional material, PHMB, which was shown to exhibit reversible refractive index change in the presence of $CO_2$ gas molecules. Compared to other functional materials for $CO_2$ gas, PHMB has the advantage that it does not require a humidified environment for $CO_2$ detection and can operate at room temperature. A series of experiments were performed to demonstrate the operation of the sensor and to evaluate its performance in terms of sensitivity and limit of detection. The sensor was shown to exhibit linear response over the 0 - 500ppm range of $CO_2$ concentrations, with a detection limit of 20ppm, making it suitable for monitoring $CO_2$ gas levels in the atmosphere.

We also showed that PHMB has good selectivity against hydrogen, which makes it useful for developing a dual-gas photonic sensor for the simultaneous detection of $CO_2$ and $H_2$. In the next chapter, we will propose and demonstrate a wavelength-multiplexing scheme based on silicon microring resonators functionalized with different materials for $CO_2$ and $H_2$ gas monitoring.

# Chapter Three.

# A Silicon Photonic Dual-Gas Sensing System

## 3.1 Integrated Photonic Multi-Analyte Sensing Systems

The development of multi-analyte sensor systems on a chip has attracted growing interest in recent years since they provide low-cost sensing solutions along with rapid chemical analysis capability. Such multi-analyte sensors have been realized on different sensing platforms, such as electrochemical sensors, surface plasmon resonance sensors, fluorescence sensors, etc. For example, a multi-analyte biosensor using four organic electrochemical transistors was demonstrated in [53] for the detection of glucose and lactate solutions. A paper-based colorimetric sensor was reported in [54] for multi-analyte diagnosis. The sensor uses 12 indicator pads to analyze 12 biomarkers in urine for point-of-care diagnosis. The vast selection of available chemical fluorescent and colorimetric probes also allows various combinations of analytes to be detected in a multiplexing scheme, ranging from simple pH value [55] to complicated protein molecules [56].

As we have demonstrated in the previous chapter, microring resonators have promising potential for developing integrated photonic sensors with high sensitivities [57-61] and micron-scale dimensions, making them particularly suitable for implementing large scale sensor arrays on a chip. Unlike other integrated optics structures such as gratings and Mach-Zehnder interferometers, the sensitivity and resolution of a microring sensor do not degrade with smaller microring size, which is a crucial advantage for reducing sample consumption while enabling high-density integration of multiple sensing channels on a chip. Multi-analyte detection based on arrays

of microring resonators can be achieved either through a spatial multiplexing scheme or a wavelength division multiplexing (WDM) scheme.

In a spatial multiplexing scheme, each microring is coupled to a different straight waveguide so that the output signals of the microring array can be detected simultaneously by a photodiode array. The microring channels can each have their own input light source [62], or they can be coupled to a common light source through a multi-mode interference (MMI) splitter.[58]. Implementations of spatially-multiplexed photonic sensors based on microring resonators have been reported mostly for biosensing applications. Carlborg *et al.*[58] developed a label-free assay on a 7mm×3mm chip consisting of seven spatially-multiplexed microring sensing channels sharing a common optical input port via an MMI splitter. The device used a slot waveguide structure to enhance the sensor's sensitivity to refractive index change, with a reported LOD of $5\times10^{-6}$ RIU. A group from the University of Washington [62] reported a bioassay chip with distributed microring sensors, which are selectively functionalized with six different types of biomarkers by inkjet technology for detecting two types of carbonhydrate-binding proteins. Inkjet technology is increasingly becoming a popular method for functionalizing individual microring sensors on a chip because it is fast, precise and uses only small volumes of functional materials, although applicable materials should either be available in liquid phase or they can be dispersed or dissolved in a certain solvent [63, 64].

In the WDM approach, microring sensors are coupled to a common straight waveguide with a common light source and detector. The microring resonators are designed such that their resonance frequencies are separated within one FSR. By tuning the input wavelength, different microring channels can be addressed. Several multi-analyte photonic sensors exploiting the WDM capability of microring resonators have been reported. Xu *et al.* [65] demonstrated a biosensor array with five microring resonators coupled to a single bus waveguide and addressed by a WDM scheme. The biosensor array was used for monitoring molecular binding activities of two different antigen-antibody pairs simultaneously, and achieved a resolution of 0.3 pg/mm$^2$ and a selectivity greater than 15:1 for complementary versus mismatched protein pairs. Researchers from Ghent University [66] combined both WDM and spatial multiplexing schemes to obtain a sensor array consisting of 12 microring resonators on an area of 4mm×750μm, with three input waveguides each connected to four microrings. They demonstrated multiplexed antibody detection using different receptor molecules bound to different microrings in each of the four-ring channels.

With respect to photonic gas sensors, most reported works have mainly focused on the detection of a single gas. One of the few works on multi-gas sensing came from a group at Georgia Institute of Technology [29], who reported the detection of four volatile organic compound (VOC) vapours separately using an array of microring resonators functionalized with four different polymers. However, not only did each functional polymer show significant response to all four target VOCs, but different polymers also had similar responses when tested with the same VOC vapour. Thus, the sensor selectivity for the different target gases was poor. This example again illustrates the importance of selecting appropriate functional materials for label-free refractometric sensors, especially when operated in a multi-analyte environment.

In this chapter we report our work on the development of a silicon photonic dual-gas sensor for the simultaneous detection of $CO_2$ and $H_2$ gases. Both of these gases are closely monitored in the oil and energy industry for environmental and safety compliance. In particular, hydrogen is colorless and tasteless but is also highly explosive with a high diffusion coefficient in air. It is present in the production of traditional fossil fuels as well as the generation of clean energy, such as hydrogen fuel cells. The detection of $H_2$ gas is an integral part of any safety alarm system in an industrial setting.

A commonly used functional material for $H_2$ detection is the palladium metal [67-70]. One of the main objectives of this work is to demonstrate the possibility of integrating PHMB polymer for $CO_2$ detection with other types of functional materials (in this case metal) on the same chip. Another objective is to assess the performance of PHMB as a functional material for $CO_2$ detection in a multi-gas sensing environment. The results of this study could enable the development of silicon photonic multi-gas sensor arrays for environmental greenhouse gas and industrial emission monitoring.

This chapter is organized as follows. In Section 3.2, we present the design of a dual-gas sensor based on silicon microring resonators, and explain the choice of various design parameters. Section 3.3 will describe the fabrication and functionalization of the dual-gas microring sensor. In Section 3.4, we will describe the dual-gas sensing experiments and discuss the sensor performance in terms of sensitivity, limit of detection and cross-talks. The chapter is summarized in Section 3.5.

### 3.2 Design of a Silicon Photonic Dual-Gas Microring Sensor

One of the advantages of microring sensors is the wavelength multiplexing capability of the resonators, which can be used for parallel detection of multiple analytes. For proof-of-concept demonstration, we designed and realized a prototype sensor chip targeting the detection of two gases, $CO_2$ and $H_2$. Figure 3.1(a) shows a schematic of the proposed microring sensor array design, which consists of three microring resonators evanescently coupled to the same straight waveguide. Microring 1 is left uncovered and serves as the reference device to track temperature and laser power variations. Microrings 2 and 3 serve as sensing elements for $H_2$ and $CO_2$ gases and are functionalized with Pd and PHMB, respectively. The cross-section views of the two functionalized microrings are shown in Figure 3.1(b) and (c). In order to keep track of the resonance wavelength shift of each microring, their resonance wavelengths ($\lambda_1$, $\lambda_2$, $\lambda_3$) are designed to be slight different by varying the individual ring's waveguide width (i.e., tuning its $n_{eff}$ value) while keeping the radius constant. The coupling gap between the common straight waveguide and each microring resonator is adjusted depending on the optical absorbance of the functional coating on the microring in order to achieve near critical coupling condition. As discussed in the previous chapter, critical coupling results in microring resonance spectra with deep extinction, which helps to improve the signal-to-noise ratio (SNR) and the limit of detection of the sensor. The straight waveguide is connected to grating couplers at both ends for coupling light in and out of the chip via fibres.

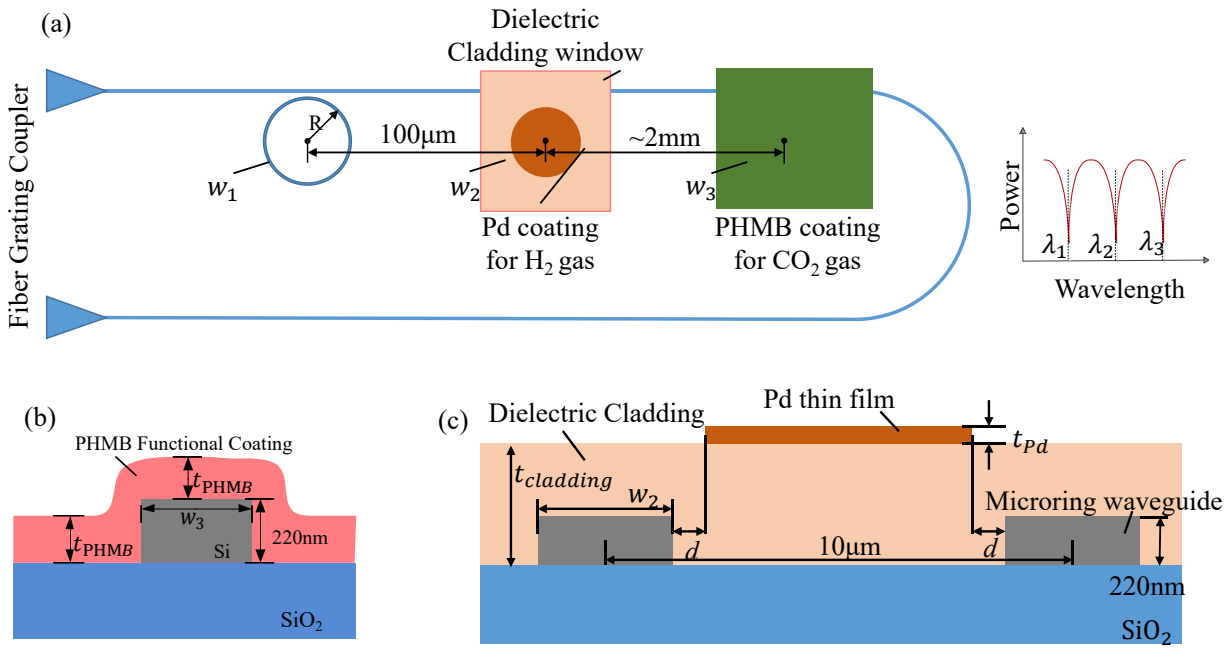


Figure 3.1 The proposed optical microring resonator sensing array. (a) Schematic of the dual-gas sensor using arrayed microrings. (b) Cross-section view of the microring waveguide functionalized with PHMB. (c) Cross-section view along the diameter of the microring with Pd coating.

We implemented the sensor array on a Silicon-on-Insulator (SOI) platform for operation in the telecommunication wavelength range (1.5μm - 1.6μm). The SOI chip consists of a 220nm layer of crystalline silicon on a 3μm-thick $SiO_2$ under-cladding layer. The straight waveguide width is chosen to be 450nm, which supports a single TE mode with effective index $n_{eff}$ = 2.45 at 1.55μm wavelength. The microring resonators are designed to have a radius of 10μm, which gives an FSR of about 9nm. The resonances of the 3 microrings are designed to be separated by about 2nm within one FSR. This variation is achieved by tuning the width of the resonator waveguide around the nominal value of 450nm. The coupling gap between the microring and the straight waveguide is designed to be 170nm, except for the Pd-coated microring resonator (Pd-MRR), whose gap is reduced to 140nm to compensate for the higher loss of the metal film. The distance between the Pd-MRR and the reference microring resonator (Ref-MRR) is set to be 100μm, which leaves enough space for a cladding window to be opened on the Pd-MRR ring for Pd deposition. On the other hand, the microring resonator functionalized with PHMB (PHMB-MRR) is placed ~2mm away from the other two microrings to facilitate the deposition of the PHMB layer, as described later.

The grating couplers for input/output light coupling were designed for TE polarization with 220nm etch depth, which matches the thickness of the silicon core layer so that the waveguide structures and the grating couplers can be fabricated in a single electron beam lithography (EBL) and etching process. Since conventional fully-etched grating couplers suffer from strong back reflections due to the large index contrast of the gratings [71, 72], we designed the couplers with sub-wavelength gratings to improve the coupling efficiency, as reported in [73].

## 3.3 Fabrication and Functionalization of Sensor Chip

The implementation of the dual-gas sensor chip can be divided into three main steps: fabrication of the silicon photonic chip, selective functionalization of MRR sensing elements, and bonding of the chip to a pigtailed fibre array. We will describe each of these steps in detail below.

### *3.3.1 Fabrication of SOI microring sensor chip*

The sensor device was fabricated on a $1cm^2$ SOI chip at the University of Alberta's NanoFab using Electron Beam Lithography (EBL) and silicon dry etching. We used hydrogen silsequioxane negative photoresist (HSQ, Dow Corning XR-1541 E-Beam resist 6%) because of its shorter EBL write time and better etching resistance compared to the positive-tone PMMA photoresist. Dry etching is performed using an Oxford Estrelas Inductively Coupled Plasma Reactive Ion Etching (ICP-RIE) system to transfer the HSQ pattern onto the silicon layer. The HSQ residue is removed from the chip after etching, leaving the silicon waveguides exposed to air. A detailed description of the fabrication process can be found in Appendix I.

Figure 3.2 shows SEM images of a typical fabricated sensor chip. Figure 3.2(a) shows the image of a grating coupler, which uses elliptical focusing grating lines to achieve better coupling ratio than conventional straight grating lines [74, 75]. Figure 3.2(b) shows a typical fabricated microring resonator, with a radius of 10μm, waveguide width of 420nm, and coupling gap of 145nm. Figure 3.2(c) shows a magnified image of the side wall of a silicon waveguide patterned by EBL and ICP-RIE dry-etching.

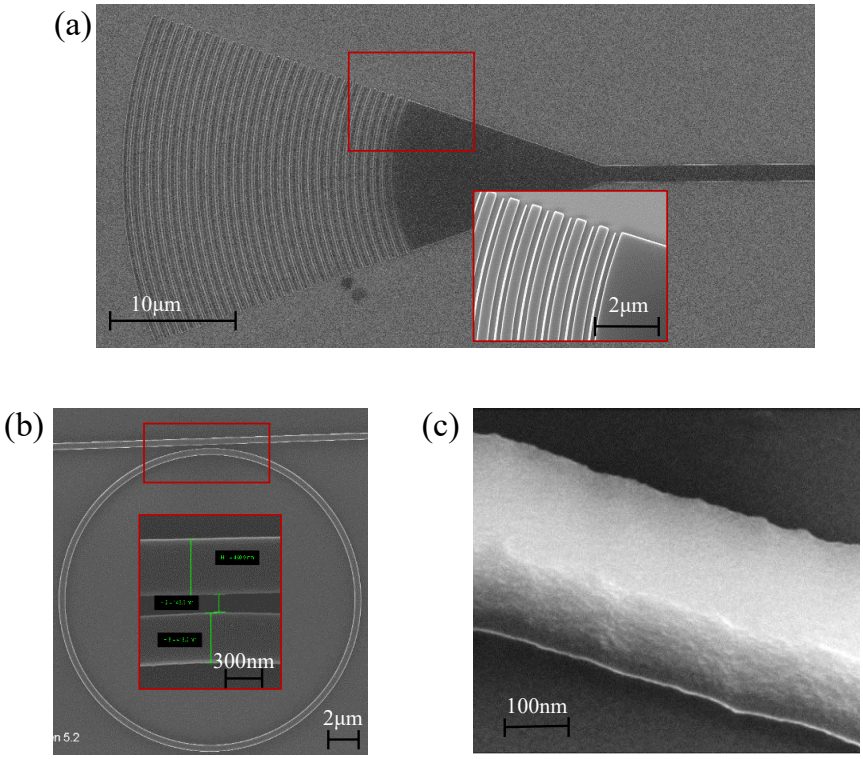


Figure 3.2. SEM images of key components of a typical fabricated sensor chip. (a) A grating coupler, inset shows a zoomed-in view of the grating lines. (b) A microring resonator, inset shows a zoomed-in view of the coupling region. (c) The side wall of a fabricated silicon waveguide.

### *3.3.2 Functionalization of the microring sensors*

Since the detection of $CO_2$ and $H_2$ gases requires two different types of functional materials, namely, a polymer and a metal, a special procedure for incorporating both of these materials on the same microring sensor chip must be developed. We describe below the functional materials used and the procedure for functionalizing the microring sensors.

*Functional material for $CO_2$ gas sensing*

In Chapter 2 we showed that a PHMB polymer thin film exhibits reversible refractive index change upon absorbing and releasing $CO_2$ gas molecules, and this optical response is correlated to the $CO_2$ gas concentration in a sealed chamber. In addition, the PHMB thin film shows no response to $H_2$ gas, making it suitable as a functional material for $CO_2$ detection in the dual-gas sensing environment.

*Functional material for $H_2$ gas sensing*

Palladium is a commonly used functional material for $H_2$ detection due to the strong hydrogen-palladium interaction and the high diffusion coefficient of hydrogen in the Pd lattice [76]. When adsorbed onto a Pd surface, a hydrogen molecule dissociates into two ions, which diffuse into the metal lattice and reside in the interstitial site, forming hydrides ($PdH_x$). This reaction increases the lattice constant of Pd, causes volume expansion and alters the electrical and optical properties of the macroscopic medium. The ratio $x$ of Pd to H atoms in a hydride depends on the hydrogen partial pressure and temperature. At low ratios ($x < 1.5\%$) the deformation of Pd lattice from hydride reaction is reversible when the hydrogen is removed. This is achieved by purging the material with $N_2$ gas flow. At high ratios ($x > 60\%$) the lattice change is permanent, which is undesirable for sensor applications. Heating the device to above 300℃ can reverse the reaction but may not be suitable for some applications. Several different Pd metal alloys have been synthesized with the aim of reducing the reaction temperature to room temperature by adding catalysts to the reaction [76, 77].

Integrated optical sensors with Pd coatings have been developed in the past with various constructions. A group from the University of Toronto reported a photonic $H_2$ sensor based on a Pd-coated ridge silicon waveguide by monitoring the change in the transmitted power of the functionalized waveguide upon exposure to various $H_2$ gas concentrations [78]. The same group further investigated the influence of Pd thin film thickness to sensitivity and hysteresis behaviour of the sensor in [69]. A whispering gallery mode (WGM) $H_2$ sensor based on a Pd-coated SU-8 microdisk was reported in [70] for detecting $H_2$ gas in the 3000 – 10,000 ppm range. When exposed to $H_2$ gas, the Pd coating undergoes expansion and induces strain on the polymer microdisk, which causes a red shift in the resonance wavelength of the microdisk. For our dual-gas sensor, we chose Pd as the functional material for $H_2$ sensing in order to provide a basis for comparison between the performance of our dual-gas sensor to that of stand-alone $H_2$ sensors reported in the literature.

*Functionalization procedure*

To incorporate the two different types of functional materials for detecting $CO_2$ and $H_2$ on the same chip, we have developed a functionalization procedure according to the property and deposition techniques of the two materials. Specifically, the PHMB polymer can be deposited by

spin-coating and removed using DI water, whereas Pd metal thin films are commonly deposited using a Physical Vapor Deposition (PVD) technique such as magnetron sputtering and electron beam evaporation, and patterned with a lithography-based lift-off method. Since PHMB is water soluble, we functionalize the chip first with a Pd thin film, followed by spin-coating of the PHMB polymer. The functionalization procedure of the sensor chip consists of the following steps:

a) **Cleaning**. The fabricated SOI chip is first cleaned in a Piranha bath to remove potential organic contamination on the microring surface.

b) **Dielectric cladding**. Palladium is a highly-absorbing noble metal with a complex refractive index of $n_{\mathrm{Pd}} = 3.16 - 8.12j$ at 1550nm wavelength [79]. To isolate the optical mode of the Si MRR from the lossy metal film, we need to deposit a dielectric cladding layer on top of the MRR waveguide and place the Pd layer on this cladding layer in order to minimize the optical loss while ensuring that the MRR can sense the refractive index change in the Pd layer upon exposure to $H_2$ gas. In addition, we will also need to selectively remove this cladding layer from the PHMB-MRR for $CO_2$ sensing.

We initially used PECVD $SiO_2$ as the dielectric cladding layer since it has a refractive index matching that of the underlying oxide layer of the SOI substrate. Optical lithography and wet etching in BOE (buffered oxide etch) were used to selectively remove the cladding layer on top of the PHMB-MRR and the reference microring. However, the BOE also etched the oxide laterally underneath the Si waveguides, causing the microrings and waveguides to become loosely attached to the surface of the oxide layer and prone to destruction when washed with DI water and blow-dried with $N_2$. Figure 3.3 shows an example of a destroyed microring using this method. To avoid this issue, we decided to use HSQ photoresist instead as the cladding layer. HSQ thin films can be deposited by spin-coating and patterned using EBL. After electron beam exposure or thermal curing, the HSQ resist becomes amorphous silica with a refractive index of 1.38~1.41 depending on the exposure dosage or the curing temperature [80, 81].

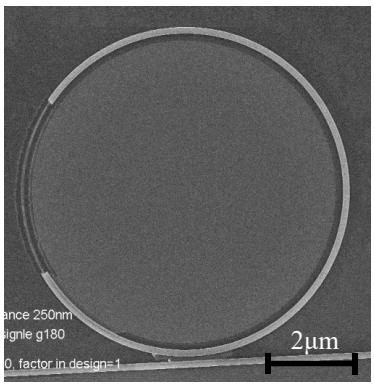


Figure 3.3 An SEM image of a destroyed microrings after wet etching of PECVD $SiO_2$ cladding.

To determine the thickness of the HSQ cladding layer and the lateral position of the Pd layer, we used the COMSOL Multiphysics software to study the influence of a 13nm-thick Pd thin film on the TE mode of a 450nm×220nm Si waveguide. Figure 3.4 shows the simulation result when the Pd thin film is placed on a 320nm-thick HSQ cladding with a refractive index of 1.4, at a lateral distance of $d$ = 275nm from the edge of the Si waveguide core. The presence of the Pd film causes the real part of the effective index of the waveguide to increase by $1 \times 10^{-4}$. The imaginary part of the effective index also increases to $1.8 \times 10^{-5}j$, which corresponds to 1.6dB/cm waveguide loss. This magnitude of change in the real part of the effective index can be detected by the silicon microring while the extra waveguide loss is kept low enough so as not to significantly degrade the resonator's Q factor.

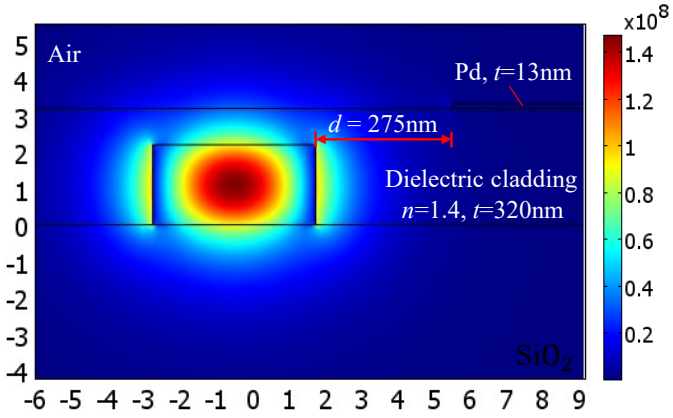


Figure 3.4 TE mode of the Si waveguide with Pd thin film.

**c) Functionalizing the Pd-MRR**

Figure 3.5 summarizes the metal lift-off procedure for depositing a Pd thin film on top of the microring for $H_2$ sensing. The pictures illustrate the cross-section view along the diameter of the microring after each processing step. We first spin-coated a 320nm-thick HSQ cladding layer on the chip, as shown in Figure 3.5(a), and used EBL to pattern the layer so that only a square region of HSQ is left to cover the Pd-MRR. Next, we spin-coated the chip with a 90nm-thick layer of PMMA (950 A2) and used EBL to expose an 18.5μm-diameter disk concentric to the microring, as illustrated in Figure 3.5(b). The exposed PMMA disk was then removed with a methyl isobutyl ketone (MIBK) : IPA developer. A ~13nm-thick Pd thin film was then deposited on the chip, as shown in Figure 3.5(c), using a planar magnetron sputter system. Metal lift-off was performed by immersing the chip in an Acetone bath, which left only a Pd disk on the microring as illustrated in Figure 3.5(d). Figure 3.5(e) shows an SEM image of the Pd-MRR. The Pd microdisk is concentric to the microring with a diameter of 18.45μm, so that the microring waveguide is not covered with Pd and can be seen in the image.

**d) Functionalizing the PHMB-MRR**

To functionalize the PHMB-MRR, we spin-coated a layer of PHMB on the entire chip. The chip was baked at 110˚C for 5 minutes, then dipped partly in DI water to dissolve the PHMB only from the region where the Pd-MRR and Ref-MRR were located.

In Section 2.4.1 we found that the sensitivity of the $CO_2$ microring sensor had a positive correlation to the thickness of the PHMB layer in the range of 80 - 240nm. For the dual-gas sensor chip, we chose a thick PHMB layer of 620 nm thickness with the aim of investigating the sensor performance in terms of sensitivity and resolution for very thick PHMB films.

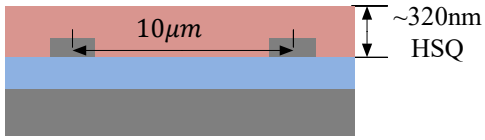


(a) Sensor chip with HSQ cover window patterned on one microring resonator

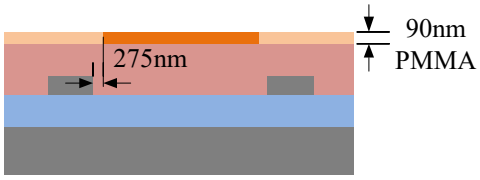


(b) PMMA patterning with E-Beam Lithography


(c) Pd thin film deposition using a planar magnetron sputter system

(d) Lift-off and Pd-coated microring

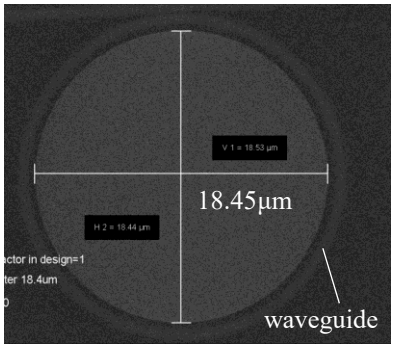


(e) SEM image of the functionalized microring

Figure 3.5 Functionalization of the Pd-MRR using EBL and metal lift-off method. (a) – (d) Cross-section views along the microring diameter after each step of the functionalization process. (e) An SEM image of the microring with the Pd functional layer.

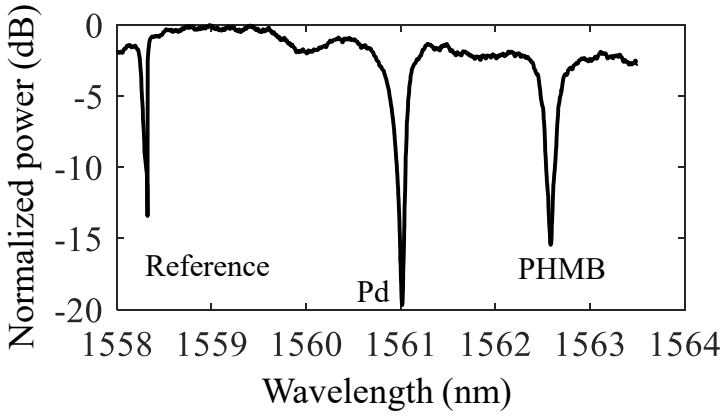


Figure 3.6 Resonance spectrum of the packaged multi-gas sensor chip measured under $N_2$ gas flow.

| | | Pd-MRR | PHMB-MRR | Ref-MRR |
|---|---|---|---|---|
| **Dimensions** | Width | 452nm | 511nm | 455nm |
| | Coupling Gap | 155nm | 190nm | 180nm |
| **Extracted parameters** | Roundtrip loss | 59dB/cm | 40dB/cm | 35dB/cm |
| | Coupling | 0.95 | 0.98 | 0.98 |
| **Functional layer thickness** | | Pd thickness: ~13nm<br>HSQ buffer: 321nm<br>Lateral distance: ~290nm* | PHMB: 620nm | N/A |

*: Estimated from the result of a test chip fabricated using the same recipe but with no HSQ buffer window, which defocuses the waveguide profile in SEM image thus affects dimension measurement. The actual device chip is not measured with SEM after functionalization to minimize possible contamination and deactivation to the Pd thin film

Table 3.1 Parameters of each microring resonator on the fabricated sensor chip.

### *3.3.3 Device packaging and characterization*

After functionalization, the chip was bonded to a fibre array using the method described in Section 2.5.1. Following the procedure described in the *preconditioning* step in section 2.5.2, we obtained the initial spectrum of the dual-gas sensor as shown in Figure 3.6. We observe that within a 9nm FSR of the microrings, there are three distinct resonances corresponding to each of the three microrings. From subsequent gas sensing experiments, we could identify which resonance belongs to which microring, as labeled in Figure 3.6. We also performed curve-fitting of each resonance spectrum to obtain the relationship between the transmitted power and the wavelength shift, which will be used in subsequent sensing experiments. The coupling coefficient and roundtrip loss values extracted from the curve fit of each microring are summarized in Table 3.1, along with the device dimensions and functional layer thickness.

## 3.4 Sensing Experiments and Results

The experimental setup used to perform sensing experiments with $CO_2$ and $H_2$ gases is shown in Figure 3.7. The analyte gases were supplied to the test chamber from two separate gas tanks containing 1% $H_2$ and 1% $CO_2$. The flow of each gas was controlled and regulated by a small-volume MFC. Before setting a target gas flow, the gas supply system was purged successively with $N_2$ and the target gas at 100 sccm flow rate for 5 minutes to remove residue gases in the hoses.

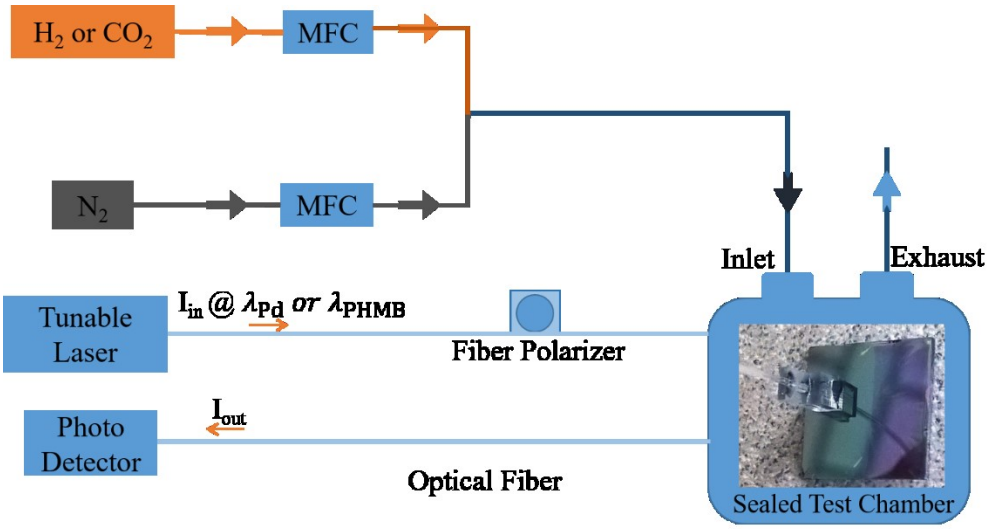


Figure 3.7 Schematic of experimental setup employed to measure the response of the Pd-MRR and PHMB-MRR to separate $H_2$ and $CO_2$ gas flows.

Following the procedure described in Section 2.6.1, we performed sensing experiments by flowing various concentrations of either $CO_2$ or $H_2$ gas into the test chamber and monitoring the transmitted power response of each microring sensor at a fixed wavelength located on the shoulder of the microring resonance spectrum. From the transmitted power, we computed the corresponding resonant wavelength shift to determine the sensor response to the analyte gas.

In the experiments below, we first studied the response of a standalone Pd-MRR sensor to $H_2$ and $CO_2$ gases to understand its behaviours and determine the sensitivity and selectivity of the Pd-MRR to each of these gases (the response of a standalone PHMB-MRR sensor to both of these gases was already investigated in Chapter 2). Next, we performed a series of experiments to evaluate the performance of the dual-gas sensor chip. We will first report the response of each microring on the chip (Ref-MRR, Pd-MRR, PHMB-MRR) to individual $H_2$ and $CO_2$ gas flows. We will then report the response of the sensor chip to a mixture of $H_2$ and $CO_2$ gases.

### *3.4.1 Response of a standalone Pd-MRR*

To study the response of a standalone Pd-MRR to $H_2$ and $CO_2$ gases, we prepared a separate sensor chip containing a single microring functionalized with only Pd. The SOI chip was taken from the same batch of devices used in Chapter 2, which were fabricated at the U. of Washington Nanofabrication Facility. To simplify the functionalization process, we deposited the chip with a 315nm layer of PECVD $SiO_2$ and used the metal lift-off process described in Section 3.3.2 to

pattern a Pd disk on the microring. The Pd layer had a thickness of ~13nm and lateral separation distance of $d$ ~275nm from the microring waveguide. The functionalized microring had a Q-factor of ~6800.

We next performed $H_2$ and $CO_2$ gas sensing experiments on the standalone Pd-MRR sensor. Figure 3.8(a) and (b) show the plot of the resonance wavelength shift vs. gas concentration for $H_2$ and $CO_2$ gas, respectively. In Figure 3.8(a) we observe that the microring exhibits a blue shift in the resonance wavelength upon exposure to $H_2$, with the magnitude of wavelength shift increasing linearly with the gas concentration. The blue shift in the resonance spectrum indicates a decrease in the effective index of the microring waveguide, which results from a decrease in the refractive index of Pd upon exposure to $H_2$ gas. As discussed previously, this change in the refractive index of Pd can be explained in terms of the lattice expansion of the metal upon absorption of hydrogen, which reduces the hydride conductivity and decreases its refractive index [67]. From the slope of the linear curve fit of the data in Figure 3.8(a), we calculate the wavelength sensitivity of the Pd-MRR to $H_2$ gas to be $S_\lambda = 1.90\times10^{-3}$pm/ppm, which is among the highest reported for Pd-based optical hydrogen sensors. For example, a Pd hydrogen sensor based on fibre Bragg grating was reported in [67] showing a highest sensitivity of 0.75pm/ppm at 19˚C. This fibre optic sensor also showed a decrease in its sensitivity with increasing temperature. Eryürek *et al.* reported a hydrogen sensor using Pd-coated SU-8 micro-resonator with a sensitivity of $3.2\times10^{-3}$pm/ppm[70]. However, their Pd sensor had a lower detection threshold of 3000ppm, while our standalone sensor has shown $H_2$ detection of 1000ppm. The error bars in (a) represent the standard deviation of three repeated measurements at each gas concentration, from which we calculated the uncertainty in the wavelength shift measurements to be $\sigma_\lambda = \pm5.8\%$. This uncertainty represents the detection resolution of the Pd-MRR sensor for $H_2$ gas in terms of wavelength shift. Together with the sensitivity value $S_\lambda$, this wavelength uncertainty determines the sensor LOD through the relation $\mathrm{LOD} = \sigma_\lambda / S_\lambda$.

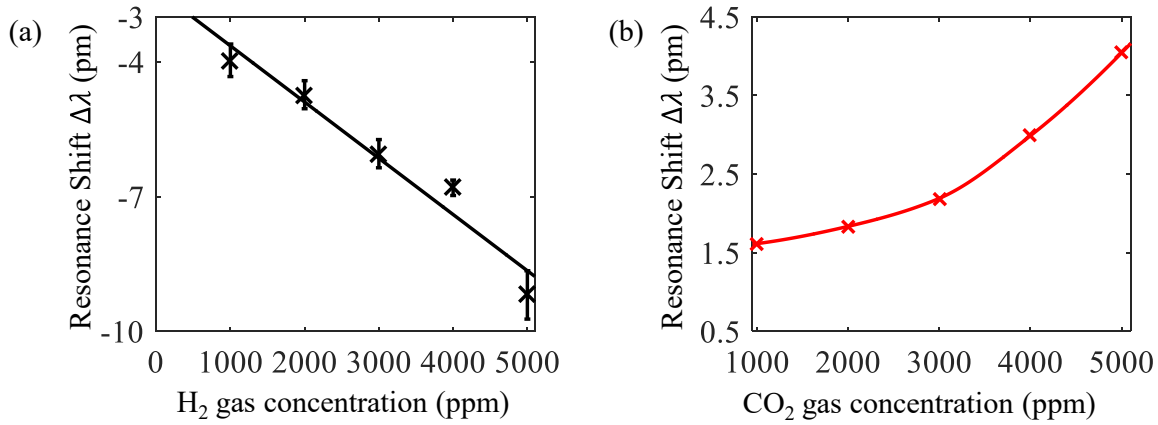


Figure 3.8 Response of a standalone Pd-MRR to $H_2$ and $CO_2$ gases. (a) Plot of the resonance wavelength shift vs. $H_2$ gas concentration. The black line is the linear curve fit of the data up to 5000ppm concentration. (b) Plot of resonance wavelength shift vs. $CO_2$ gas concentration.

From Figure 3.8(b), we observe that Pd-MRR exhibits a red shift in the resonance wavelength upon exposure to $CO_2$ gas. More importantly, the magnitude of the wavelength shift is comparable to the response to $H_2$ gas in Figure 3.8(a), and also shows an increasing trend with increasing gas concentration. These wavelength shifts are too large to be caused by temperature differences in the $CO_2$ gas flows. These results indicate that there seems to be a significant response of Pd to $CO_2$ gas, which to our knowledge, has not been reported before. One possible explanation may be the adsorption of $CO_2$ to the sensor surface by Palladium Oxide at room temperature [82], which might have been formed by partial oxidation of Pd thin film during transportation and storage of the senor chip. This adsorption will form a monolayer of $CO_2$ gas molecules on the Pd-MRR surface, which could increase the effective index of the waveguide mode. Knowledge of the response to Pd to $CO_2$ gas will enable us to more accurate analyze the sensing results of the dual-gas sensor.

### *3.4.2 Response of reference microring on the dual-gas sensor chip*

We next study the response of the dual-gas sensor chip. We will first report the response of the reference microring (Ref-MRR) to $H_2$ and $CO_2$ gas flows of various concentrations to determine the noise floor and thermal stability of the test system. Figure 3.9 plots the resonant wavelength shifts of the Ref-MRR versus $H_2$ and $CO_2$ gas concentrations. We observe that the microring has a similar response to both $CO_2$ and $H_2$ gases, showing a small red shift in the resonant wavelength. Over the large concentration range of 500 – 5000 ppm of each gas, the resonant wavelength shift

is 0.41±0.02pm for $CO_2$ gas and 0.45±0.1pm for $H_2$ gas and appears to be nearly independent of the gas concentration. Using Equation (2.4) and a group index of ~5 for the silicon waveguide, we calculate the corresponding effective index change in the microring to be $1.3\times10^{-6}$ and $1.4\times10^{-6}$ for $CO_2$ gas and $H_2$ gas respectively. Possible sources of this effective index change include pressure-induced index change of the gas environment, the refractive index difference between the gas mixture and $N_2$, and the thermo-optic response of the Si waveguide due to temperature differences in the gas flows. Since we kept a constant gas flow rate of 200sccm in the experiment and maintained the chamber pressure to be the same as the ambient atmosphere, we can eliminate the pressure-induced index change as a contributing source. The refractive index of a gas mixture is determined by the refractive index of each gas component, with a linear relation to the gas concentrations. The refractive index difference between pure gases is very small, e.g. at 1550nm wavelength, $N_2$ and $CO_2$ has refractive indices of 1.00044 and 1.00028. The refractive index difference of an analyte gas mixture (5000ppm $CO_2$ in $N_2$) and $N_2$ can be estimated to be $+8\times10^{-7}$RIU by $n_{CO_2}C_{CO_2} + n_{N_2}C_{N_2}$. Such a difference is too small to cause the wavelength shift observed, and thus, this effect can also be disregarded, leaving temperature variation as the only possible cause.

To estimate the temperature variation that would cause the measured wavelength shift of the Ref-MRR, we assume that the resonance shift is solely due to the index change of the Si waveguide core caused by the difference in the temperatures of the target gas line ($H_2$ or $CO_2$) and $N_2$ gas. Given that the thermo-optic coefficient of silicon at 1550nm is $1.86\times10^{-4}K^{-1}$[83], we estimate that the change in temperature between the target gases and $N_2$ to be approximately $(8\pm1)\times10^{-3}$°C. This level of temperature variations is reasonable for our sensing system and represents the thermal noise source in our measurements.

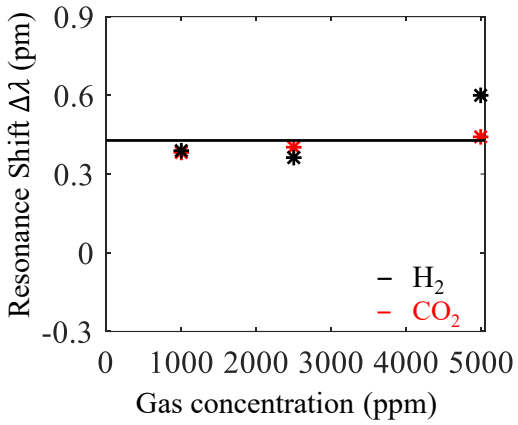


Figure 3.9. Resonance wavelength shifts of the reference microring on the dual-gas sensor chip vs various $CO_2$ (red) and $H_2$ (black) gas concentrations.

### *3.4.3 Response of PHMB-MRR to separate $CO_2$ and $H_2$ gases*

Figure 3.10(a) and (b) show the plots of the resonant wavelength shift of the PHMB-MRR versus $CO_2$ gas and $H_2$ gas concentration, respectively. From Figure 3.10(a) we observe that the response of the PHMB-MRR to $CO_2$ gas is similar to the response of the standalone $CO_2$ microring sensor in Chapter 2. More specifically, the resonant wavelength of the microring is blue shifted upon exposure to $CO_2$, with the amount of wavelength shift linearly correlated to the $CO_2$ concentration. The sensitivity of the PHMB-MRR is $7.62\times10^{-4}$pm/ppm, which is smaller than that of the standalone sensor reported in Chapter 2 ($2.4\times10^{-3}$pm/ppm in the range of 0 – 2500ppm). Since the PHMB polymer layer used in the dual-gas sensor is fairly thick (620nm compared to 240nm in the single-microring sensor), $CO_2$ molecules may not penetrate deep enough into the functional layer, leading to weaker perturbation of the waveguide mode and hence lower sensitivity. It is expected that the sensitivity of the PHMB-MRR can be improved by using a thinner PHMB layer.

The error bars in Figure 3.10(a) represent the standard deviations of three repeated measurements of the wavelength shift. The uncertainty of the sensor in terms of wavelength is calculated to be ±5.3%. This value represents the resolution of the PHMB-MRR for detecting $CO_2$ gas in the concentration range of 0 - 1250ppm. Together with the sensitivity value $S_\lambda$, this wavelength uncertainty represents a LOD of ±39pm, which has a bigger value than that of

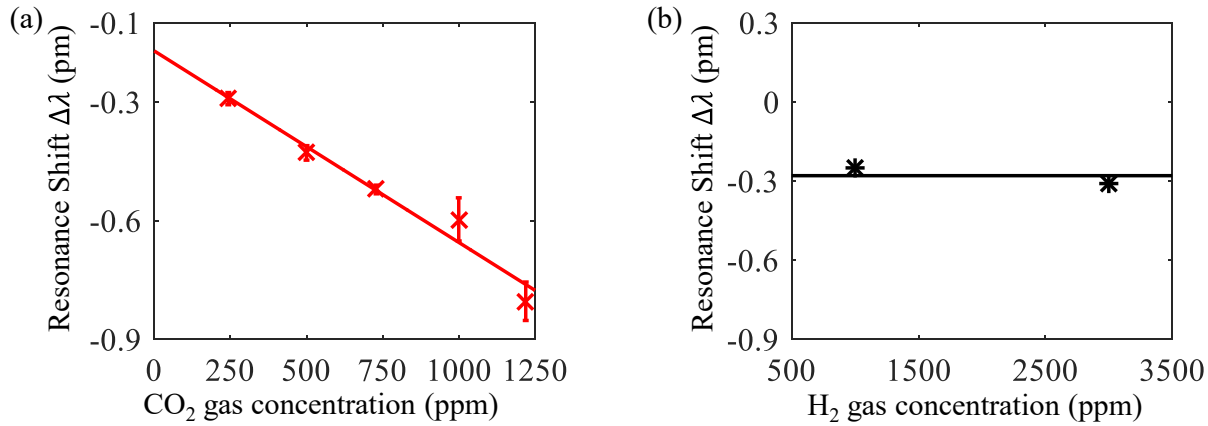


Figure 3.10 Response of the PHMB-MRR on the dual-gas sensor chip: (a) Plot of calculated resonance wavelength shifts vs. $CO_2$ gas concentrations. The red line is the linear curve fit of the data up to 5000ppm concentration. (b) Plot of resonance wavelength shifts vs. $H_2$ concentrations.

the standalone sensor in chapter 2 (±20pm). This higher LOD value is expected because the LOD depends on the sensitivity, for which the standalone sensor in Chapter 2 has better performance.

From Figure 3.10(b) we observe that the PHMB-MRR exhibits a small blue shift in the resonant wavelength upon exposure to $H_2$ gas, although this response is nearly independent of the $H_2$ gas concentration over the range tested. The average wavelength shift is 0.28±0.03pm. This blue resonance shift is most likely due to the thermo-optic response of the PHMB film to a slight temperature change caused by the gas flow. We recall from Figure 3.9 that the Ref-MRR experiences small red shifts in the resonant wavelength upon exposure to $H_2/N_2$ and $CO_2/N_2$ gas mixtures, which correspond to temperature increases of about 0.01˚C. Since polymeric materials commonly have negative thermo-optic coefficients, it is likely that the index of the PHMB layer decreases with increasing temperature, thereby offsetting the effect of the index increase in the silicon core. The net result is a slight blue shift in the resonant wavelength of the PHMB-MRR observed in Figure 3.10(b).

We previously showed in Chapter 2 that PHMB has excellent selectivity against $H_2$, even at a high concentration of 5000 ppm. The average wavelength shift of 0.28pm of the PHMB-MRR in the presence of $H_2$ gas can be regarded as the noise floor of measurements of $CO_2$ concentration by the PHMB-MRR. Since the sensitivity of the PHMB-MRR to $CO_2$ is $7.62\times10^{-4}$pm/ppm, this noise floor means that our dual-gas sensor cannot measure $CO_2$ gas concentrations more accurately than about 370ppm.

### *3.4.4 Response of Pd-MRR to separate $CO_2$ and $H_2$ gases*

In Figure 3.11(a), we plot the resonance wavelength shift of the Pd-MRR versus $H_2$ gas concentration over the 0 – 5000ppm range. The Pd-MRR exhibited a blue shift in the resonance wavelength which is linearly correlated to the $H_2$ gas concentration. The sensitivity is calculated to be $9.14\times10^{-4}$pm/ppm, which is slightly smaller than the value of $1.90\times10^{-3}$pm/ppm obtained for the standalone Pd-MRR in Section 3.4.1. The difference is mainly due to the fact that the Pd microdisk in the standalone sensor was closer to the resonator waveguide due to fabrication offset, resulting in higher sensitivity. The error bars in Figure 3.11(a) represent the standard deviations of three measurements of the resonance shifts, from which we calculated the uncertainty in the wavelength measurements to be ±7.8%. This value represents the resolution of the Pd-MRR for detection of $H_2$ in the concentration range of 0 - 5000ppm. We also note that $H_2$ gas has a Lower Explosive Limit (LEL) of 4% (40,000ppm). Our dual-gas sensor is thus capable of detecting $H_2$ concentrations well below the LEL, making it suitable for providing early detection of harmful $H_2$ gas levels.

The Pd-MRR has a lower $H_2$ detection threshold of 1000ppm. Below this concentration level, the change in the transmitted power is at the noise level and cannot be used to accurately determine the resonance wavelength shift. This lower detection threshold may be improved by increasing the thickness of the Pd layer as well as the radius of the Pd microdisk to obtain stronger interaction between the optical mode and the functional layer.

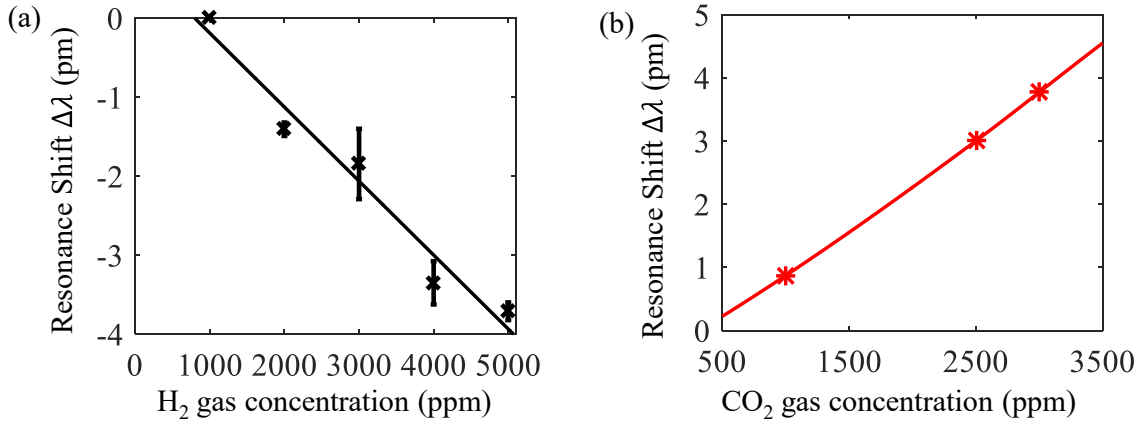


Figure 3.11 Response of the Pd-MRR on the dual-gas sensor chip: (a) Plot of calculated resonance wavelength shifts vs. $H_2$ gas concentrations. The black line is the linear curve fit of the data up to 5000ppm concentration. (b) Plot of resonance wavelength shifts vs. $CO_2$ concentrations.

From Figure 3.11(b), we observe that upon exposure to $CO_2$ gas, the Pd-MRR exhibits a red shift in the resonance wavelength which is correlated to the $CO_2$ gas concentration. This behaviour is consistent with the response obtained with the standalone Pd-MRR in Section 3.4.1. However, for the dual-gas sensor, the response of the Pd-MRR to $CO_2$ gas concentration is fairly linear, which allows us to determine the cross-sensitivity of the Pd-MRR sensor to $CO_2$ to be $S_{\lambda,CO_2}$ = $1.21\times10^{-3}$pm/ppm. Given a $H_2/CO_2$ gas mixture with a known $CO_2$ concentration ($C_{CO_2}$), we can use the Pd-MRR response to determine the $H_2$ concentration ($C_{H_2}$) according to the formula:

$$C_{H_2} = (\Delta\lambda - S_{\lambda,CO_2} C_{CO_2})/S_{\lambda,H_2} \quad (3.1)$$

where $\Delta\lambda$ is the measured wavelength shift of the Pd-MRR and $S_{\lambda,H_2}$ is the sensitivity of the Pd-MRR to $H_2$ and $S_{\lambda,CO_2}$ is its cross-sensitivity to $CO_2$. In the operation of the dual-gas sensor, the $CO_2$ concentration in the gas mixture is measured by the PHMB-MRR. In Table 3.2, we summarise the performance of the dual-gas sensor and the standalone sensors for $CO_2$ and $H_2$ gas detection. The Ref-MRR showed constant redshift response to both gases at various concentrations, which could be used to establish the noise floor of the sensing system. The two sensing channels (PHMB-MRR and Pd-MRR) of the dual-gas sensor have consistent performance in terms of sensitivity to $CO_2$ and $H_2$ gases when compared to the responses of the respective standalone sensors.

| | | **Sensitivity** Target Gas | **Cross-Sensitivity** Interfering Gas | **Uncertainty** |
|---|---|---|---|---|
| **Ref-MRR** | $CO_2$ | Constant 0.41pm | N/A | ±0.2 pm |
| | $H_2$ | Constant 0.45pm | N/A | ±0.1 pm |
| **PHMB** (For $CO_2$) | Standalone (240nm) | $2.4\times10^{-3}$ pm/ppm (0-2500ppm) | Not Measurable | ±20 ppm (@50ppm) |
| | PHMB-MRR (610nm) | $7.62\times10^{-4}$ pm/ppm (0-1250ppm) | Constant -0.3pm (500-3500ppm) | ±39 ppm (0-1250 ppm) |
| **Pd** (For $H_2$) | Standalone | $1.90\times10^{-3}$ pm/ppm (0-5000ppm) | Red shift with correlation to $C_{CO2}$ | $\sigma_\lambda$ = ±7.8% (0-5000ppm) |
| | Pd-MRR | $9.14\times10^{-4}$ pm/ppm (0-5000ppm) | Red shift $1.21\times10^{-3}$(pm/ppm) | $\sigma_\lambda$ = ±9.8% (0-5000ppm) |

Table 3.2 Performance summary of the standalone sensors and the dual-gas sensor for $CO_2$ and $H_2$ gas

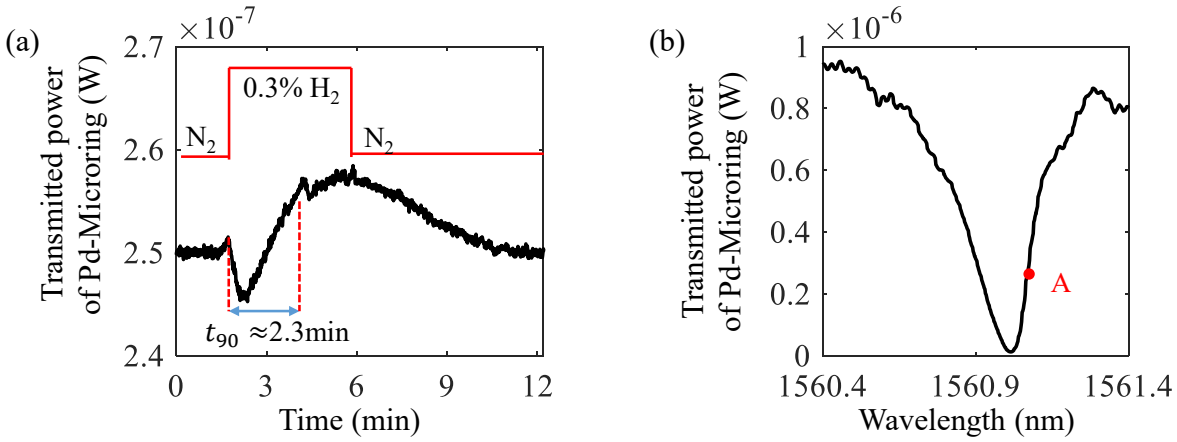


Figure 3.12 (a) Time response of the transmitted power of the Pd-MRR at a fixed wavelength (indicated by point A in the spectrum), in response to a 4-minute $H_2$ gas pulse at 3000ppm. The gas flow sequence is indicated by the red trace, with 2 minutes of $N_2$, 4 minutes of 3000ppm $H_2$ and finally 6 minutes of $N_2$ to regenerate the Pd thin film. (b) The spectrum of the Pd-MRR measured prior to the gas sensing experiment. The operation wavelength is chosen to be 1561.01nm indicated by point A, locating on the rising edge of the resonance spectrum.

Figure 3.12(a) shows the time-domain response of the transmitted power of the Pd-MRR subject to a 4min pulse of $H_2$ gas at 3000ppm. The operation wavelength was tuned to 1561.01nm, which is located on the right shoulder of the resonance arm as indicated by point A in Figure 3.12(b). Initially there is a small drop in the transmitted power at the beginning of $H_2/N_2$ gas mixture flow, which corresponds to a small red shift of the resonance spectrum. This transient power drop is attributed to the thermos-optic response of the Pd-MRR due to a small temperature difference of the two gas lines. After the initial drop, the transmitted power begins to increase, which corresponds to a blue shift of the resonance spectrum. When the $H_2$ gas is turned off and $N_2$ is flowed into the chamber, the transmitted power falls back to the baseline. The rise time $t_{90}$ of the response of Pd-MRR to $H_2$ gas is determined to be about 2.3mins

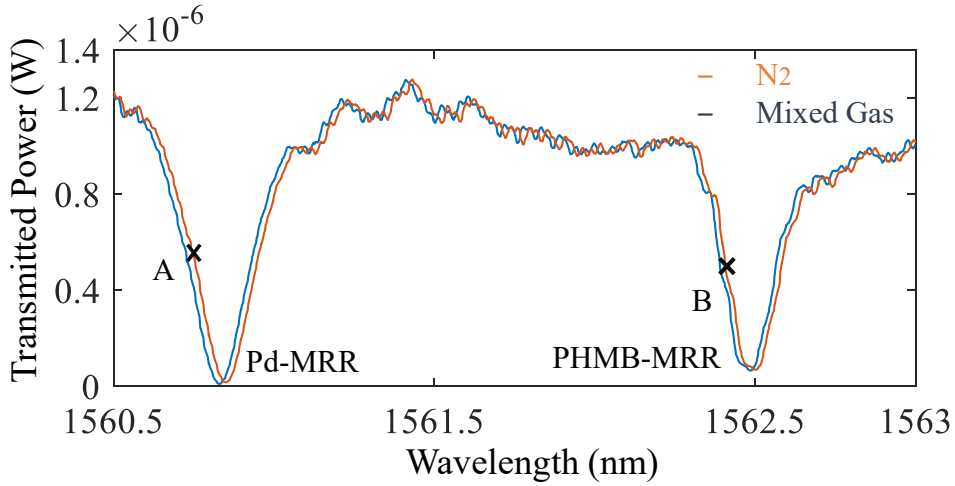


Figure 3.13 Measured resonance spectra of the Pd-MRR and PHMB-MRR on the dual-gas sensor chip. Red curve is the initial spectrum in $N_2$ gas; blue curve is the spectrum in the presence of a mixture of 2% $H_2$ and 0.5% $CO_2$ gases.

### *3.4.5 Response of the dual-gas sensor to a mixture of $H_2$ and $CO_2$ gases*

In this section we demonstrate the simultaneous detection of $H_2$ and $CO_2$ gases using the dual-gas sensor. We employed the experimental setup in Figure 3.7 to measure the spectral response of the PHMB-MRR and Pd-MRR in the presence of a mixture of 2% $H_2$ and 0.5% $CO_2$ in $N_2$. The mixture was supplied from a certified standard gas tank containing both $H_2$ and $CO_2$ at the afore-specified concentrations. After preconditioning the sealed gas chamber with 200sccm-flow of $N_2$ for 10 minutes, the baseline spectra of the Pd-MRR and PHMB-MRR were measured. The result is shown by the red curve in Figure 3.13. Next we introduced 200sccm flow of the gas mixture into the chamber and monitored the output response of Pd-MRR for 10 minutes. After the sensor response had stabilized, we measured the transmission spectra of the Pd-MRR and PHMB-MRR again. The result is shown by the blue curve in Figure 3.13. We observe that the resonance spectra of the Pd-MRR and the PHMB-MRR are blue-shifted by different amounts, 9pm and 3pm, respectively, upon exposure to the gas mixture. The shapes of the resonance spectra, however,

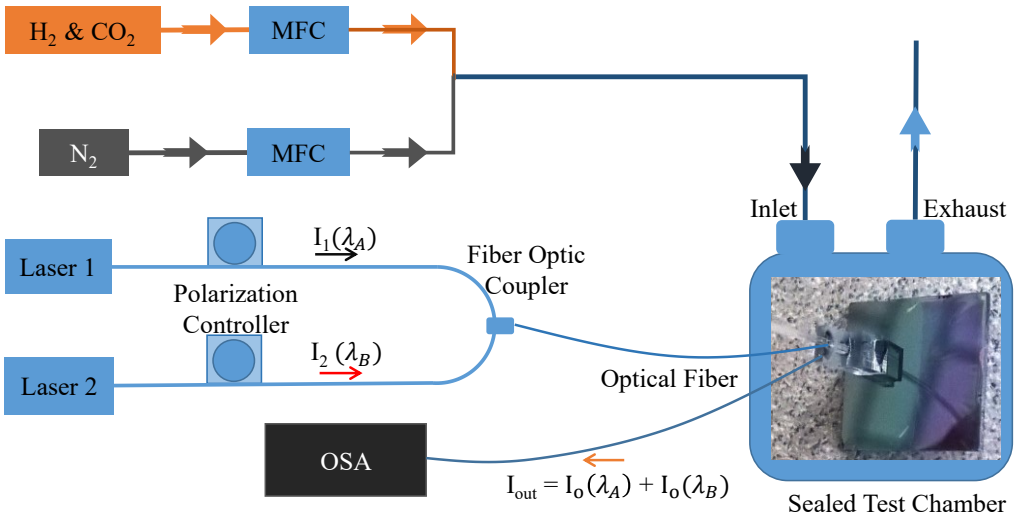


Figure 3.14 Schematic of the experimental setup using two laser sources and an OSA for monitoring the time response of the dual-gas sensor to a mixture of $H_2$ and $CO_2$ gases.

remain unchanged before and after exposure to the gas mixture, indicating that the gases induced negligible extra loss.

The red and black curves in Figure 3.15 show the transmitted power of the Pd-MRR and PHMB-MRR, respectively, as a function of time. We observe that the transmitted powers of both microrings decrease upon the introduction of the gas mixture, then rise back again during the regeneration period when $CO_2$ and $H_2$ are released from the PHMB and Pd functional coatings. Since the operating wavelengths are located on the left shoulders of the resonance spectra, the drops in the transmitted powers upon exposure to the gas mixture correspond to blue shifts in the resonance wavelengths, in agreement with the results in Figure 3.13. The corresponding resonance shifts are 11pm for the Pd-MRR and 2.35pm for the PHMB-MRR. The resonance shift due to $H_2$ alone can be estimated to be ~16pm using the sensitivity $S_{\lambda,H_2}$ obtained from Figure 3.11(a). Then, according to Equation (3.1), the wavelength shift of Pd-MRR for 2% $H_2$ in the presence of 0.5% $CO_2$ will be 12pm, which is in agreement with what we have observed in the experiment.

We also note that the time trace of the Pd-MRR does not fully return to the initial baseline after the gas mixture is turned off, indicating that the Pd thin film did not return to its initial state. This irreversible change of Pd lattice typically occurs at $H_2$ concentrations over 1% due to the irreversible phase transition of the Pd-H system and has been reported for other Pd-based optical

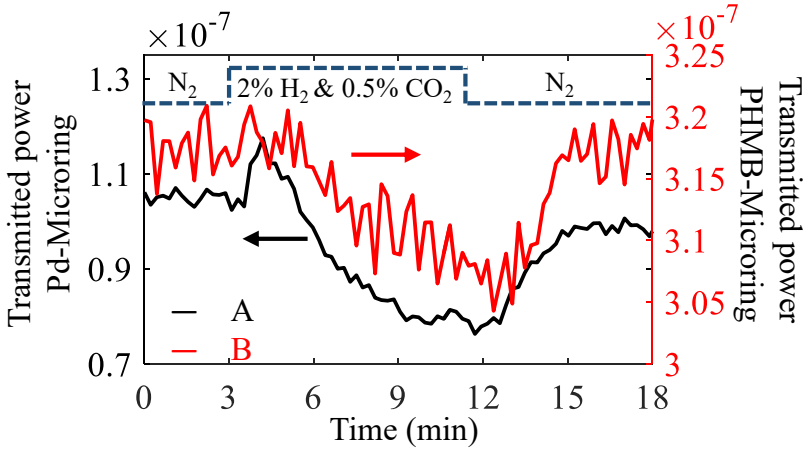


Figure 3.15 Time response of the transmitted power of the dual-gas sensor to 6-minute pulse of mixed gas consisting of 0.5% $CO_2$ and 2% $H_2$ gas balanced in $N_2$. The black trace shows the response of the Pd-MRR while the red trace shows the response of the PHMB-MRR. The operation wavelengths of the two microring sensors are as indicated by points A and B in Figure 3.13. The gas flow sequence is indicated by the blue dashed trace.

hydrogen sensors in terms of hysteresis phenomenon [67, 69]. Heating Pd to above 300℃ could reverse this lattice phase transition but may not be suitable for some applications. Another approach to supress such irreversible change is by employing Ni to form Pd-Ni alloy as the functional material, but at the cost of reduced sensitivity [84].

### 3.5 Summary

In this chapter, we designed, implemented and experimentally demonstrated the operation of a silicon photonic dual-gas sensor using arrayed microring resonators functionalized with PHMB and Pd for $CO_2$ and $H_2$ gas sensing. A functionalization process was developed to selectively deposit the two different types of functional materials on the microring resonators. Gas sensing experiments were performed to evaluate the response of each microring sensor to separate $CO_2$ and $H_2$ gases. While PHMB was shown to provide good selectivity of $CO_2$ against $H_2$ gas, a significant level of cross-sensitivity to $CO_2$ gas was observed for Pd for both the standalone Pd-MRR and the dual-gas sensor. We discussed how this cross-sensitivity can be taken account in the measurement of $H_2$ gas concentration by the Pd-MRR on the dual-gas sensor. Finally, we also investigated the response of the dual-gas sensor to a gas mixture to demonstrate its ability to simultaneously detect $CO_2$ and $H_2$ gases.

# Chapter Four.

# A Differential Ellipsometric Method for Chiral Sensing

## 4.1 Introduction

Chirality influences the behaviours of living organisms in many ways. Chiral compounds are what give rise to the specific smells and tastes that an organism experiences. Chirality also dictates the functionalities of the enzymes which it relies on for metabolism. Amino acids, a most import building block that keeps life propagating, have the same left-handed sense of chirality [85]. In general, the physical and chemical properties of a compound are determined not only by its chemical formula but also by how the atoms are structurally arranged, i.e., by the stereochemistry of the molecule.

Chirality refers to the stereochemical property of molecules that have non-superimposable mirror images, like the left and right hands. Two molecules that are mirror images of each other are referred to as left-handed and right-handed enantiomers. These molecules have the same chemical formula and atom constitution but differ in their three-dimensional (3D) structures, or conformations. It is these 3D structures which determine the different behaviours of the enantiomers. Many natural chiral compounds exist in both left- and right-handed conformations. Enantiomers have the same physical properties but may exhibit significant differences in their chemical interactions with other molecules, which lead to their different biochemical characteristics in terms of pharmacology, toxicology, pharmacokinetics, and metabolism. For example, L-carvone smells like mint while its mirror image R-carvone smells like caraway [86].

Chirality is also directly related to the secondary structure of large organic molecules such as proteins.

Given the influence of chirality on the functionalities of biochemical molecules, the detection and analysis of chiral compounds have drawn significant interest in biochemistry research, pharmacology and drug discovery. For example, in the production of drugs and food additives, it is often important to determine the enantiomeric purity of chiral compounds. More than half of the drugs currently in use consist of chiral compounds, among which 90% contain both enantiomers in equal concentrations [87, 88]. Due to the different biological activities of enantiomers, enantiopure drugs (i.e., drugs that contain only one type of enantiomer) can offer the advantages of more efficient treatment and less toxic side effects [87].

Optically, chirality manifests itself in the different ways left and right circularly polarized light interact with a chiral medium. One of the most common ways for analyzing chirality is by measuring the optical activity of the material. For example, polarimetry and circular dichroism spectroscopy are two popular optical methods for measuring the chiral parameter of a chiral material. These methods will be discussed in more detail in Section 4.2. Recently, methods based on measurement of optical rotation from light reflection at a chiral surface [89, 90] or from light interaction with surface plasmons [91] have also been developed.

The objective of this chapter is to modify the standard ellipsometric method so that it can be used to characterize the chirality of a material over a broad wavelength range. The method exploits the enhanced chiral signature of light reflection near the critical angle to obtain accurate measurement of the optical rotation of the chiral material. One of our main contributions is to develop a differential technique for determining the chiral parameter which reduces the effect of system noise and thus improves measurement precision. In particular, the enhanced signal-to-noise ratio (SNR) of the differential method eliminates the need for high-power tunable laser sources so that lamp light sources can be used for broadband characterization of chiral materials. This enables the method to be implemented in a standard commercial spectroscopic ellipsometer, which typically uses a lamp source. To demonstrate the technique, we use a commercial ellipsometer with a QTH lamp to measure the optical rotatory dispersion (ORD) of sucrose solution over the 500-1000nm wavelength range. The measured ORD spectrum can also be used to calculate the circular dichroism (CD) spectrum of the medium using the Kramers-Kronig (KK) relation [18, 92]. The proposed differential ellipsometric method thus potentially provides a robust

and versatile tool for characterizing chiral compounds for biochemistry research, drug discovery and other applications in the health sciences.

This chapter is organized as follows. We first give a review of existing technologies for chiral sensing in Section 4.2. This is followed by a review of the theory of electromagnetic wave propagation in a chiral medium in Section 4.3, laying the foundation for the analysis of optical structures with embedded chiral materials. In Section 4.4, we will derive a general transfer matrix formalism for analyzing light reflection and transmission at the interface between an achiral and a chiral medium. The transfer matrix is used in Section 4.5 to develop a differential ellipsometric method for chiral sensing based on reflection from an achiral-chiral interface near the critical angle of incidence. In Section 4.6, the method is implemented in a commercial ellipsometry system and validated with the measurement of the optical rotation spectrum of a sucrose solution. A summary of the work is given in Section 4.7.

## 4.2 Review of Chiral Sensing Technologies

There are in general three main methods for chiral sensing, namely, polarimetry, circular dichroism spectroscopy and enantio-selective sensors. Each of these methods is reviewed below.

*Polarimetry*

Polarimeters commonly find application in quality control laboratories and process areas in food and fragrance industries. Polarimetric detectors are also often integrated with High Performance Liquid Chromatography, which is the most widely used technique in analytic chemistry. A polarimeter detects the rotation angle of a linearly polarized (LP) light passing through a chiral sample. Any LP light can be decomposed into a combination of left circularly polarized (LCP) and right circularly polarized (RCP) light components. When propagating in a chiral medium, the two components experience different phase changes due to their different refractive indices. This phase difference subsequently rotates the linear polarization of the output light relative to the input polarization.

Since the chirality of naturally-occurring chiral substances is typically small, polarimeters require a long sample cell in order to obtain a detectable polarization rotation angle. Researchers have also reported polarimetry constructions with optical fibers. For example, a hollow-core photonic crystal fiber (HC-PCF) filled with liquid analyte was used to sense the chirality of (-)-

fructose [12]. Vollmer and Fisher reported in [93] a chiral detection scheme based on a fiber-loop ring resonator. The circular birefringence of the chiral sample causes a difference in the resonant frequencies of the LCP and RCP light modes. In contrast to conventional polarimeters, fiber ring sensors eliminate the dependence of sensitivity and limit of detection on the sample size, allowing for device miniaturization and the use of small sample volumes.

*Circular dichroism spectroscopy*

Circular dichroism (CD) refers to the differential absorption of LCP and RCP light waves in a chiral medium. The difference in the absorbance $A_{\mathrm{L}}$ and $A_{\mathrm{R}}$ of LCP and RCP waves can be expressed using the Beer-Lambert's law as [4]

$$\Delta A(\lambda) = A_L(\lambda) - A_R(\lambda) = (\varepsilon_{\mathrm{L}}(\lambda) - \varepsilon_{\mathrm{R}}(\lambda)) \times cL = \Delta\varepsilon(\lambda) cL \tag{4.1}$$

where $\varepsilon_{\mathrm{L/R}}(\lambda)$ is the molar absorption coefficient of LCP/RCP light, $L$ is the path length of the sample cell, and $c$ is the sample molar concentration. CD spectroscopy is well recognized for its sensitivity to the structure of organic chiral molecules, especially proteins. It is now a standard analytical method for studying the secondary structure of proteins, and for monitoring protein conformation changes under different conditions such as temperature and pH, solvent composition variation, and ligand binding. Initially CD was studied in the ultra-violet (UV) and visible wavelength ranges, where electronic transitions caused by photon absorption are the underlying mechanism for the differential polarization absorption [4]. Investigation of CD has since been extended to the infrared region, where vibrational transitions give rise to Vibrational CD (VCD) [94]. However, VCD signals in the mid-infrared wavelength range are generally three orders of magnitude smaller than those in the UV and visible CD spectra.

Recently localized surface plasmon resonances (SPRs) in metal nanoparticles were exploited to excite a new type of CD peaks caused by chiral molecules immobilized on the nanoparticle surface [91]. It was shown that the interaction between the chiral molecules and the SPRs can enhance the chiroptical activity of the molecules, giving rise to amplified CD spectral response. Furthermore, this SPR-CD spectrum exhibits a new peak at longer wavelengths, close to the intrinsic plasma frequency of the metal. The authors in [91] argued that this new peak originates from the real part of the chiral parameter while conventional CD comes from its imaginary part. Therefore, it was suggested that information about the complex chirality parameter can be obtained with a single SPR-CD measurement.

*Enantioselective sensors*

Enantioselective sensors are one of the major types of sensors for detecting concentrations of chiral compounds and the enantiomeric excess, which measures the extent to which one particular enantiomer dominates in the mixture. These sensors employ chiral selectors as functional materials that preferentially recognize one enantiomer over its mirror-image molecule. They exhibit a change in physical properties such as dielectric constant [95], mass [96] and fluorescence [97], which can be detected using appropriate interrogation techniques. For example, a potentiometric sensor with synthesized chiral polyaniline was reported in [98] for sensing one isomer in racemic phenylalanine (Phe) by measuring the different potential responses to the L- and D-(Phe) enantiomers. A chiral fluorescent metal-organic framework was synthesised in [97] for enantioselective sensing of four pairs of chiral amino alcohols, showing different relations of the fluorescent signal intensity to the enantiomer concentration. In general, enantioselective sensors can only provide information about the concentration of the chiral molecules but not the strength of their chirality, which may also be important for structural analysis and for understanding their biochemical functionalities.

## 4.3 Light Propagation in a Chiral Medium

As previously discussed, chirality manifests itself in the optical activity of a material, which causes LCP and RCP light waves to interact differently with the chiral medium. This optical property of enantiomers can be exploited for the detection of chirality. In order to see how this can be achieved, we must first understand the behaviour of light in a chiral medium. Toward this aim, we discuss below the electromagnetic formalism used to describe light propagation in a chiral medium.

From a macroscopic point of view, optical activity arises from the coupling of electric and magnetic fields of light as it propagates through a chiral medium. Thus, in a chiral medium the electric and magnetic induction fields (**D** and **B**) can no longer be simply related to the electric and magnetic fields (**E** and **H**) by the permittivity $\varepsilon_c$ and permeability $\mu_c$. Instead researchers have proposed new constitutive relations to express the coupling of electric and magnetic fields induced by the chirality of the medium. Condon introduced a chirality factor $g$ to describe this coupling phenomenon and rewrote the constitutive relations as [2]

$$\mathbf{D} = \varepsilon_c \mathbf{E} - g\,\partial \mathbf{H}/\partial t\,, \tag{4.2}$$

$$\mathbf{B} = \mu_c \mathbf{H} + g\,\partial \mathbf{E}/\partial t\,. \tag{4.3}$$

Silverman [1] later expressed the constitutive relations for monochromatic waves with time dependence $\exp(j\omega t)$ as

$$\mathbf{D} = \varepsilon_c \mathbf{E} - j\,\kappa/c_0 \mathbf{H}, \quad \mathbf{B} = j\,\kappa/c_0\,\mathbf{E} + \mu_c \mathbf{H}\,, \tag{4.4}$$

where $\kappa = \omega g/c_0$ and $c_0$ is the speed of light in vacuum. This set of constitutive relations is now widely adopted in metamaterial research. The formalism we follow in this thesis was introduced by S. Bassiri *et al*. in their extensive work on light propagation in chiral media [99],

$$\mathbf{D} = \varepsilon_c \mathbf{E} - j\xi \mathbf{B}, \quad \mathbf{H} = -j\xi \mathbf{E} + \mathbf{B}/\mu_c\,, \tag{4.5}$$

which are commonly used in optics. The chiral admittance $\xi$, which is in general complex, is related to the parameter $\kappa$ in Equation (4.4) by $\kappa = \xi \mu_c c_0$. In this thesis we assume non-magnetic media so $\mu_c = \mu_0$.

By substituting the chiral constitutive relations in Equation (4.5) into Maxwell's equations, we obtain the following coupled wave equations for wave propagation in a bulk chiral medium:

$$\nabla^2 \begin{pmatrix} \mathbf{E} \\ \mathbf{H} \end{pmatrix} + (1 + 2\chi^2) n_c^2 k_0^2 \begin{pmatrix} \mathbf{E} \\ \mathbf{H} \end{pmatrix} + \begin{pmatrix} -2j\xi k_0^2 / \eta_0^2 \mathbf{H} \\ 2j\xi(1+\chi^2) n_c^2 k_0^2 \mathbf{E} \end{pmatrix} = 0\,, \tag{4.6}$$

where $n_c = \sqrt{\varepsilon_c / \varepsilon_0}$ is the refractive index of the chiral material, $\eta_0 = \sqrt{\varepsilon_0 / \mu_0}$ is the admittance of free space, and $\chi = \xi / \eta_c$ is the normalized chirality admittance ($\eta_c = n_c \eta_0$). In this thesis, we will refer to $\chi$ simply as the chiral parameter, which can take on complex values.

Consider now a plane wave propagating in the $z$ direction with field dependence $E_z(z,x) \sim$ . The solution for the longitudinal field component $E_z$ may be expressed as a superposition of two modes $U_1(x)$ and $U_2(x)$ [99],

$$E_z = U_1(x) + U_2(x)\,. \tag{4.7}$$

Using Maxwell's equations, we obtain the corresponding magnetic field $H_z$ as

$$H_z = j\eta_c \sqrt{1+\chi^2}\,[U_1(x) - U_2(x)]\,. \tag{4.8}$$

Substituting the above expressions for $E_z$ and $H_z$ into Equation (4.6), we get the equations for $U_1(x)$ and $U_2(x)$,

$$\frac{d^2U_{1(2)}}{dx^2} + (k_{+(-)}^2 - \beta^2)U_{1(2)} = 0, \tag{4.9}$$

where $k_{\pm} = n_{\pm}k_0 = n_c(\pm\chi + \sqrt{1+\chi^2})k_0$. The solutions to the above wave equations are

$$U_1 = C_1 e^{-k_{x1}x} \text{ and } U_2 = C_2 e^{-k_{x2}x}, \tag{4.10}$$

with $k_{x1(x2)} = \sqrt{\beta^2 - k_{+(-)}^2}$.

From the solutions for $U_1$ and $U_2$ and using Maxwell's equations, we can determine the transverse electric field components ($E_x$, $E_y$) to be

$$E_x = -(j\beta / k_{x1})C_1 e^{-k_{x1}x} - (j\beta / k_{x2})C_2 e^{-k_{x2}x}. \tag{4.11}$$

$$E_y = -(k_+ / k_{x1})C_1 e^{-k_{x1}x} + (k_- / k_{x2})C_2 e^{-k_{x2}x}. \tag{4.12}$$

The above solutions contain two sets of waves, one with transverse wave vector $k_{x1}$ and transverse field amplitude $[E_x, E_y] = [\beta/k_{x1}, -j\,k_+/k_{x1}]C_1$, and the other with transverse wave vector $k_{x2}$ and transverse field amplitude $[E_x, E_y] = [\beta/k_{x2}, j\,k_-/k_{x2}]C_2$. We identify the first wave as an LCP wave with propagation constant $k_+$ and the second wave as an RCP wave with propagation constant $k_-$. We can define the index of refraction seen by the LCP and RCP waves as $n_+ = k_+/k_0$ and $n_- = k_-/k_0$, respectively. For $\chi \ll 1$, we have $n_{\pm} \approx n_c(1 \pm \chi)$.

An LP wave can be considered to be the superposition of two RCP and LPC waves with equal amplitudes. After propagating a distance $L$ in a transparent chiral medium with real-valued $\chi$, the two circularly polarized components acquire a phase difference of $\exp(2jn_c\,\mathrm{Re}\{\chi\}k_0L)$, resulting in a rotation of $n_c\,\mathrm{Re}\{\chi\}\,\mathrm{k}_0\,L$ in the polarization plane of the incident LP wave. Thus the real part of the chiral parameter $\chi$ is responsible for the optical rotation (OR) effect. On the other hand, the imaginary part of $\chi$ is responsible for the circular dichroism effect. If the chiral medium is absorbing with complex refractive index $n_c$ and an imaginary-valued $\chi$, then after propagating a distance $L$, the LCP and RCP components will experience an absorption difference of $\exp(-4n_c\,\mathrm{Im}\{\chi\}k_0L)$, which changes the incident LP wave into an elliptically polarized wave. Its ellipticity $\theta$ in CD unit is given by

$$\theta = 4n_c\,\mathrm{Im}\{\chi\}k_0L \times 32.982\log(e). \tag{4.13}$$

## 4.4 Transfer Matrix Analysis of an Achiral-Chiral Interface

In this section, we derive a general transfer matrix for light reflection from the interface between an achiral (dielectric) medium and a chiral medium. Using the transfer matrix, the reflection coefficients of an achiral-chiral interface are then determined and analyzed to identify the effects of chirality on the reflection spectrum. These effects will be later employed for ellipsometric measurement of the chiral parameter.

### *4.4.1 General transfer matrix of an achiral-chiral interface*

The reflection and refraction of light at a chiral interface have been extensively investigated in the past. Silverman was the first to derive the Fresnel reflection coefficients of light incident on an achiral-chiral interface [1]. The transfer matrix method has also been employed to investigate the reflection and transmission of circularly polarized light at a chiral-chiral interface [100] and of linearly polarized light incident on an achiral-chiral interface [101]. In our work, we are interested in light transmission through a multi-layer structure which consists of interfaces between a dielectric and a chiral medium (this chapter), as well as between a metal and a chiral medium (Chapter 5). To facilitate the analysis of these structures, we derive below a general transfer matrix for an achiral-chiral interface which can relate two different states of polarizations in the two media, namely, linearly polarized (LP) light in the achiral medium and circularly polarized (CP) light in the chiral medium.

We consider an interface at $x = 0$ which separates an achiral medium on the left and a chiral medium on the right, as illustrated in Figure 4.1. The achiral medium has refractive index $n_a$ while the chiral medium is characterized by refractive index $n_c$ and chiral parameter $\chi$. In the achiral medium, we assume an incident LP field $\mathbf{E}_1^{(a)}$ and a reflected LP field $\mathbf{E}_2^{(a)}$ represented by the Jones vectors

$$\mathbf{E}_1^{(a)} = \begin{bmatrix} E_{1,\mathrm{s}}^{(a)} \\ E_{1,p}^{(a)} \end{bmatrix}, \tag{4.14}$$

$$\mathbf{E}_2^{(a)} = \begin{bmatrix} E_{2,\mathrm{s}}^{(a)} \\ E_{2,p}^{(a)} \end{bmatrix}, \tag{4.15}$$

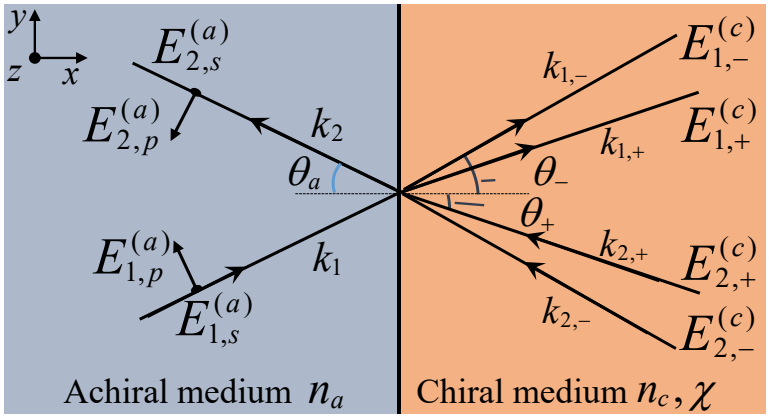


Figure 4.1 Reflection and refraction at an achiral-chiral interface

where $E_{i,p}^{(a)}$ and $E_{i,s}^{(a)}$ ($i$ = 1,2) represent the electric field amplitude of the $p$- and $s$-polarized component, respectively. In the chiral medium, we assume an incident CP field $\mathbf{E}_2^{(c)}$ and a reflected CP field $\mathbf{E}_1^{(c)}$ represented by

$$\mathbf{E}_1^{(c)} = \begin{bmatrix} E_{1,+}^{(c)} \\ E_{1,-}^{(c)} \end{bmatrix}, \tag{4.16}$$

$$\mathbf{E}_2^{(c)} = \begin{bmatrix} E_{2,+}^{(c)} \\ E_{2,-}^{(c)} \end{bmatrix}, \tag{4.17}$$

where $E_{i,+}^{(c)}$ and $E_{i,-}^{(c)}$ ($i = 1,2$) represent the electric field amplitude of the LCP and RCP component, respectively. The LCP and RCP waves in the chiral medium experience different refractive indices given by $n_+$ and $n_-$, respectively. The angles of reflection $\theta_+$ and $\theta_-$ shown in Figure 4.1 are also different. Specifically, the incident LCP wave $E_{1,+}^{(c)}$ is reflected into two CP waves $E_{2,\pm}^{(c)}$ at the angles $\theta_\pm$ satisfying the relation

$$n_+ \sin(\theta_+) = n_\pm \sin(\theta_\pm)\,. \tag{4.18}$$

A similar expression applies to the incident RCP wave $E_{1,-}^{(c)}$. The incident LP wave $\mathbf{E}_1^{(a)}$ from the achiral medium will be refracted into the pair of LCP and RCP waves $E_{1,+}^{(c)}$ and $E_{1,-}^{(c)}$ at the refraction angles $\theta_\pm$ governed by the Snell's law

$$n_a \sin(\theta_a) = n_\pm \sin(\theta_\pm)\,. \tag{4.19}$$

The above Snell's law also applies to the refraction angle $\theta_a$ of the refracted LP field $\mathbf{E}_2^{(a)}$ due to the incident CP field $\mathbf{E}_2^{(a)}$ from the chiral medium.

Next we apply the continuity boundary condition to the tangential electric and magnetic fields at the interface. In the achiral medium, the tangential **E** and **H** fields are

$$\mathbf{E}_{1,\mathrm{T}}^{(a)} = \begin{bmatrix} E_{1,\mathrm{s}}^{(a)} \\ \dfrac{k_{xa}}{k_a} E_{1,p}^{(a)} \end{bmatrix}, \ \mathbf{H}_{1,\mathrm{T}}^{(a)} = \begin{bmatrix} -\eta_a \dfrac{k_{xa}}{k_a} E_{1,\mathrm{s}}^{(a)} \\ \eta_a E_{1,p}^{(a)} \end{bmatrix} \tag{4.20}$$

$$\mathbf{E}_{2,\mathrm{T}}^{(a)} = \begin{bmatrix} E_{2,\mathrm{s}}^{(a)} \\ -\dfrac{k_{xa}}{k_a} E_{2,p}^{(a)} \end{bmatrix}, \ \mathbf{H}_{2,\mathrm{T}}^{(a)} = \begin{bmatrix} \eta_a \dfrac{k_{xa}}{k_a} E_{2,\mathrm{s}}^{(a)} \\ \eta_a E_{2,p}^{(a)} \end{bmatrix}, \tag{4.21}$$

where $\eta_a = n_a \eta_0, k_a = n_a k_0,$ and $k_{xa} = k_a \cos\theta_a$ . Using Maxwell's equations and the chiral constitutive relation in Equation (4.5), we also obtain the tangential fields of the CP waves in the chiral medium (for a detailed derivation the reader is referred to Appendix II):

$$\mathbf{E}_{1,\pm\mathrm{T}}^{(c)} = \begin{bmatrix} 1 \\ \pm j \dfrac{k_{x+}}{k_+} \end{bmatrix} E_{1,\pm}^{(c)}, \quad \mathbf{H}_{1,\pm\mathrm{T}}^{(c)} = \begin{bmatrix} -\dfrac{k_{x+}}{k_+} \eta_{ce} \\ \pm j\eta_{ce} \end{bmatrix} E_{1,\pm}^{(c)}, \tag{4.22}$$

$$\mathbf{E}_{2,\pm\mathrm{T}}^{(c)} = \begin{bmatrix} 1 \\ \mp \end{bmatrix} E_{2,\pm}^{(c)}, \quad \mathbf{H}_{2,\pm\mathrm{T}}^{(c)} = \begin{bmatrix} \dfrac{k_{x+}}{k_+} \eta_{ce} \\ \pm j\eta_{ce} \end{bmatrix} E_{2,\pm}^{(c)}, \tag{4.23}$$

where $\eta_{ce} = n_{ce}\eta_0 = \eta_0 n_c \sqrt{1+\chi^2}$ and $k_{x\pm} = k_0 \sqrt{n_\pm^2 - n_a^2 \sin^2\theta_a}$ . Applying the continuity boundary condition to the tangential fields in Equations (4.20) - (4.23), we obtain

$$E_{1,s}^{(a)} + E_{2,s}^{(a)} = E_{1,+}^{(c)} + E_{1,-}^{(c)} + E_{2,+}^{(c)} + E_{2,-}^{(c)} \tag{4.24}$$

$$\frac{k_{xa}}{k_a} E_{1,p}^{(a)} - \frac{k_{xa}}{k_a} E_{2,p}^{(a)} = j\frac{k_{x+}}{k_+} E_{1,+}^{(c)} - j\frac{k_{x-}}{k_-} E_{1,-}^{(c)} - j\frac{k_{x+}}{k_+} E_{2,+}^{(c)} + j\frac{k_{x-}}{k_-} E_{2,-}^{(c)} \tag{4.25}$$

$$-\eta_a \frac{k_{xa}}{k_a} E_{1,s}^{(a)} + \eta_a \frac{k_{xa}}{k_a} E_{2,s}^{(a)} = -\frac{k_{x+}}{k_+}\eta_{ce} E_{1,+}^{(c)} - \frac{k_{x-}}{k_-}\eta_{ce} E_{1,-}^{(c)} + \frac{k_{x+}}{k_+}\eta_{ce} E_{2,+}^{(c)} + \frac{k_{x-}}{k_-}\eta_{ce} E_{2,-}^{(c)} \tag{4.26}$$

$$\eta_a E_{1,p}^{(a)} + \eta_a E_{2,p}^{(a)} = j\eta_{ce} E_{1,+}^{(c)} - j\eta_{ce} E_{1,-}^{(c)} + j\eta_{ce} E_{2,+}^{(c)} - j\eta_{ce} E_{2,-}^{(c)} \tag{4.27}$$

We can rewrite the above boundary conditions in terms of two matrix equations

$$\mathbf{M}_1\mathbf{E}_1^{(a)} + \mathbf{M}_2\mathbf{E}_2^{(a)} = \mathbf{M}_3\mathbf{E}_1^{(c)} + \mathbf{M}_4\mathbf{E}_2^{(c)}, \tag{4.28}$$

$$\mathbf{M}_5\mathbf{E}_1^{(a)} + \mathbf{M}_6\mathbf{E}_2^{(a)} = \mathbf{M}_7\mathbf{E}_1^{(c)} + \mathbf{M}_8\mathbf{E}_2^{(c)}, \tag{4.29}$$

where

$$\begin{aligned}
\mathbf{M}_1 &= \begin{bmatrix} \frac{k_{xa}}{k_a} & 0 \\ 0 & 1 \end{bmatrix} & \mathbf{M}_2 &= \begin{bmatrix} -\frac{k_{xa}}{k_a} & 0 \\ 0 & 1 \end{bmatrix} \\
\mathbf{M}_3 &= \begin{bmatrix} j\frac{k_{x+}}{k_+} & -j\frac{k_{x-}}{k_-} \\ 1 & 1 \end{bmatrix} & \mathbf{M}_4 &= \begin{bmatrix} -j\frac{k_{x+}}{k_+} & j\frac{k_{x-}}{k_-} \\ 1 & 1 \end{bmatrix} \\
\mathbf{M}_5 &= \begin{bmatrix} n_a & 0 \\ 0 & -n_a\frac{k_{xa}}{k_a} \end{bmatrix} & \mathbf{M}_6 &= \begin{bmatrix} n_a & 0 \\ 0 & n_a\frac{k_{xa}}{k_a} \end{bmatrix} \\
\mathbf{M}_7 &= \begin{bmatrix} jn_c & -jn_c \\ -\frac{k_{x+}}{k_+}n_{ce} & -\frac{k_{x-}}{k_-}n_{ce} \end{bmatrix} & \mathbf{M}_8 &= \begin{bmatrix} jn_{ce} & -jn_{ce} \\ \frac{k_{x+}}{k_+}n_{ce} & \frac{k_{x-}}{k_-}n_{ce} \end{bmatrix}
\end{aligned}. \tag{4.30}$$

For an interface between two achiral media, the relationship between the incident LP field $\mathbf{E}_1^{(l)}$ in the left medium and the incident and reflected LP fields $\mathbf{E}_2^{(r)}$ and $\mathbf{E}_1^{(r)}$ in the right medium can be written as

$$\mathbf{E}_1^{(l)} = \mathbf{T}^{(lr)}\mathbf{E}_1^{(r)} + \mathbf{R}^{(lr)}\mathbf{E}_2^{(r)} \tag{4.31}$$

where the matrices $\mathbf{T}^{(lr)}$ and $\mathbf{R}^{(lr)}$ are given by

$$\mathbf{T}^{(lr)} = \begin{bmatrix} \frac{1}{t_p} & 0 \\ 0 & \frac{1}{t_s} \end{bmatrix} \text{ and } \mathbf{R}^{(lr)} = \begin{bmatrix} \frac{r_p}{t_p} & 0 \\ 0 & \frac{r_s}{t_s} \end{bmatrix}, \tag{4.32}$$

in which the Fresnel coefficients are [102]

$$r_p = \frac{n_r^2 k_{xl} - n_l^2 k_{xr}}{n_r^2 k_{xl} + n_l^2 k_{xr}}, \qquad t_p = \frac{2n_l n_r k_{xl}}{n_r^2 k_{xl} + n_l^2 k_{xr}} \tag{4.33}$$

$$r_s = \frac{k_{xl} - k_{xr}}{k_{xl} + k_{xr}}, \qquad t_s = \frac{2k_{xl}}{k_{xl} + k_{xr}}. \tag{4.34}$$

For an achiral-chiral interface, we solve Equation (4.25) for the fields $\mathbf{E}_1^{(a)}$ and $\mathbf{E}_2^{(a)}$ in the achiral medium to get

$$\mathbf{E}_1^{(a)} = \mathbf{T}^{(ac)}\mathbf{E}_1^{(c)} + \mathbf{R}^{(ac)}\mathbf{E}_2^{(c)}, \tag{4.35}$$

$$\mathbf{E}_2^{(a)} = \mathbf{R}^{(ac)}\mathbf{E}_1^{(c)} + \mathbf{T}^{(ac)}\mathbf{E}_2^{(c)}, \tag{4.36}$$

where the matrices $\mathbf{T}^{(ac)}$ and $\mathbf{R}^{(ac)}$ are given by

$$\mathbf{T}^{(ac)} = \begin{bmatrix} j\dfrac{n_a k_{x+} + n_+ n_{ce} k_{xa}/n_a}{2n_+ k_{xa}} & -j\dfrac{n_a k_{x-} + n_- n_{ce} k_{xa}/n_a}{2n_- k_{xa}} \\ \dfrac{n_+ k_{xa} + n_{ce} k_{x+}}{2n_+ k_{xa}} & \dfrac{n_- k_{xa} + n_{ce} k_{x-}}{2n_- k_{xa}} \end{bmatrix}, \tag{4.37}$$

$$\mathbf{R}^{(ac)} = \begin{bmatrix} j\dfrac{-n_a k_{x+} + n_+ n_{ce} k_{xa}/n_a}{2n_+ k_{xa}} & -j\dfrac{-n_a k_{x-} + n_- n_{ce} k_{xa}/n_a}{2n_- k_{xa}} \\ \dfrac{n_+ k_{xa} - n_{ce} k_{x+}}{2n_+ k_{xa}} & \dfrac{n_- k_{xa} - n_{ce} k_{x-}}{2n_- k_{xa}} \end{bmatrix}. \tag{4.38}$$

Comparing Equations (4.31) - (4.34) and Equations (4.35) – (4.38), we can define the elementary coefficients $r_{ij}$ and $t_{ij}$ ($i = p, s,$ and $j = +, -$) in analogy to the Fresnel coefficients as

$$r_{s\pm} = \frac{n_\pm k_{xa} - n_{ce} k_{x\pm}}{n_\pm k_{xa} + n_{ce} k_{x\pm}}, \qquad t_{s\pm} = \frac{2n_\pm k_{xa}}{n_\pm k_{xa} + n_{ce} k_{x\pm}}. \tag{4.39}$$

$$r_{p\pm} = \frac{n_\pm n_{ce} k_{xa} - n_a^2 k_{x+}}{n_\pm n_{ce} k_{xa} + n_a^2 k_{x+}}, \quad t_{p\pm} = \frac{2n_\pm n_{ce} k_{xa}}{n_\pm n_{ce} k_{xa} + n_a^2 k_{x+}}. \tag{4.40}$$

With the above expressions, the matrices $\mathbf{T}^{(ac)}$ and $\mathbf{R}^{(ac)}$ in Equations (4.35) and (4.36) can be written as

$$\mathbf{T}^{(ac)} = \begin{bmatrix} j\dfrac{1}{t_{p+}} & -j\dfrac{1}{t_{p-}} \\ \dfrac{1}{t_{s+}} & \dfrac{1}{t_{s-}} \end{bmatrix}, \mathbf{R}^{(ac)} \begin{bmatrix} j\dfrac{r_{p+}}{t_{p+}} & -j\dfrac{r_{p-}}{t_{p-}} \\ \dfrac{r_{s+}}{t_{s+}} & \dfrac{r_{s-}}{t_{s-}} \end{bmatrix}. \tag{4.41}$$

The matrix expressions in Equation (4.41) will be useful for analyzing reflection from a multi-layer structure containing both achiral (dielectric and metal) and chiral materials. We can identify the elementary coefficients $t_{ij}$ in Equation (4.39) and (4.40) as the fraction of light in linear polarization $i$ that is transmitted to circular polarization $j$ at the achiral-chiral interface. The coefficients $r_{ij}$, however, do not readily lend themselves to any simple physical interpretation.

### *4.4.2 Effect of chirality on the reflection spectrum of an achiral-chiral interface*

To investigate the effects of the chiral parameter on the reflection spectrum of a dielectric-chiral interface, we consider the example of a single interface of BK-7 glass as the dielectric material and an aqueous solution of sucrose as the chiral medium (this structure will also be experimentally investigated later). At the 589 nm wavelength (Sodium D-line), sucrose has a specific rotation of $[\alpha]_D^{20} = +66.5$ deg·ml/(g·dm) [103]. Its chiral parameter can be calculated from

$$\chi = \frac{[\alpha]_D^{20}\,\lambda c}{36 n_c}, \tag{4.42}$$

where $\lambda$ is the wavelength and $c$ is the solution volume concentration in *g/ml*. Using the values for the specific rotation $[\alpha]_D^{20} = +66.5$ deg·ml/(g·dm) and the refractive index $n_c$ = 1.4201[104], we obtain $\chi = 4.7\times10^{-7}$ for sucrose at 589 nm wavelength. The refractive index of BK-7 glass around this wavelength is $n_a$ = 1.517.

We consider LP light with field components $\mathbf{E}_i = [E_{i,p}, E_{i,\mathrm{s}}]^{\mathrm{T}}$ incident from the BK-7 glass medium onto the interface at incidence angle $\theta_a$, as illustrated in Figure 4.2. This results in reflected LP light $\mathbf{E}_r = [E_{\mathrm{r},p}, E_{\mathrm{r,s}}]^{\mathrm{T}}$ in the glass medium and transmitted CP light $E_+$ and $E_-$ in the chiral solution at the refraction angles $\theta_+$ and $\theta_-$ respectively. Setting the incident light $\mathbf{E}_2^{(\mathrm{c})}$ in the chiral medium to 0 in Equations (4.35) - (4.36), we solve for the LP reflected light to get

$$\mathbf{E}_r = \mathbf{R}^{(\mathrm{ac})}\left(\mathbf{T}^{(\mathrm{ac})}\right)^{-1}\mathbf{E}_i = \begin{bmatrix} r_{pp} & r_{sp} \\ r_{ps} & r_{ss} \end{bmatrix}\mathbf{E}_i\,. \tag{4.43}$$

The elements $r_{pp}$ and $r_{ss}$ are the reflection coefficients of the $p$ and $s$-polarizations, while $r_{ps} = -r_{sp}$ denote the cross-polarization reflection coefficients. If the chiral parameter $\chi$ is 0 (i.e., the medium on the right is achiral), the reflection matrix reduces to a diagonal matrix ($r_{ps} = -r_{sp} = 0$) with conventional Fresnel reflection coefficients $r_p$ and $r_s$ as given in Equations (4.33) - (4.34).

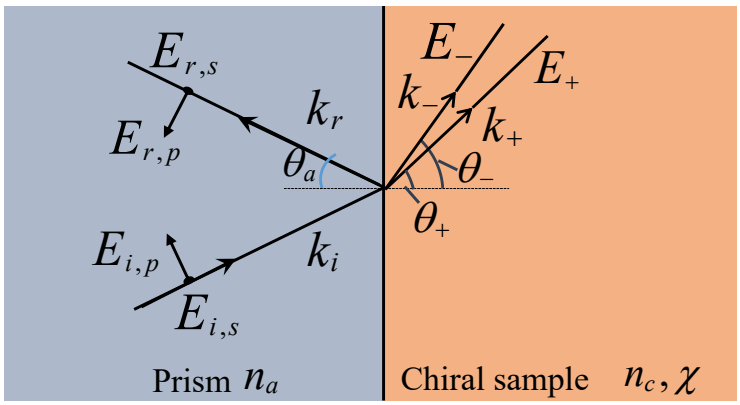


Figure 4.2 Reflection at an achiral-chiral interface

In Figure 4.3(a) and (b), we plot the magnitude and phase of the reflection coefficients at the interface of BK-7 glass and sucrose solution as a function of the incidence angle at the 589nm wavelength. Since $\chi \ll 1$, the magnitudes of the cross-polarization reflection coefficients in Figure 4.3(a) are close to zero except near the critical incidence angle $\theta_c$ (given by $\sin\theta_c = n_c/n_0 \approx \sin\theta_{c-} \approx \sin\theta_{c+}$), where the effect of chirality is strongly enhanced as seen from peak amplitudes of $r_{ps}$ and $r_{sp}$ [105]. Silverman et. al. employed this enhanced chiral effect near the critical angle to measure the differential linear reflectance (DLR) [106] and differential circular reflectance (DCR) [107, 108] of the chiral medium, which are defined as

$$\mathrm{DLR} = \frac{(R_s - R_p)}{(R_s + R_p)} = \frac{(|r_{ss}|^2 + |r_{sp}|^2 - |r_{pp}|^2 - |r_{ps}|^2)}{(|r_{ss}|^2 + |r_{sp}|^2 + |r_{pp}|^2 + |r_{ps}|^2)} \tag{4.44}$$

$$\mathrm{DCR} = \frac{(R_+ - R_-)}{(R_+ + R_-)} = \frac{(|r_{++}|^2 + |r_{+-}|^2 - |r_{--}|^2 - |r_{-+}|^2)}{(|r_{++}|^2 + |r_{+-}|^2 + |r_{--}|^2 + |r_{-+}|^2)}. \tag{4.45}$$

Recently, a cavity ringdown polarimeter (CRDP) was reported in which an optical resonator was used to further enhance the chiral signal near the critical angle by a factor equal to the number of cavity passes [90].

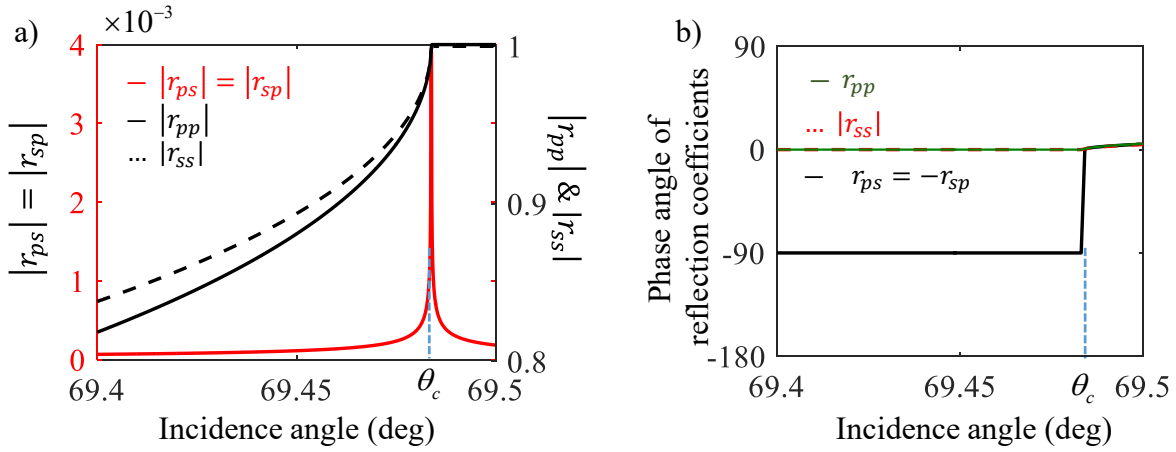


Figure 4.3 Plots of the reflection coefficients as functions of the incidence angle at the interface between BK-7 glass with index $n_a = 1.5167$ and a non-absorbing chiral medium with index $n_c = 1.4201$ and chiral parameter $\chi = 4.7 \times 10^{-7}$ at the 589nm wavelength.

From Figure 4.3(b), we also observe that when the incidence angle is smaller than the critical angle, $r_{ps} = -r_{sp}$ are imaginary numbers while $r_{pp}$ and $r_{ss}$ are real numbers. This leads to a phase difference between the *p*- and *s*-polarization components of the reflected light upon reflection from an achiral-chiral interface. This phase difference is strongly enhanced near the critical angle and depends on the chiral parameter, thus providing an alternative approach for chiral detection by interrogating the change in the phase difference between the *p*- and *s*- polarization components of light reflected from an achiral-chiral interface. Note that for an achiral-achiral interface, the phase change reduces to zero. This method of chiral detection has the advantage of reduced sample volume compared to conventional transmission polarimetry, which typically requires very thick samples (~1cm) to achieve good signal-to-noise ratio. A heterodyne interferometric method based on detecting the phase difference between the two LP components has been developed in [89], which offers good accuracy and does not require large sample volumes. However, the method requires complex and delicate experimental setup, and uses a single-wavelength laser source so that measurement of chiral parameter can only be made at a single wavelength.

## 4.5 A Differential Ellipsometric Method for Broadband Chiral Measurement

In this section we develop a differential ellipsometric method for chirality measurement by exploiting the enhanced cross-polarization phase difference of light reflection from an achiral-chiral interface near the critical angle of incidence. The differential approach suppresses the system noise and enhances the SNR of the measurements, allowing the technique to be implemented with a broadband lamp instead of high-power tunable lasers. This is an important advantage since it allows broadband measurements of chiral samples to be made with a commercial variable angle spectroscopic ellipsometer (VASE). Ellipsometry is a powerful technique for characterizing the change in the polarization state of light upon reflection from a sample surface and is widely used for characterizing optical properties of materials. Commercial ellipsometry systems provide wavelength scanning capability spanning from the UV to IR range, variable incidence angle with increment as small as 0.001˚, as well as good ellipsometric angle resolution [109, 110]. The development of a chiral measurement method that can take advantage of the capabilities of commercial ellipsometers can thus provide a potentially valuable tool for the study and characterization of chiral compounds.

### *4.5.1 Theoretical development*

In conventional ellipsometry, linearly polarized light at wavelength $\lambda$ is shone on a sample surface at incident angle $\theta_0$ and the amplitudes and phases of the reflected *s*- and *p*-polarized light waves are measured. From the measured reflection coefficients, the ellipsometric ratio $\rho$ is calculated from [111]

$$\rho = r_p / r_s = \tan\psi e^{i\Delta}, \tag{4.46}$$

where $\psi$ and $\Delta$ are the ellipsometric amplitude angle and phase angle, respectively. For linearly polarized light reflected from an isotropic achiral sample, the off-diagonal elements of the reflection matrix in Equation (4.43) are zero. However, for a chiral sample, the off-diagonal components of the reflection matrix are no longer zero, so that the ellipsometric ratio $\rho$ also depends on $r_{ps}$ and $r_{sp}$, as we will show below. Thus by measuring the cross-polarization reflection coefficients, we can determine the chiral parameter $\chi$ of the sample.

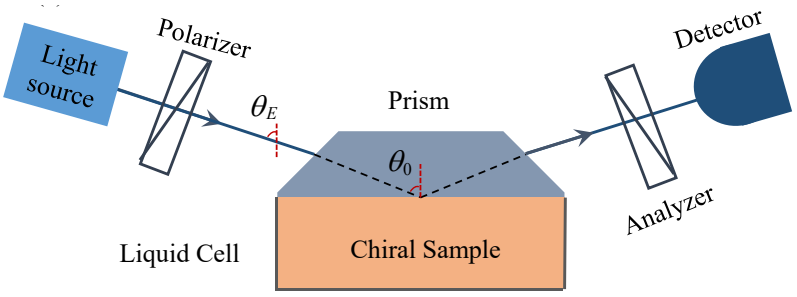


Figure 4.4 Schematic diagram of a standard ellipsometry setup for chirality measurement.

Figure 4.4 shows the setup for an ellipsometry measurement of reflection from an achiral-chiral interface. The achiral medium is a prism of refractive index $n_0$. The chiral medium is characterized by an average refractive index $n_c$ and chiral parameter $\chi$. Light from a light source passes through a polarizer set at angle $P$ relative to the $p$-polarization, so that the transmitted light is a linearly-polarized plane wave described by the Jones vector $[\cos P, \sin P]^{\mathrm{T}}$. The reflected light passes through an analyzer set at angle $A$ relative to the $p$-polarization. Using the reflection matrix at an achiral-chiral interface in Equation (4.43), we can calculate the reflected field amplitude after the analyzer from

$$\begin{aligned} E_r &= \begin{bmatrix}\cos A & \sin A\end{bmatrix}\begin{bmatrix} t_{p0} & 0 \\ 0 & t_{s0}\end{bmatrix}\begin{bmatrix} r_{pp} & r_{sp} \\ r_{ps} & r_{ss}\end{bmatrix}\begin{bmatrix} t_{p0} & 0 \\ 0 & t_{s0}\end{bmatrix}\begin{bmatrix}\cos P \\ \sin P\end{bmatrix} \\ &= t_{p0}^2 r_{pp}\cos P\cos A + t_{p0}t_{s0}r_{sp}\sin P\cos A + t_{p0}t_{s0}r_{ps}\cos P\sin A + t_{s0}^2 r_{ss}\sin P\sin A \\ &= \cos P\cos A\left(t_{p0}^2 r_{pp} + t_{p0}t_{s0}r_{sp}\tan P\right) + \sin P\sin A\left(t_{p0}t_{s0}r_{ps}\cot P + t_{s0}^2 r_{ss}\right) \\ &= \cos P\cos A\left(t_{p0}^2 r_{pp} + t_{p0}t_{s0}r_{ps}\,\mathrm{tanA}\right) + \sin P\sin A\left(t_{p0}t_{s0}r_{sp}\,\mathrm{cotA} + t_{s0}^2 r_{ss}\right) \end{aligned} \tag{4.47}$$

The expressions for the elements of the reflection matrix are given in Equation (4.43). Transmission coefficients $t_{p0}$ and $t_{s0}$ account the transmission at the air-prism interfaces. If the sample is achiral, then $r_{ps} = r_{sp} = 0$ and the reflected field amplitude reduces to

$$E_r = t_{p0}^2 r_p \cos P\cos A + t_{s0}^2 r_s \sin P\sin A\,. \tag{4.48}$$

In conventional ellipsometry, the reflected light intensity $|E_r|^2$ is measured for various values of the polarizer angle $P$ and analyzer angle $A$. From this set of measurement data, the ellipsometric ratio $\rho$ defined in Equation (4.46) can be obtained as a function of wavelength using a data fitting technique[112].

If the sample is chiral, the reflected field amplitude also depends on the cross-polarization reflection coefficients as shown in Equation (4.47). By comparing Equation (4.47) to (4.48), we can define the equivalent ellipsometric ratios $\rho_{\mathrm{P}}$ and $\rho_{\mathrm{A}}$ for the chiral sample as

$$\begin{cases} \rho_{\mathrm{P}} = \left(t_{p0}^2 r_{pp} + t_{p0} t_{s0} r_{sp} \tan P\right) \Big/ \left(t_{s0}^2 r_{ss} + t_{p0} t_{s0} r_{ps} \cot P\right) = \tan\psi_{\mathrm{P}} e^{i\Delta_{\mathrm{P}}} \\ \psi_{\mathrm{P}} = \arctan\left(\left|t_{p0}^2 r_{pp} + t_{p0} t_{s0} r_{sp} \tan P\right| \Big/ \left|t_{s0}^2 r_{ss} + t_{p0} t_{s0} r_{ps} \cot P\right|\right) \\ \Delta_{\mathrm{P}} = Arg\left(t_{p0}^2 r_{pp} + t_{p0} t_{s0} r_{sp} \tan P\right) - Arg\left(t_{s0}^2 r_{ss} + t_{p0} t_{s0} r_{ps} \cot P\right) \end{cases} \tag{4.49}$$

$$\begin{cases} \rho_{\mathrm{A}} = \left(t_{p0}^2 r_{pp} + t_{p0} t_{s0} r_{ps} \tan A\right) \Big/ \left(t_{s0}^2 r_{ss} + t_{p0} t_{s0} r_{sp} \cot A\right) = \tan\psi_{\mathrm{A}} e^{i\Delta_{\mathrm{A}}} \\ \psi_{\mathrm{A}} = \arctan\left(\left|t_{p0}^2 r_{pp} + t_{p0} t_{s0} r_{ps} \tan A\right| \Big/ \left|t_{s0}^2 r_{ss} + t_{p0} t_{s0} r_{sp} \cot A\right|\right) \\ \Delta_{\mathrm{A}} = Arg\left(t_{p0}^2 r_{pp} + t_{p0} t_{s0} r_{ps} \tan A\right) - Arg\left(t_{s0}^2 r_{ss} + t_{p0} t_{s0} r_{sp} \cot A\right) \end{cases} \tag{4.50}$$

Note that $\rho_{\mathrm{P}}$ depends on the polarization angle $P$ but not the analyzer angle $A$, while the converse is true for $\rho_{\mathrm{A}}$. However, both ellipsometric angles (or more specifically the amplitude angle $\psi$ and phase angle $\Delta$) carry information about the cross-polarization reflection coefficients. For our work, we will use measurements of the phase angle $\Delta_{\mathrm{A}}$ to extract the chiral parameter of the sample.

Since chirality introduces only small perturbations to the ellipsometric measurements, it is very difficult to accurately extract the chiral parameter from the absolute ellipsometric phase angle values, which would require accurate prior knowledge of the refractive indices, incidence angles and the system baseline. A common solution which is widely employed in CD spectroscopy is to subtract the measurement data with the reference data of a known achiral sample. The reference sample should ideally have the same refractive index as the chiral sample and be measured under identical condition, both of which can introduce systematic errors to the chiral parameter measurements.

We propose a differential approach in which ellipsometry measurements are performed at two different analyzer angles $A_1$ and $A_2$, and the phase angle difference, $\delta\Delta = \Delta_{\mathrm{A2}} - \Delta_{\mathrm{A1}}$, of the two ellipsometric ratios is used to determine the chiral parameter $\chi$ of the sample. If the sample is an achiral medium, the ellipsometric ratio reduces to Equation (4.46), so that $\delta\Delta = 0$. The differential approach allows the rejection of common noise sources from the multiple optical components in the ellipsometry system, thereby significantly improving the measurement SNR. The method does not require a reference sample, which also helps reduce systematic error.

| | | OR | CD |
|---|---|---|---|
| **Wavelength** | | 589nm | 400nm |
| **Refractive Index** | BK-7 Glass | 1.517 | 1.530 |
| | Chiral medium | 1.420 | $1.506 - 1.22\times10^{-3}$j |
| **Chiral parameter χ** | | $4.7\times10^{-7}$ | $5.08\times10^{-7}$j |

Table 4.1 Optical parameters used in the simulations of the differential ellipsometry method for measurements of OR and CD chirality.

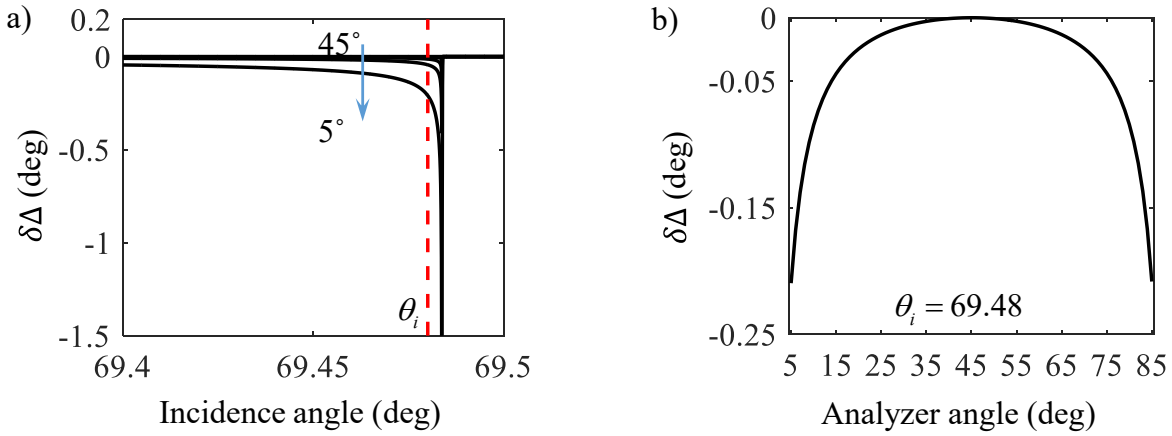


Figure 4.5 (a) Simulated phase angle difference δΔ vs. the incidence angle for a transparent chiral sample with OR chirality at 589nm wavelength, for various values of the analyzer angle $A$.

(b) Phase angle difference δΔ vs. analyzer angle $A$ in the range of 5˚~85˚, at a fixed incidence angle of 69.48˚ (indicated by the red dashed line in (a)).

### *4.5.2 Simulation results*

To demonstrate the differential ellipsometric method and evaluate its performance for chirality measurement, we performed numerical simulations of the ellipsometry system in Figure 4.4 using a BK-7 glass prism and a transparent chiral sample with real chiral parameter $\chi$, i.e., a material with optical rotation property. The optical constants of the materials used in the simulations are summarized in Table 4.1 under the OR column. In the simulations, we fixed the reference analyzer angle $A_1 = A_{REF} = 45^\circ$ while the angle $A_2 = A$ is varied from 5˚ to 45˚ with 10˚ increments. Figure 4.5(a) plots the phase angle difference δΔ as a function of the incidence angle for different settings of the analyzer angle $A$. We observe that the phase angle difference increases in magnitude abruptly

near the critical angle of incidence $\theta_c$. In Figure 4.5(b) we plot the phase angle difference $\delta\Delta$ vs. the analyzer angle $A$ for a fixed incidence angle $\theta_i = 69.48°$, which is near the critical angle. We observe that $\delta\Delta$ becomes larger in magnitude as the analyzer angle approaches 0° and 90°. Thus, for maximum SNR, it is better to perform ellipsometric measurements of the chiral sample with the analyzer angle $A$ set close to 0° or 90°. We also observe in Figure 4.5(b) that for the weak chiral parameter assumed in the simulations ($\chi = 4.7\times10^{-7}$), the magnitude of $\delta\Delta$ is in the range 0 – 0.25° for analyzer angles close to 5° and 85°. This range of phase angles can readily be measured by commercial ellipsometry systems, which typically can resolve the ellipsometric phase angle $\Delta$ with a resolution as small as 0.005˚.

We also performed simulations for the case where the chiral sample is absorbing with a complex refractive index and an imaginary chiral parameter $\chi$, i.e., the medium exhibits circular dichroism. The optical parameters used in the simulations are listed in Table 4.1 under the CD column. Figure 4.6(a) shows the plot of $\delta\Delta$ vs. the incidence angle for analyzer angle settings from 5˚ to 45˚. We observe that the phase angle difference also exhibits enhanced response near the critical angle of incidence. However, the response is more broadened around the critical angle than that of the OR chiral medium in Figure 4.5(a), which is attributed to material absorption. Figure 4.6(b) shows the variation of $\delta\Delta$ with the analyzer angle $A$ at the critical angle of incidence. Again, the phase angle difference increases as the analyzer angle approaches 0˚ and 90˚, although its magnitude is much smaller than those obtained for the OR chiral medium in Figure 4.5(b). The small phase angle difference makes it more difficult to measure the chiral parameter of a CD medium with this technique. In Chapter 5, we will propose a method based on surface plasmon resonance which can potentially provide stronger enhancement of the phase angle difference for measurement of CD chirality.

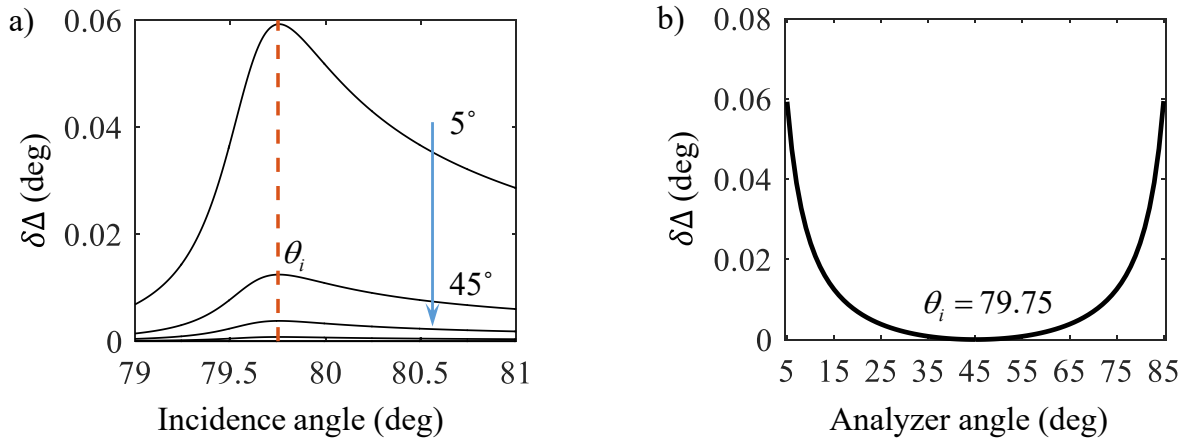


Figure 4.6 (a) Simulated phase angle difference δΔ vs. the incidence angle for an absorbing chiral medium with CD chirality at 400nm wavelength, for various values of the analyzer angle $A$. (b) Phase angle difference δΔ vs. analyzer angle in the range of 5°~85°, at incidence angle of 79.75° (indicated by the red dashed line in (a)).

We also examined the variation of the ellipsometric phase angle difference with the chiral parameter at the critical angle of incidence. The results are shown in Figure 4.7(a) and (b) for OR chiral medium and CD chiral medium, respectively. In both plots the reference analyzer angle $A_{\mathrm{REF}}$ is set at 45° and the other angle is set at $A$ = 5°. It can be seen that for both types of chirality, the phase angle difference varies linearly with the magnitude of the chiral parameter, $\delta\Delta \propto |\chi|$. For OR medium, the angle δΔ is negative if $\mathrm{Re}\{\chi\}$ is positive and vice versa. The linear relationship in Figure 4.7(a) can thus be used to determine both the strength of the real part of the chiral parameter as well as the handedness of the enantiomer. For a chiral solution, the chiral strength depends on the concentration of the chiral solute. Thus, if the chiral parameter of an enantiomer is known, we can use the technique to determine the concentration of the chiral molecules in an enantio-pure solution, or to characterize the enantiomeric excess (also referred to as the optical purity) of a chiral sample composed of a mixture of mirrored enantiomers. Both of these measurements are of important interest in drug development and manufacturing [113].

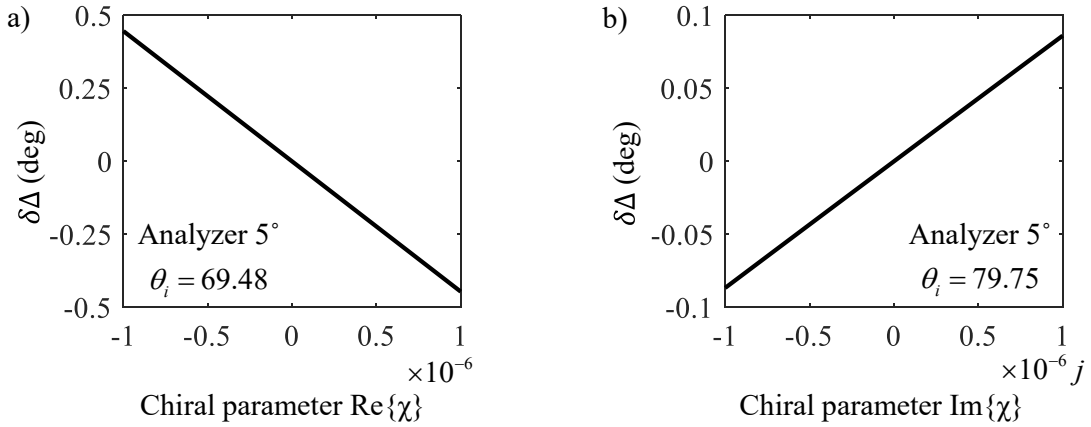


Figure 4.7 Simulated phase angle difference δΔ vs. the chiral parameter χ for (a) sample with OR chirality and (b) sample with CD chirality. The analyzer angle is set at $A = 5^{\circ}$. The incidence angles for the OR and CD samples are 69.48˚ and 79.75˚ respectively.

Finally we note that modern ellipsometry systems employ more advanced optics configuration than shown in Figure 4.4 to improve the SNR, resolution and sensitivity [110, 114, 115], as well as to allow more advanced measurements such as those based on the Muller Matrix [109, 110]. Examples of advanced ellipsometry systems include the Polarizer-Sample-Rotating Analyzer (PSRA) system [110], the Polarizer-Compensator-Sample-Analyzer (PCSA) system [109] and the Polarizer-Sample-Compensator-Analyzer (PSCA) system [116]. Equation (4.49) and (4.50) holds for these advanced systems under standard ellipsometry operation mode, while the choice of $\rho_{\mathrm{P}}$ or $\rho_{\mathrm{A}}$ depends on the type of optics configuration employed in the system. Detailed derivations of $\rho_{\mathrm{P}}$ or $\rho_{\mathrm{A}}$ for these system can be found in [6, 110, 116].

## 4.6 Optical Rotation Measurement Using the Differential Ellipsometric Method

*Materials and experimental setup*

In the experiment, we chose sucrose aqueous solution as the chiral sample to be measured, since its physical and optical properties are well documented [104, 117], including density, molar concentration, and refractive index as functions of the solution mass concentration. Reference data of the chiral parameter can be obtained from the specific rotation at 589nm wavelength provided in the specification data sheet of sucrose [103] and the optical rotatory dispersion data reported in [118]. Sucrose solution is also commonly used as a calibration standard for polarimeters.

We added sucrose (Sigma Aldrich) to DI-water with a 1:1 weight ratio to obtain a 50% wt% solution. The mixture is stirred by a magnetic stir bar for 24 hours at room temperature to form a uniform solution. The solution obtained is transparent with a faint yellow colour, resulting from a weak absorption near 270nm [103]. We confirmed this by measuring the absorption spectrum of the solution over the wavelength range 200 – 450nm, as shown in Figure 4.8, using a Hitachi UH-3000 UV-Vis Spectrophotometer and DI-water as the reference sample. The chirality of sucrose solution is commonly reported by the specific rotation $[\alpha]_D^{20}$, which is related to the chiral parameter by Equation (4.42). Using the reference values of $[\alpha]_D^{20} = +66.5°$ [103] and $n_c = 1.4201$ [18], we calculated $\chi = 4.7\times10^{-7}$ for the 50% wt% sucrose solution at 589nm wavelength.

A dove prism (BK7, Thorlabs Inc., $n_0$ = 1.517 at 589nm) is employed as the dielectric (achiral) medium with a higher refractive index than the chiral solution sample. The Polypropylene cap (O.D.×Height: 28mm×10mm) of a Wheaton glass scintillation Vial (Fisher Scientific Inc.) is used as the container for the liquid. The liquid surface is in direct contact with the prism to establish the achiral-sample interface. For the control experiment, we used DI water as the achiral sample.

We employed the M-2000v Spectroscopic Ellipsometer with a Quartz Tungsten Halogen lamp light source and WVASE32 software from J. A. Woollam Inc. to perform ellipsometry measurements of the sample over the wavelength range of 500-1000nm. Figure 4.9 shows a photograph image of the setup. The ellipsometer is first calibrated using a standard wafer provided

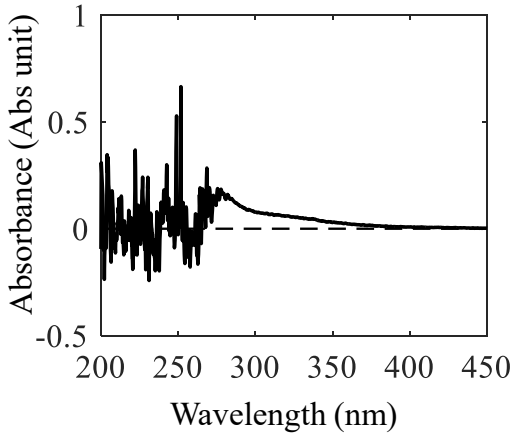


Figure 4.8 Absorption spectrum of a 50% wt% sucrose solution.

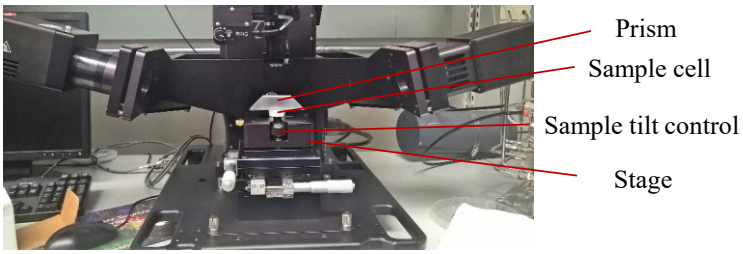


Figure 4.9 A photograph image of the ellipsometry setup for chiral measurement.

by J.A. Woollam Inc. (250nm $SiO_2$ on Si wafer) using the calibration procedure as described in the manual [110]. After mounting the sample on the stage, an alignment procedure is performed to ensure that the prism-sample surface is perpendicular to the plane of incidence, and that the reflected beam enters the center of the detector unit for maximum intensity. As depicted in Figure 4.4(a), the input angle $\theta_E$ of the ellipsometer is calculated from the incidence angle $\theta_0$ at the prism-sample interface using the relation $\theta_E = 45° + \arcsin\left((\theta_0 - 45)n_0\right)$, where 45° is the inclination angle of the dove prism. We used an input angle $\theta_E$ sweeping range of ~2° with increments of 0.2°. For each angle setting, the alignment procedure is first performed to obtain fine adjustments to the sample stage tilt and height. Ellipsometry measurements are then performed at a reference analyzer angle of $A_{REF}$ = 45° and angle $A$ = 5°. The incidence angle is swept at a step size of 0.005°.

*Experimental results*

We first report the measurement results for the DI water control sample at 589nm wavelength. Figure 4.10(a) plots the phase angle difference δΔ and the ellipsometric amplitude angle $\psi$ versus the incidence angle. It can be seen that δΔ remains close to zero for all incidence angles since the water sample is achiral. The critical incidence angle $\theta_c$ can be estimated by examining the amplitude angle $\psi$, which becomes constant for $\theta_0 > \theta_c$ due to total internal reflection of both *s* and *p* polarizations.

Figure 4.10(b) shows the measurement results for the sucrose solution at 589nm. Also shown by the black line is the theoretical response of the phase angle difference, which is calculated using Equation (4.41). We observe that |δΔ| increases rapidly as the incidence angle $\theta_0$ approaches $\theta_c$, then returns to zero when $\theta_0 > \theta_c$. This behaviour is qualitatively in agreement with the theoretical curve, although the measured response is more broadened. One possible contributing factor is the absorption in the prism and the sucrose solution, which result in

broadening of the sharp phase transition at critical angle, similar to the case of a lossy chiral sample shown in Figure 4.6. To determine the chiral parameter, we computed the curve of δΔ vs. χ at the critical angle of incidence $\theta_c$ (similar to Figure 4.7(a)) and used the measured maximum value of |δΔ| to obtain the corresponding value for the chiral parameter to within a tolerance of 0.005˚. In this way we obtained a chiral value of $\chi = 4.4\times10^{-7}$ for the 50% sucrose solution sample at 589nm, which is in close agreement with the value of $\chi = 4.7\times10^{-7}$ calculated from reference data.

Figure 4.11(a) shows the measured data for the phase angle difference of the sucrose solution vs. the incidence angle at various wavelengths. We observe that the maximum value of |δΔ| at the critical incidence angle decreases at longer wavelengths. We computed the chiral parameter for each wavelength and plotted the data in terms of the specific rotation (using Equation (4.34)) vs. wavelength in Figure 4.11(b). Also shown are the reference ORD (optical rotation dispersion) data for the sucrose solution, which is given by the formula $[\alpha]_\lambda = A/(\lambda^2 - \lambda_0^2)$ with parameters $A = 2.17\times10^7$ deg·mL·g$^{-1}$·dm$^{-1}$·nm$^2$ and $\lambda_0 = 131$nm [118, 119]. It can be seen that the measured specific rotation values are in good agreement with the reference ORD curve over the measured wavelength range.

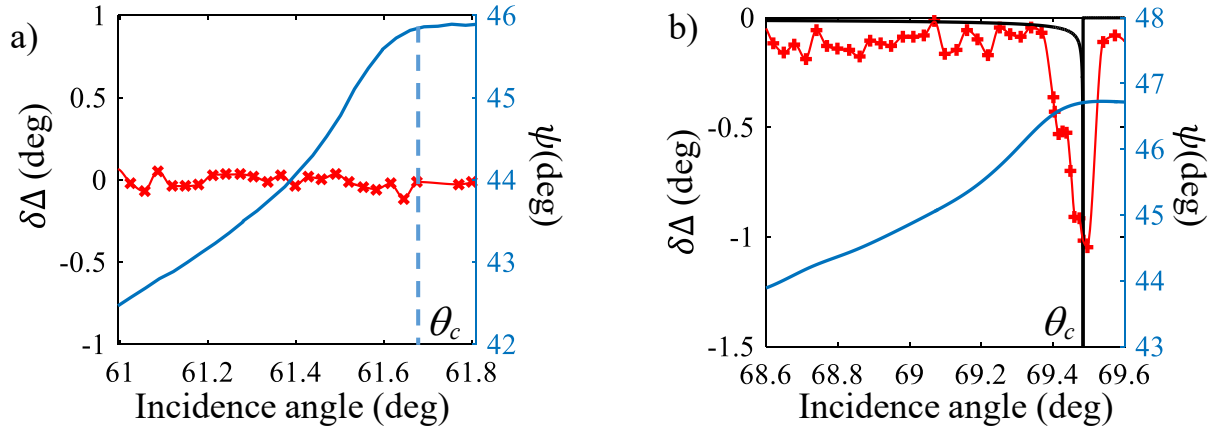


Figure 4.10 Plots of the measured (red line) and theoretical (black line) phase angle difference δΔ vs. the incidence angle for (a) DI water and (b) sucrose solution (50% wt%) at 589nm wavelength. The blue curves show the ellipsometric amplitude angle $\psi$ vs. the incidence angle with the analyzer angle set at 45˚.

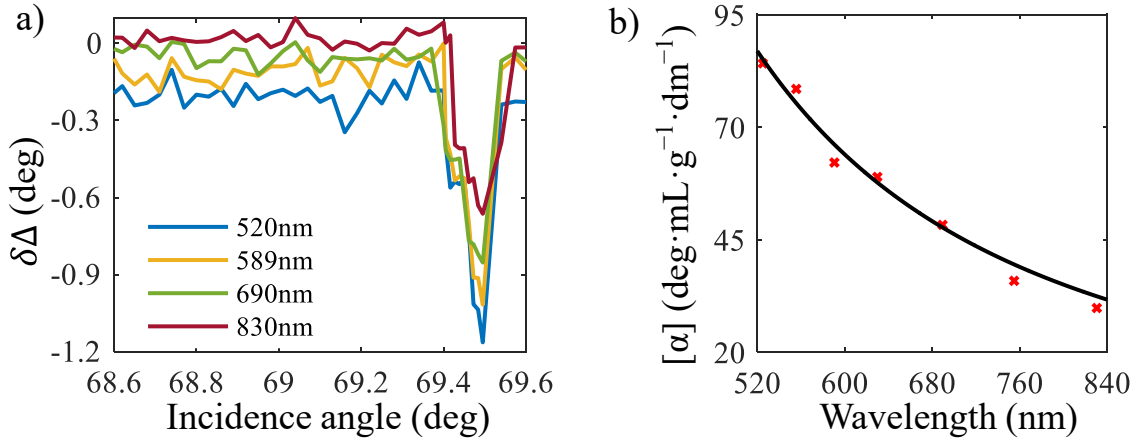


Figure 4.11 (a) Plots of the phase angle difference vs. the incidence angle for the 50% wt.% sucrose solution at various wavelengths. (b) Measured specific rotation (red crosses) and reference ORD data (black curve) of the sucrose sample at various wavelengths.

Finally we note that from the measured spectrum of $\mathrm{Re}\{\chi\}$ (the OR spectrum), it is possible to obtain the spectrum of $\mathrm{Im}\{\chi\}$ (the CD spectrum) of the sample using the KK relations [99]

$$\mathrm{Re}\{\chi(\omega)\} = \frac{2\omega}{\pi} P\int_0^\infty \frac{\mathrm{Im}\{\chi(\nu)\}}{\nu^2-\omega^2} d\nu \tag{4.51}$$

$$\mathrm{Im}\{\chi(\omega)\} = -\frac{2}{\pi} P\int_0^\infty \frac{\nu\,\mathrm{Re}\{\chi(\nu)\}}{\nu^2-\omega^2} d\nu \tag{4.52}$$

where $P$ is the principle value of the integrals and $\omega$ is the angular frequency. Note that the above integrals extend over the entire spectral range from DC to infinity, whereas measurement data for the OR spectrum are limited to a finite wavelength range. One approach to overcome this difficulty is to fit the OR data with a model such as a modified Gaussian and Lorentzian curve and use this function to evaluate the indefinite integral in the KK transform to obtain the CD spectrum.

### 4.7 Summary

In this chapter we developed a differential ellipsometric method for measuring the OR spectrum of transparent chiral materials. The method exploits the enhanced chiral effect on the reflection spectrum of an achiral-chiral interface near the critical incidence angle. By using a differential approach to extract the chiral parameter from ellipsometry measurement data, we showed that the

system noise could be sufficiently suppressed so that the method is sensitive enough to detect the weak chirality of naturally-occurring substances using a standard ellipsometry setup. We implemented the method in a commercial ellipsometer and demonstrated its application for measuring the OR spectrum of a sucrose solution, with the results found to be in good agreement with reference data.

We also theoretically investigated the performance of the method for measuring the CD spectra of lossy chiral samples and found that the chiral effect is too weak to be detected in a standard ellipsometry system. In the next chapter, we will explore the possibility of using surface plasmon resonance to enhance the OR and CD chiral signatures at a metal-chiral surface, which can potentially provide an alternative, more sensitive method for chiral measurement.

# Chapter Five.

## Chiral Sensing Based on Surface Plasmon Resonance

In Chapter 4, we developed a differential ellipsometric method for chiral measurement based on reflection from an achiral-chiral interface near the critical incidence angle. The method was shown to be a robust technique for measuring the OR spectrum of a transparent chiral sample, but suffers from the issue of weak SNR when used to measure the CD spectrum of a lossy chiral material. In recent years, surface plasmon resonance (SPR) has been employed to develop highly-sensitive refractometric sensors for both transparent [120] and absorbing samples [9]. The SPR phenomenon is also widely exploited to enhance the sensitivity of other sensing technologies that interrogate the absorption and scattering of light in matter, such as fluorescence spectroscopy [121], optical absorption spectroscopy [122], and Raman spectroscopy [123]. Recently, localized surface plasmon polaritons have also been exploited to enhance and detect the CD signatures of chiral molecules assembled on metal nano-particles [91, 92, 124].

The objective of this chapter is to investigate the behaviour of light propagating or reflecting at a metal-chiral interface and exploit phenomena that are sensitive to chirality for measurement of OR and CD. We will first investigate the propagation of surface waves at a metal-chiral interface and show that chiral surface plasmon polaritons (SPPs) have unique characteristics different from those of conventional SPPs at a dielectric-metal interface. In particular, chiral SPPs have a cut-off condition which strongly depends on the strength of the chirality, which can potentially be exploited for chiral sensing. We also investigate the excitation of chiral SPPs by light incident on a metal-chiral interface, considering both commonly-used configurations for SPP excitation, namely, the Kretschmann and Otto configurations. Through simulation studies, we will show that

the reflection spectra of both SPR systems exhibit enhanced chiral signatures which can be exploited for ellipsometric measurement of OR and CD chiralities. In particular, the ellipsometric response of the Otto configuration is found to be more sensitive to the chiral strength of the sample than that of the Kretschmann system. We also investigate the feasibility of implementing the SPR-enhanced ellipsometric method based on the Otto configuration in a commercial ellipsometer.

This chapter is organized as follows. We will first investigate the propagation characteristics of chiral SPPs at a metal-chiral interface in Section 5.1. In Section 5.2 we will derive a general reflection matrix for light incident on a multi-layer system with an embedded chiral material. The reflection matrix will be applied to the two common configurations for exciting SPPs, namely, the Kretschmann SPR system and the Otto SPR system. In Section 5.3, we will present simulation results to investigate the performance of SPR-enhanced ellipsometric methods for measuring OR and CD chiralities based on the two SPR systems. In Section5.4, we will present preliminary experimental results of our attempt to implement the ellipsometric method based on the Otto configuration in a commercial spectroscopic ellipsometer. The chapter is summarized in Section 5.5.

## 5.1 Chiral Surface Plasmon Polaritons

SPPs are electromagnetic surface waves propagating along the interface of a dielectric and a metal as a result of the coupling between the electromagnetic fields and the electron plasma oscillations in the metal. Only TM waves (defined as having an electric field component perpendicular to the interface) can excite SPPs, which are evanescently bound to both sides of the interface. When chirality is introduced into the dielectric material, the surface plasmon wave exhibits unique properties that distinguish them from conventional SPPs. In this section we derive the dispersion relation of chiral SPPs supported by a chiral-metal interface and investigate the propagation characteristics of chiral SP waves.

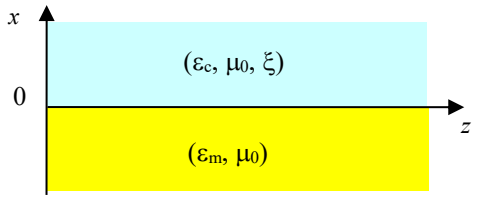


Figure 5.1. Interface between a metal and a chiral medium

Figure 5.1 shows a planar interface between a metal with complex dielectric constant $\varepsilon_m$ and a chiral medium with dielectric constant $\varepsilon_c$ and chiral admittance $\xi$. Both media have vacuum magnetic permeability $\mu_0$. We assume a plane wave propagating along the positive *z* axis with the *z* dependence $e^{-j\beta z}$, and denote the direction normal to the interface as the *x* axis. For this 1-D structure, the wave equations for the electric and magnetic fields in the chiral medium, which are given by Equation (4.6), reduce to

$$\frac{\partial^2}{\partial x^2}\begin{pmatrix} E_i \\ H_i \end{pmatrix} + ((1+2\chi^2)n_c^2 k_0^2 - \beta^2)\begin{pmatrix} E_i \\ H_i \end{pmatrix} + \begin{pmatrix} -2j\xi k_0^2 / \eta_0^2 H_i \\ 2j\xi(1+\chi^2)n_c^2 k_0^2 E_i \end{pmatrix} = 0\,, \tag{5.1}$$

with $i = x, y, z$. The general solutions for the longitudinal field components ($E_z$, $H_z$) can be expressed using Equations (4.7) and (4.8) as

$$E_z = C_1 e^{-k_{x1}x} + C_2 e^{-k_{x2}x},\ H_z = j\eta_c\sqrt{1+\chi^2}\,(C_1 e^{-k_{x1}x} - C_2 e^{-k_{x2}x})\,. \tag{5.2}$$

From the above solutions for ($E_z$, $H_z$), we can obtain the transverse field components ($E_x$, $H_x$, $E_y$, $H_y$) in the chiral medium as [125]:

$$E_x = -(j\beta / k_{x1})C_1 e^{-k_{x1}x} - (j\beta / k_{x2})C_2 e^{-k_{x2}x}, \tag{5.3}$$

$$H_x = \eta_c\sqrt{1+\chi^2}\left(\frac{\beta}{k_{x1}}C_1 e^{-k_{x1}x} - \frac{\beta}{k_{x2}}C_2 e^{-k_{x2}x}\right), \tag{5.4}$$

$$E_y = -(k_+ / k_{x1})C_1 e^{-k_{x1}x} + (k_- / k_{x2})C_2 e^{-k_{x2}x}, \tag{5.5}$$

$$H_y = -j\eta_c\sqrt{1+\chi^2}\left(\frac{k_+}{k_{x1}}C_1 e^{-k_{x1}x} + \frac{k_-}{k_{x2}}C_2 e^{-k_{x2}x}\right). \tag{5.6}$$

In the metal, the fields are given by

$$E_z = A_1 e^{k_{xm}x}, \qquad H_z = B_1 e^{k_{xm}x}, \tag{5.7}$$

$$E_x = (j\beta / k_{xm})E_z, \qquad H_x = (j\beta / k_{xm})H_z\,, \tag{5.8}$$

$$E_y = (-j\omega\mu_0 / k_{xm})H_z,\ \ H_y = (-j\omega\varepsilon_m / k_{xm})E_z\ \ , \tag{5.9}$$

where $k_{xm} = \sqrt{\beta^2 - \omega^2 \mu_0 \varepsilon_m}$ is the transverse decay constant of the SP mode in the metal. By requiring the tangential field components to be continuous at the interface $x = 0$, we obtain the following dispersion relation for the chiral SP mode,

$$\begin{aligned} &\left(\omega\mu_0\eta_c\sqrt{1+\chi^2}k_{x1} + k_+ k_{xm}\right)\left(\frac{\omega\varepsilon_m}{\eta_c\sqrt{1+\chi^2}}k_{x2} + k_- k_{xm}\right) \\ &+\left(\omega\mu_0\eta_c\sqrt{1+\chi^2}k_{x2} + k_- k_{xm}\right)\left(\frac{\omega\varepsilon_m}{\eta_c\sqrt{1+\chi^2}}k_{x1} + k_+ k_{xm}\right) = 0 \end{aligned} \quad . \tag{5.10}$$

Equation (5.5) degenerates to that of SPPs at a normal dielectric-metal interface when the chiral parameter $\chi$ vanishes (in which case the $E_x$ field also vanishes). We also note that chiral SPPs are hybrid in nature, since they support both TE ($E_y$) and TM ($E_x$) components, in contrast to normal SPPs which support only the TM polarization. In general, chiral SPPs are elliptically polarized, with the direction of polarization rotation depending on the sign of the chiral admittance $\xi$.

We numerically solved Equation (5.10) for the propagation constant $\beta$ of SPPs at the interface between gold and a chiral medium with refractive index $n_c = 1.5$ and chiral admittance $\xi$. The permittivity of gold is assumed to be given by the Drude model, with plasma frequency $\omega_p = 1.30\times10^{16}$rad/s and damping constant $\gamma = 2.80\times10^{13}$rad/s [126]. Figure 5.2(a) compares the dispersion curves of chiral SPP with $\xi = 10^{-5}\Omega^{-1}$ (solid black curve) and conventional SPP (green dashed curve) at the interface of Au and a dielectric with index $n_c$ ($\xi = 0$). The dispersion curve of the chiral SPP is seen to follow closely that of the conventional SPP, with both curves asymptotically approaching the surface plasmon resonance frequency $\omega_{sp} = \omega_p / \sqrt{1+n_c^2}$ at large values of $\beta$. The difference between the two dispersion curves becomes more pronounced at low frequencies, as illustrated by Figure 5.2(b), which shows the frequency dependence of the real part of the effective index, $n_{eff} = \mathrm{Re}\{\beta/k_0\}$, for various chiral admittance values. It is seen that as the frequency decreases, the effective index of the chiral SPP begins to deviate from that of conventional SPP (green dashed line) and approaches the value $n_+$ shown by the black dashed line. We also observe that a larger value of the chiral admittance causes the dispersion curve to deviate more from that of conventional SPP.

Due to loss in the metal layer, SPPs decay as they propagate along the metal surface, with the propagation (or decay) length defined as $L_p = 1/2\,\mathrm{Im}\{\beta\}$, which is the distance where the SPP power decays to $1/e$ of the initial value. Figure 5.2(c) shows a plot of the propagation length of

chiral SPP versus frequency for various values of the chiral admittance. We observe that the $L_p$ dispersion curves follow that of conventional SPP (green dashed line) fairly closely except at low frequencies, where the propagation length increases rapidly and the curves begin to level off at different frequency limits for different chiral admittance values. These low-frequency limits signify a cut-off condition of the chiral SPP modes, where the SPP field is no longer bounded to the metal and thus experiences no loss ($\mathrm{Im}\{\beta\} = 0$, $L_p \to \infty$). The existence of a cut-off frequency is unique to chiral SPPs and is not observed for normal SPPs at a dielectric-metal interface.

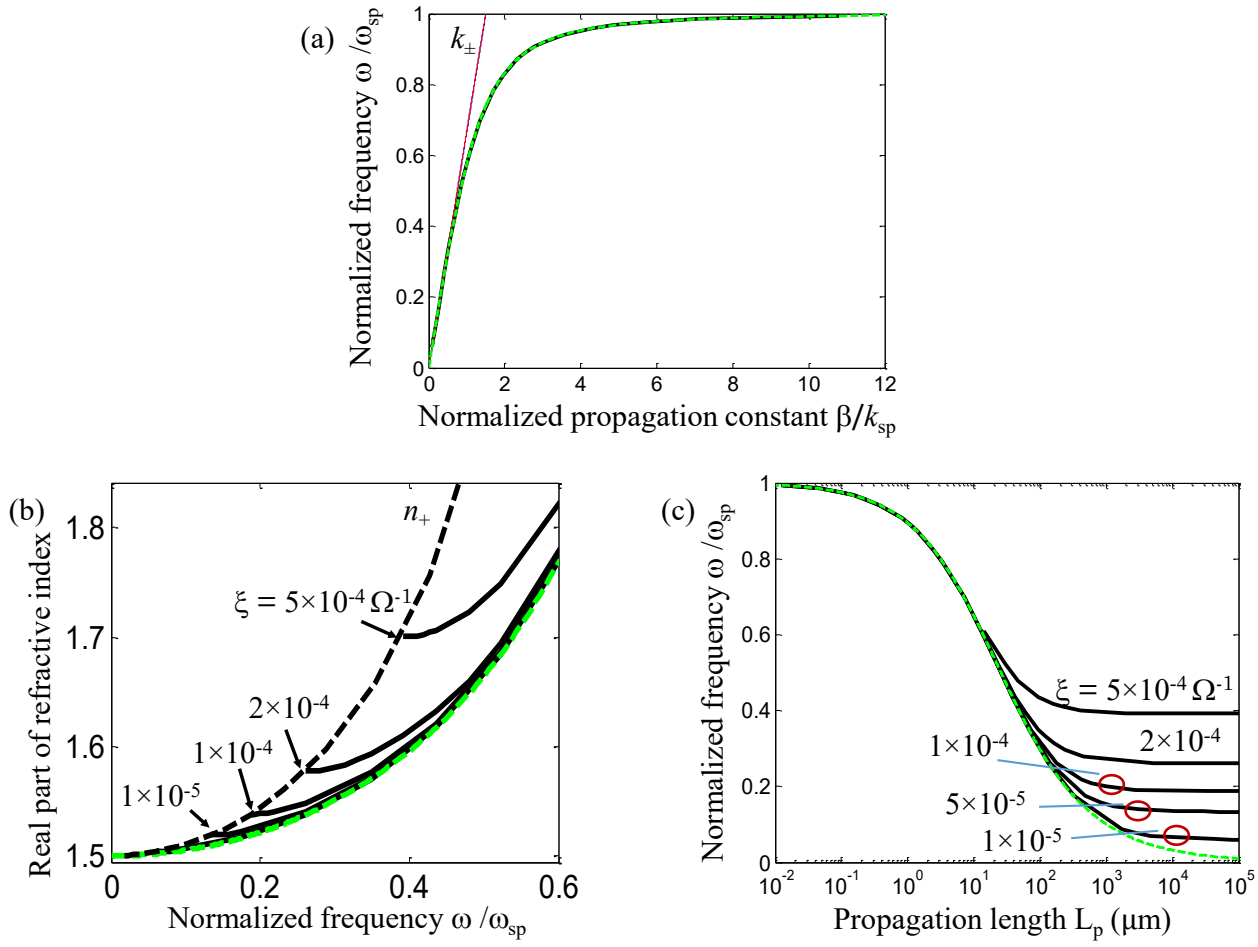


Figure 5.2. a) Dispersion relation of chiral SPP (solid black curve) at the interface of Au and a chiral medium with $\xi = 10^{-5}\Omega^{-1}$. The frequency and propagation constant are normalized by the SP resonance frequency $\omega_{sp}$ and $k_{sp}$ = $\omega_{sp}/c$, respectively. The red lines plot the light lines for $k_\pm$. b) Frequency dependence of the real part of the effective index and c) of the propagation length of chiral SPPs for various values of the chiral admittance. Green dashed lines in all the plots are results for normal SPPs at a Au-dielectric interface.

Figure 5.2(b) shows that at the cut-off frequency, the effective index of the chiral SPP approaches the index value $n_+$ (for our example, which assumes $n_+ > n_-$ or $\xi > 0$). Thus the cut-off condition $\mathrm{Im}\{\beta\} = 0$ may be replaced by the condition $\beta = k_+$, which results in $k_{x1} = 0$ and $k_{x2} = (k_+^2 - k_-^2)^{1/2}$ for the transverse decay constants in the chiral medium. Substituting these values into the dispersion relation in Equation (5.5), we obtain the equation for the cut-off condition

$$\varepsilon_m^2 + 2\varepsilon_c\varepsilon_m(1+2\chi^2)\sqrt{1+1/\chi^2} + \varepsilon_c^2\left[(1+\chi^2)^2 - \sqrt{1+1/\chi^2}\right] = 0\,. \qquad (5.11)$$

For a chiral medium with parameters $\varepsilon_c$ and $\chi$, the above equation can be used to solve for the metal permittivity value $\varepsilon_m$, from which the cut-off frequency can be determined using the Drude model for the metal. More interestingly, the above equation also predicts that at a given frequency ($\varepsilon_m$ value), there exists a cut-off value for the chiral parameter $\chi$ above which the chiral SPP is no longer supported.

In Figure 5.3, we plot the propagation loss ($\exp(-\mathrm{Im}\{\beta\}\times 10^{-3})$) of chiral SPP as a function of the chiral admittance $\xi$ at different wavelengths of light. It is seen that the propagation loss of chiral SPP is always smaller than that of conventional SPPs (with $\xi = 0$) and exhibits a steep drop-off near the cut-off value $\xi_c$, which can be computed using Equation (5.6). The strong dependence of the propagation loss of chiral SPP on the parameter $\xi$ near cut-off can be exploited for chiral sensing application. For example, by measuring the transmission loss of chiral SPP along a chiral-metal interface, we can determine the chirality value. This method has the advantage that it can be implemented on an integrated optics platform, where the metal film can be patterned into a plasmonic waveguide structure and coated with the chiral medium to be measured. For maximum sensitivity, the chiral plasmonic waveguide should be operated near the cut-off frequency. In a different application, the much longer decay length of chiral SPPs compared to conventional SP modes suggests that chirality can provide a potential route toward mitigating loss in plasmonic devices.

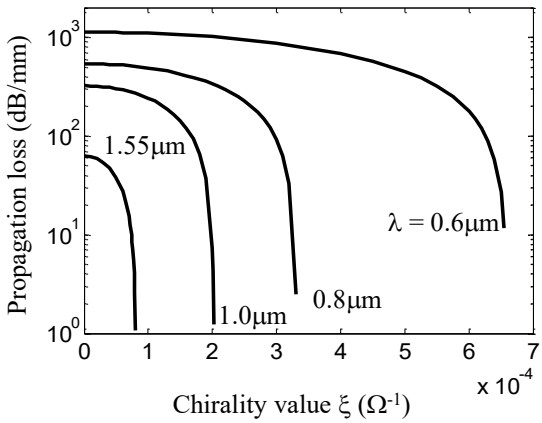


Figure 5.3. Propagation loss of Au-chiral SPPs as functions of the chiral admittance $\xi$ at various wavelengths.

To further shed light on the physical origin of the cut-off condition of chiral SPPs, we examined the field distributions of the chiral SP mode near cut-off. Figure 5.4(a)-(d) plot the amplitude distributions of the $E_z$, $E_x$ and $E_y$ fields of chiral SP modes at the interface between gold and a chiral medium at $\lambda$ = 600nm. The index of the chiral medium is $n_c$ = 1.5 and two chirality values are considered: $\xi = 1\times10^{-4}\ \Omega^{-1}$ and $\xi = 6.68\times10^{-4}\ \Omega^{-1}$, the latter being close to the cut-off value $\xi_c$ at this wavelength. The presence of both $E_x$ and $E_y$ fields (Figure 5.4(c), (d)) indicates that the mode is a hybrid combination of both TM ($E_x$) and TE ($E_y$) components. For small values of $\xi$, the mode is SPP-like with a dominant TM component, as seen in Figure 5.4(c). As $\xi$ approaches the cut off value $\xi_c$, the amplitude of $E_y$ grows indicating that more power is transferred to the TE component (Figure 5.4(d)). Since the TE wave is not bound to the metal surface, less ohmic loss occurs in the metal resulting in a decrease of the propagation loss with increasing $\xi$ as seen in Figure 5.3. Near the metal surface, electromagnetic boundary conditions force the tangential field $E_y$ close to zero while the $E_x$ field is strongly enhanced. Far from the metal surface, the two fields are equal to each other. For $\xi \approx \xi_c$, the transverse field decay constant $k_{x1}$ in the chiral medium approaches zero, indicating that the mode is no longer bounded, as can be seen in Figure 5.4 (d). Thus the cut off condition occurs when enough power is transferred from the TM polarization to the TE polarization so that the mode is no longer bounded to the metal surface.

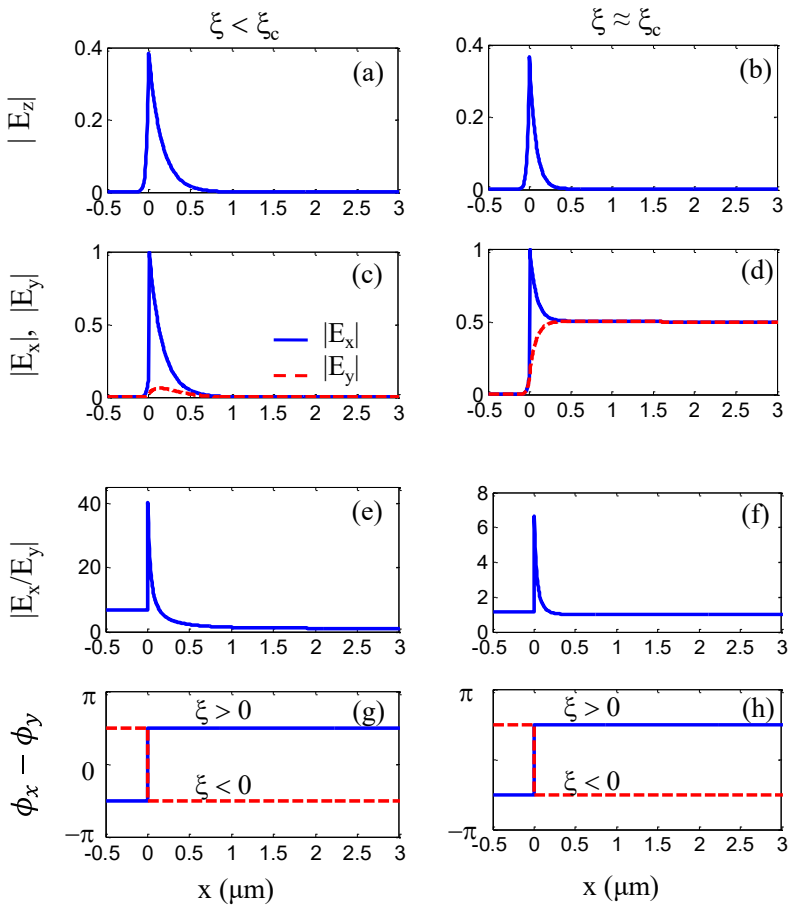


Figure 5.4. Field distributions of $|E_z|$, $|E_x|$, $|E_y|$, the ratio $|E_x/E_y|$, and phase angle difference $\phi_x - \phi_y$ of chiral-Au SP modes at λ = 0.6μm (left panels: $\xi = 10^{-4}\Omega^{-1}$, right panels: $\xi = 6.68\times 10^{-4}\Omega^{-1} \approx \xi_c$). The fields in (a)-(d) are normalized by the peak value of $|E_x|$.

It is also instructive to examine the polarization characteristics of the chiral SP mode. In Figure 5.4(e)-(h) we plot the ratio of the transverse field amplitudes $|E_x/E_y|$ and the phase angle difference between $E_x$ and $E_y$, $\phi_x - \phi_y$. Figure 5.4(g) shows that for $\xi > 0$, the phase angle difference between the two fields is identically $-\pi/2$ inside the metal and $+\pi/2$ in the chiral medium, indicating that the wave is elliptically polarized with opposite senses of rotation in the metal and the chiral medium. Since $|E_x/E_y| > 1$, the major axis of the polarization ellipse is oriented along the direction transverse to the metal surface, although far from the metal surface the field becomes circularly polarized since $|E_x/E_y| \approx 1$. The opposite directions of polarization rotation in the metal and chiral medium are a consequence of the fact that the dielectric constants of the metal and chiral material have opposite signs, which causes a π-phase change in the $E_x$ field at the

interface. Inside the metal the elliptically polarized light causes the electrons to execute a spiral motion as the charge density wave propagates forward. Changing the sign of the chirality parameter does not affect the magnitudes of the field components but reverses the senses of polarization rotation in the metal and chiral medium, as seen by the plots for $\xi < 0$ in Figure 5.4 (g) and (h).

## 5.2 Transfer Matrix Analysis of SPR Multi-layer Systems with Chiral Material

In the previous section, we investigated the propagation of chiral SPPs at a metal-chiral interface and found that the propagation length of a chiral SP mode near cut-off is very sensitive to the chiral parameter. This unique property can potentially be exploited for developing chiral sensors on an integrated platform. In this section, we analyze the reflection of light from a metal-chiral interface to investigate the influence of chirality on the cross-polarization reflection coefficient. In particular, we are interested in the role of SPPs in enhancing the chiral response, which can potentially be exploited for ellipsometric measurement of chirality.

In conventional plasmonic structures (with no chiral materials), there are two alternative configurations that can be used to excite SPPs, namely, the Kretschmann and Otto configurations. In this section we will investigate both configurations for exciting chiral SPPs. We will describe each of these systems below and derive the reflection matrix of the structure to analyze its response in the presence of chirality.

### *5.2.1 The Kretschmann configuration*

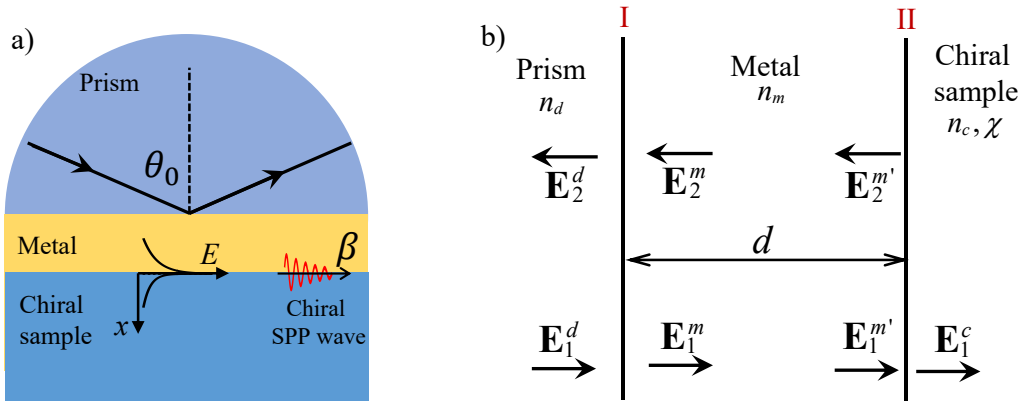


Figure 5.5 Schematic of the Kretschmann configuration for SP wave excitation: (a) cross-section view of the multi-layer SPR system along the plane of incidence; (b) electric fields in the various layers of the structure for transfer matrix analysis.

We first consider the Kretschmann configuration shown in Figure 5.5(a), which is the most common configuration for exciting SP waves. A metal thin film with refractive index $n_m$ and thickness $d$ is sandwiched between a dielectric prism of refractive index $n_d$ and a chiral sample. The chiral material has refractive index $n_c$ and chiral parameter $\chi$. To enable excitation of SP waves at the chiral-metal interface, the refractive index $n_d$ of the prism must be larger than $\mathrm{Re}\{n_c\}$. Light incident from the prism at an incidence angle $\theta_0$ greater than the critical angle $\theta_c = \mathrm{asin}(n_c/n_d)$ will experience total internal reflection, causing an evanescent wave to appear in the chiral sample. If the momentum of this evanescent wave matches that of the chiral SPP, then a chiral SP wave will be excited at the metal-chiral interface.

We employ the transfer matrix method to analyze light reflection from the metal-chiral interface in the Kretschmann SPR system. We use Jones vectors to represent the forward and backward propagating electromagnetic waves in the different layers of the SPR system, as shown in Figure 5.5(b). A linearly polarized (LP) plane wave $\mathbf{E}_1^{(d)} = \left[E_{1,p}^{(d)}, E_{1,\mathrm{s}}^{(d)}\right]^{\mathrm{T}}$ incident from the prism is reflected at the metal surface to give $\mathbf{E}_2^{(d)} = \left[E_{2,p}^{(d)}, E_{2,\mathrm{s}}^{(d)}\right]^{\mathrm{T}}$, where $E_{i,p}^{(d)}$ and $E_{i,\mathrm{s}}^{(d)}$ ($i$ = 1, 2) are the electric field amplitudes of *p*- and *s*- polarization components, respectively. The light transmitted through the metal layer into the chiral sample is denoted by $\mathbf{E}_1^{(c)} = \left[E_{1,+}^{(c)}, E_{1,-}^{(c)}\right]^{\mathrm{T}}$, where $E_{1,+}^{(c)}$ and $E_{1,-}^{(c)}$ are the electric field amplitudes of the LCP and RCP waves, respectively. Using the transfer matrix method, we can write

$$\begin{pmatrix} \mathbf{E}_1^{(d)} \\ \mathbf{E}_2^{(d)} \end{pmatrix} = \mathbf{M}_{\mathrm{I}} \mathbf{P}^{(m)} \mathbf{M}_{\mathrm{II}} \begin{pmatrix} \mathbf{E}_1^{(c)} \\ \mathbf{0} \end{pmatrix}, \tag{5.12}$$

where $\mathbf{M}_i$ ($i$ = I, II) are the transfer matrices of the prism-metal interface (I) and the metal-chiral interface (II), and $\mathbf{P}^{(m)}$ is the propagation matrix of the metal thin film. The transfer matrix of the prism-metal interface (I) has the form [127],

$$\mathbf{M}_{\mathrm{I}} = \begin{bmatrix} \mathbf{T}^{(dm)} & \mathbf{R}^{(dm)} \\ \mathbf{R}^{(dm)} & \mathbf{T}^{(dm)} \end{bmatrix}. \tag{5.13}$$

where $\mathbf{T}^{(dm)}$ and $\mathbf{R}^{(dm)}$ are given by

$$\mathbf{T}^{(dm)} = \begin{pmatrix} 1/t_p & 0 \\ 0 & 1/t_s \end{pmatrix} \text{ and } \mathbf{R}^{(dm)} = \begin{pmatrix} r_p/t_p & 0 \\ 0 & r_s/t_s \end{pmatrix}, \tag{5.14}$$

with $r_p$, $t_p$, $r_s$ and $t_s$ being the Fresnel coefficients of the prism-metal interface. The transfer matrix of the metal-chiral interface (II) is

$$\mathbf{M}_{\mathrm{II}} = \begin{bmatrix} \mathbf{T}^{(mc)} & \mathbf{R}^{(mc)} \\ \mathbf{R}^{(mc)} & \mathbf{T}^{(mc)} \end{bmatrix}, \tag{5.15}$$

where $\mathbf{T}^{(mc)}$ and $\mathbf{R}^{(mc)}$ can be calculated by substituting the optical parameters $(n_m, n_c, \chi)$ into Equations (4.32) - (4.35). The propagation matrix $\mathbf{P}^{(m)}$ in the metal is defined as

$$\mathbf{P}^{(m)} = \mathrm{diag}(\varphi_m^{-1}, \varphi_m^{-1}, \varphi_m, \varphi_m),\ \varphi_m = \exp(-jk_{xm}d), \tag{5.16}$$

where $k_{xm} = \sqrt{n_m^2 k_0^2 - n_d^2 \sin^2\theta_0}$ is the transverse propagation constant in the metal. By substituting the above matrices into Equation (5.12), we solve for the field $\mathbf{E}_2^{(d)}$ of the reflected light to get

$$\mathbf{E}_2^{(d)} = \left(\mathbf{R}^{(dm)}\mathbf{T}^{(mc)} + \varphi_m^2\mathbf{T}^{(dm)}\mathbf{R}^{(mc)}\right)\left(\mathbf{T}^{(dm)}\mathbf{T}^{(mc)} + \varphi_m^2\mathbf{R}^{(dm)}\mathbf{R}^{(mc)}\right)^{-1}\mathbf{E}_1^{(c)}. \tag{5.17}$$

The above equation will be used to calculate the reflection coefficients and the ellipsometric angles of the Kretschmann SPR system.

### *5.2.2 The Otto configuration*

An alternative configuration for exciting SPPs is the Otto configuration, which is shown in Figure 5.6(a). In this SPR system, a thin spacer layer (shown as a chiral medium in the figure) with a lower refractive index than the coupling prism is placed between the prism and the metal. Light incident at an angle larger than the critical angle is totally reflected at the prism-spacer interface, causing an evanescent wave to appear in the spacer layer. This evanescent wave can excite an SP wave at the spacer-metal interface if its momentum is matched with that of the SP mode. If the metal slab has a finite thickness, two SP modes can be excited, namely, a symmetric mode and an asymmetric mode [128]. The symmetric mode is also known as the Long-Range Surface Plasmon Resonance (LR-SPR) mode, which is characterized by much lower propagation loss and narrower bandwidth compared to conventional SPPs at a single dielectric-metal interface. LR-SPR has been exploited to enhance the sensitivity and resolution of SPR biosensors [129, 130] as well as thin film characterization systems [131]. In our research, we are also interested in exploring the possibility of using the LR-SPR mode in the Otto configuration to achieve enhanced detection of chiral substances. Toward this aim, we will first develop a transfer matrix formalism for analyzing

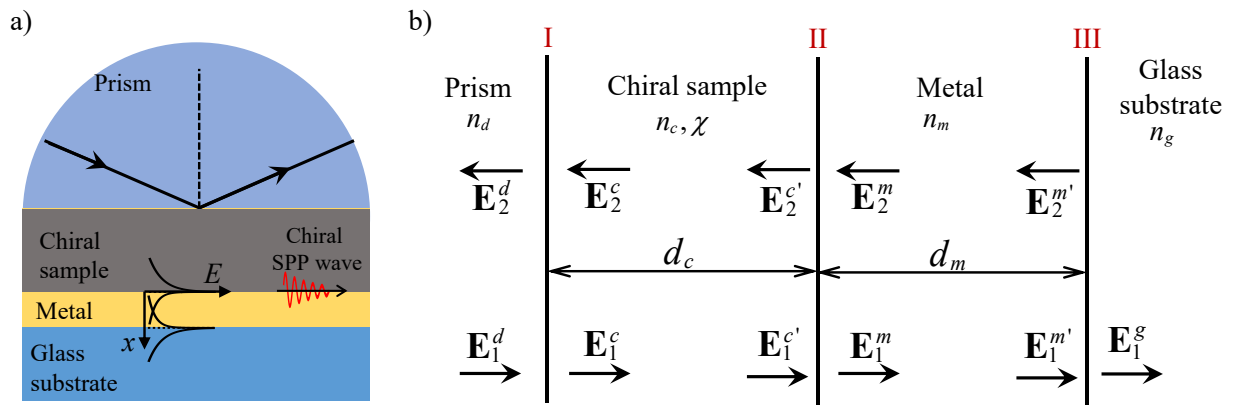


Figure 5.6 Schematic of the Otto configuration for SP wave excitation: (a) cross-section view of the multi-layer SPR system along the plane of incidence; (b) electric fields in the various layers of the structure for transfer matrix analysis.

light reflection from the Otto SPR system shown in Figure 5.6(a), where the spacer layer is replaced by a chiral sample whose chiral parameter is to be measured.

We assume the chiral layer has thickness $d_c$, refractive index $n_c$ and chiral parameter $\chi$. The prism index is $n_d$, which is assumed to be larger than $\mathrm{Re}\{n_c\}$. A metal thin film with thickness $d_m$ and index $n_m$ is deposited on a glass substrate with refractive index $n_g$. Figure 5.6(b) shows the electric fields in the various layers of the structure. Using transfer matrix analysis, we obtain the following relationship between the incident field $\mathbf{E}_1^{(d)} = \left[E_{1,p}^{(d)}, E_{1,\mathrm{s}}^{(d)}\right]^{\mathrm{T}}$, the reflected field $\mathbf{E}_2^{(d)} = \left[E_{2,p}^{(d)}, E_{2,\mathrm{s}}^{(d)}\right]^{\mathrm{T}}$ and the transmitted field $\mathbf{E}_1^{(g)} = \left[E_{1,p}^{(g)}, E_{1,\mathrm{s}}^{(g)}\right]^{\mathrm{T}}$:

$$\begin{pmatrix} \mathbf{E}_1^{(d)} \\ \mathbf{E}_2^{(d)} \end{pmatrix} = \mathbf{M}_{\mathrm{I}}\mathbf{P}^{(c)}\mathbf{M}_{\mathrm{II}}\mathbf{P}^{(m)}\mathbf{M}_{\mathrm{III}} \begin{pmatrix} \mathbf{E}_1^{(g)} \\ \mathbf{0} \end{pmatrix}, \tag{5.18}$$

where $\mathbf{M}_i$ ($i$ = I, II, III) are the transfer matrices of interfaces I, II and III as indicated in Figure 5.6, and $\mathbf{P}^{(c)}$ and $\mathbf{P}^{(m)}$ are the propagation matrices of the chiral layer and the metal thin film, respectively. The transfer matrix $\mathbf{M}_{\mathrm{I}}$ of the prism-chiral interface (I) is

$$\mathbf{M}_{\mathrm{I}} = \begin{bmatrix} \mathbf{T}^{(dc)} & \mathbf{R}^{(dc)} \\ \mathbf{R}^{(dc)} & \mathbf{T}^{(dc)} \end{bmatrix}, \tag{5.19}$$

where $\mathbf{T}^{(pc)}$ and $\mathbf{R}^{(pc)}$ can be calculated by substituting the optical parameters $(n_d, n_c, \chi)$ into Equations (4.32) - (4.34). The transfer matrix $\mathbf{M}_{\mathrm{II}}$ of the chiral-metal interface (II) can be obtained from Equations (4.28) and (4.29) to be

$$\mathbf{M}_{\mathrm{II}} = \begin{bmatrix} \mathbf{T}^{(cm)} & \mathbf{R}^{(cm)} \\ \mathbf{R}^{(cm)} & \mathbf{T}^{(cm)} \end{bmatrix}, \tag{5.20}$$

where

$$\mathbf{T}^{(cm)} = \frac{1}{2}\begin{bmatrix} -j\dfrac{1}{t_{+p}} & j\dfrac{1}{t_{-p}} \\ \dfrac{1}{t_{+s}} & \dfrac{1}{t_{-s}} \end{bmatrix}, \text{ and } \mathbf{R}^{(cm)} = \frac{1}{2}\begin{bmatrix} -j\dfrac{r_{+p}}{t_{+p}} & j\dfrac{r_{-p}}{t_{-p}} \\ \dfrac{r_{+s}}{t_{+s}} & \dfrac{r_{-s}}{t_{-s}} \end{bmatrix}. \tag{5.21}$$

The elementary coefficients $r_{ij}$ and $t_{ij}$ ($i$ =+, -, and $j$ = $p$, $s$) in the above equations are given by

$$r_{\pm s} = \frac{n_{ce}k_{x\pm} - n_{\pm}k_{xm}}{n_{ce}k_{x\pm} + n_{\pm}k_{xm}}, \qquad t_{\pm s} = \frac{2n_{ce}k_{x\pm}}{n_{ce}k_{x\pm} + n_{\pm}k_{xm}}. \tag{5.22}$$

$$r_{\pm p} = \frac{n_m^2 k_{x\pm} - n_{\pm}n_{ce}k_{xm}}{n_a^2 k_{x\pm} + n_{\pm}n_{ce}k_{xm}}, \quad t_{\pm p} = \frac{2n_m n_{ce}k_{x\pm}}{n_m^2 k_{x\pm} + n_{\pm}n_{ce}k_{xm}}. \tag{5.23}$$

The transfer matrix $\mathbf{M}_{\mathrm{III}}$ of the metal-glass interface (III) is

$$\mathbf{M}_{\mathrm{III}} = \begin{bmatrix} \mathbf{T}^{(mg)} & \mathbf{R}^{(mg)} \\ \mathbf{R}^{(mg)} & \mathbf{T}^{(mg)} \end{bmatrix}, \tag{5.24}$$

where $\mathbf{T}^{(mg)}$ and $\mathbf{R}^{(mg)}$ can be obtained from Equations (5.13) and (5.14) using refractive indices $n_m$ and $n_g$. The propagation matrix $\mathbf{P}^{(m)}$ of the metal layer is given by Equation (5.16), while the matrix $\mathbf{P}^{(c)}$ for the chiral layer is

$$\mathbf{P}^{(c)} = \mathrm{diag}(\varphi_-^{-1}, \varphi_+^{-1}, \varphi_-, \varphi_+), \ \varphi_{\pm} = \exp(-jk_{x\pm}d_c), \tag{5.25}$$

where $k_{x\pm} = \sqrt{n_{\pm}^2 k_0^2 - n_d^2 \sin^2\theta_0}$ are the transverse propagation constants of the LCP and RCP waves in the chiral medium. Substituting the above matrices into Equation (5.18), we solve for the reflected field to obtain the result

$$\mathbf{E}_2^{(d)} = \left(\mathbf{R}^{(dc)}\left(\mathbf{\Phi}^{(c)}\right)^{-1}\mathbf{A} + \mathbf{T}^{(dc)}\mathbf{\Phi}^{(c)}\mathbf{B}\right)\left(\mathbf{T}^{(dc)}\left(\mathbf{\Phi}^{(c)}\right)^{-1}\mathbf{A} + \mathbf{R}^{(dc)}\mathbf{\Phi}^{(c)}\mathbf{B}\right)^{-1}\mathbf{E}_1^{(d)} \tag{5.26}$$

where

$$\mathbf{A} = \varphi_m^{-1}\mathbf{T}^{(cm)}\mathbf{T}^{(mg)} + \varphi_m\left(\mathbf{\Phi}^{(c)}\right)^{-1}\mathbf{R}^{(cm)}\mathbf{R}^{(mg)}, \tag{5.27}$$

$$\mathbf{B} = \varphi_m^{-1}\mathbf{\Phi}^{(c)}\mathbf{R}^{(cm)}\mathbf{T}^{(mg)} + \varphi_m\mathbf{T}^{(cm)}\mathbf{R}^{(mg)}. \tag{5.28}$$

We have thus derived above the reflection matrices for both the Kretschmann and Otto SPR systems embedded with a chiral layer. In the next section, we will simulate the reflection spectra for each system and analyze the results to evaluate the performance of each configuration for ellipsometric measurement of OR and CD chirality.

## 5.3 Surface Plasmon Resonance Enhanced Ellipsometry for Chiral Measurement

In Chapter 4, we demonstrated a differential ellipsometric method for chiral sensing based on reflection from a dielectric-chiral interface near the critical incidence angle. The method interrogates the change in the ellipsometric phase angle of the reflected beam, which has a strong dependence on the chirality of the sample. In this section, we perform simulations of light reflection from a chiral SPR system in the Kretschmann and Otto configurations to investigate the dependence of the ellipsometric angles on the OR and CD chirality of the sample. The results will be used to study the role of chiral SPPs in enhancing the ellipsometric response in each configuration, and to compare the performance of SPR-enhanced ellipsometry methods to the previously demonstrated method based on critical angle incidence at a dielectric-chiral interface. We will first describe the materials and optical parameters employed in the simulations.

*Materials and parameters*

The optical parameters used in the simulations are summarized in Table 5.1. The chiral sample is prepared as a PMMA host polymer ($n_c$ = 1.49 – 1.51) with chiral molecules dissolved in it. The prism material is assumed to be N-BAF10 glass, which is chosen to have a higher refractive index ($n_d$ = 1.67) than the index of the chiral sample [132]. The substrate material is assumed to be Borofloat glass [133], which has a refractive index ($n_g$ = 1.46 – 1.48) close to that of the host polymer of the chiral sample for efficient excitation of the LR-SPR mode in the Otto configuration.

Two metals commonly used in SP structures are Al and Ag. For measurement of OR chirality at 589nm wavelength, we will use Ag, which is one of the most widely-used noble metals in SPR sensors operating in the visible wavelengths around 600nm [120, 134]. On the other hand, Al is preferred over noble metals such as Au and Ag for plasmonic applications in the UV and blue wavelengths due to its lower loss in this wavelength range [135, 136]. Examples of Al-based plasmonic applications include SP-enhanced Raman spectroscopy [137] and SP-enhanced

fluorescence spectroscopy [138]. In our simulations, we will use Al to study SP-enhanced ellipsometry for measuring CD chirality at 400nm.

Two types of chiral samples are considered in our simulation studies: a transparent chiral sample with OR chirality, and an absorbing chiral sample with CD chirality. For realistic simulation results, we extracted the values of the index $n_c$ and chiral parameter $\chi$ from actual chiral samples. The chiral samples are prepared by blending chiral molecules in a host polymer, which can be deposited by spin-coating technology. The OR sample consists of a PMMA host doped with (+)-griseofulvin. The refractive index $n_c$ and chiral parameter $\chi$ of the sample are calculated from the wavelength dispersion relations given in [139]. Their values are shown in Table 5.1.

The CD chiral sample is a PMMA host doped with (-)-Riboflavin. We prepared this sample by dissolving ~0.5mM (-)-Riboflavin in PMMA 950 A2 solution and casting a thin film of ~10μm thickness on a spectroscopic glass slide. Figure 5.7 shows the absorbance spectrum (blue) and the CD spectrum (red) measured using a Hitachi UH-3000 UV-Vis Spectrophotometer and Olis DSM 17 Circular Dichroism. The absorbance $A$ is defined as

$$A = -\log\left(\exp(-2\kappa k_0 L)\right), \tag{5.29}$$

where $k_0$ is the vacuum wave number, $\kappa = \mathrm{Im}\{n_c\}$ is the extinction coefficient and $L$ the optical path length. From the absorbance spectrum, we determine the extinction coefficient of the sample by

$$\kappa(\lambda) = \frac{A(\lambda) * \ln(10) * \lambda}{4\pi L}. \tag{5.30}$$

| | | **OR** | **CD** |
|---|---|---|---|
| **Wavelength** | | 589nm | 400nm |
| **Refractive Index** | N-BAF10 prism, $n_d$ | 1.670 | 1.696 |
| | Chiral medium, $n_c$ | 1.491 | $1.51 - 6.08\times10^{-4}j$ |
| | Metal, $n_m$ | 0.046838- 3.9485$j$ (Ag) | 0.46555-4.7121$j$ (Al) |
| | Glass substrate, $n_g$ | 1.458 | 1.482 |
| **Chiral parameter $\chi$** | | $2.1127\times10^{-7}$ | $5.0822\times10^{-7}j$ |

Table 5.1 Parameters used in the simulation studies of SPR-enhanced ellipsometric measurement of OR and CD chirality using the Kretschmann and Otto configurations.

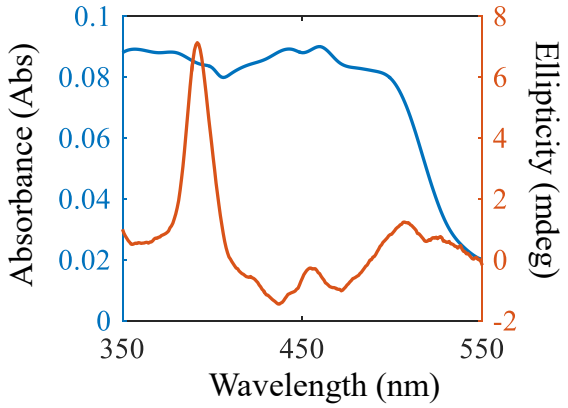


Figure 5.7 Measured absorbance spectrum (blue curve) and CD spectrum (red curve) of the CD sample consisting of PMMA host doped with (-)-Riboflavin.

The CD chiral parameter ($\mathrm{Im}\{\chi\}$) was extracted from the CD spectrum as follows. The ellipticity $\theta$ can be transformed to the differential absorbance of LCP and RCP light $\Delta A$ by $\Delta A = \theta/32.982$ ($\Delta A = A_L - A_R$ as described in section 4.2) [132]. Thus the imaginary chiral parameter $\chi$ characterizing CD chirality can be calculated from

$$\mathrm{Im}\{\chi(\lambda)\} = \frac{\theta(\lambda) * \ln(10) * \lambda}{32.982 * 8\pi * L * n_c(\lambda)}. \tag{5.31}$$

The CD spectrum of the measured sample has a peak value at 400nm wavelength. Therefore, to achieve maximum SNR, we choose to perform SPR ellipsometry simulations at this wavelength for the CD sample.

### *5.3.1 SPR-enhanced ellipsometric measurement of an OR chiral sample*

We first investigate the performance of SPR-enhanced ellipsometry for measuring a transparent chiral medium with OR chirality. Using the transfer matrix method described in Section 5.2, we performed simulations of light reflection at 589nm wavelength from a chiral SPR multi-layer in both the Kretschman and Otto configurations. The chiral sample is transparent with index $n_c$ and chiral parameter $\chi$ values given in Table 5.1.

For the Kretschmann system we used Ag film with a thickness of 54nm. The *p*-polarization reflection coefficient amplitude $|R_{pp}|$ as a function of the incidence angle is plotted in Figure 5.8(a), showing a SPR resonance dip around 74.4˚. Recall that in the differential ellipsometric method, we calculate

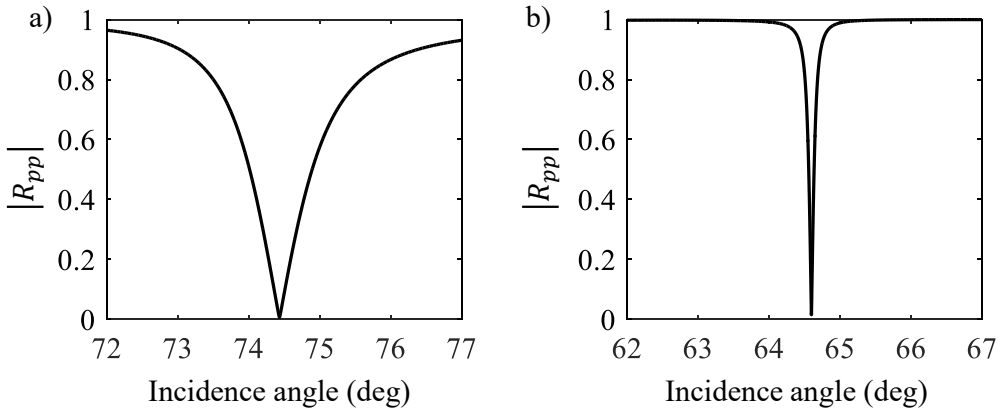


Figure 5.8 Plots of the magnitude of the *p*-polarization reflection $|R_{pp}|$ vs. the incidence angle for (a) the Kretschmann SPR system and (b) the Otto SPR system. The chiral sample is a transparent medium with OR chirality and the wavelength is fixed at 589nm.

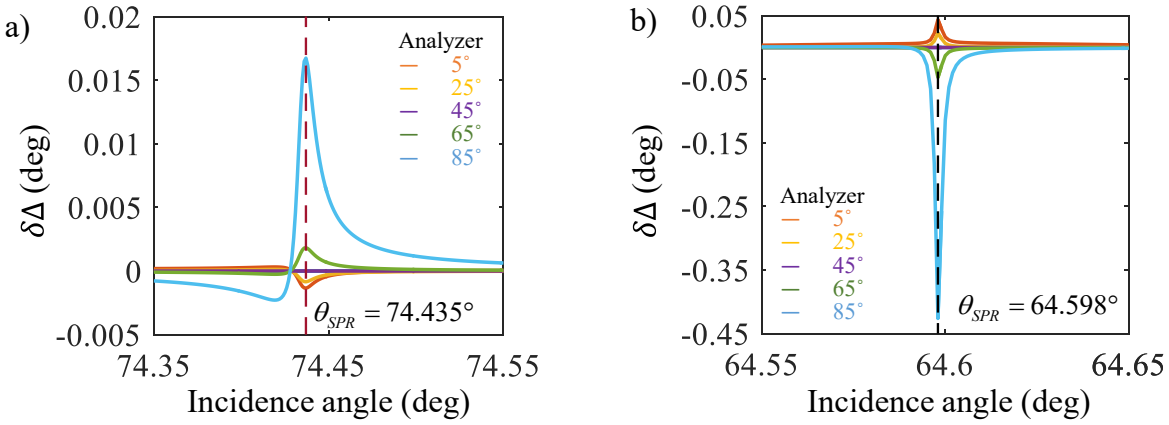


Figure 5.9 Simulation results for the phase angle difference δΔ of a transparent chiral sample with OR chirality at various analyzer angle settings: (a) the Kretschmann SPR system and (b) the Otto SPR system. The wavelength is fixed at 589 nm.

the ellipsometric phase angle Δ at two different analyzer angles, $A_{REF}$ and $A$, and use the response of the phase angle difference, $\delta\Delta = \Delta_A - \Delta_{AREF}$, to extract the chiral parameter χ of the sample. In the simulations, we fixed the reference analyzer angle $A_{REF}$ at 45˚ with respect to the *p*-polarization, and varied the analyzer angle $A$ from 5˚ to 85˚. Figure 5.9(a) shows the plot of the ellipsometric phase angle difference δΔ vs. the incidence angle at different settings of analyzer angle $A$. The phase angle difference is seen to peak at the incidence angle 74.435˚, which coincides with the angle at which the SP wave is excited at the chiral-metal surface. The peak value of $|\delta\Delta|$ depends

on the analyzer angle as predicted by Equation (4.21), becoming larger as the analyzer angle $A$ approaches 90˚.

For the Otto system, we used Ag thin film with 27 nm thickness, while the thickness of the chiral sample was fixed at 850nm. The thickness of the Ag film was chosen such that the Otto configuration gave a similar extinction ratio for the angular SPR resonance dip (as indicated by $|R_{pp}|$ plotted in Figure 5.8(b)) as in the Kretschmann system. Figure 5.9 (b) shows the plot of the phase angle difference vs. the incidence angle for the Otto structure at different settings of the analyzer angle $A$. The phase angle difference $|\delta\Delta|$ is also seen to peak at the surface plasmon resonance angle, which is 64.598˚ for the Otto system. The peak value of $|\delta\Delta|$ is also largest for analyzer angles close to 90˚. Note, however, that the phase angle difference for the Otto system is over 20 times larger than that achieved in the Kretschmann system.

Figure 5.9 indicate that the ellipsometric phase angle response is strongly enhanced by the excitation of chiral SPPs in both the Kretschmann and Otto systems. To further shed light on the mechanism for this enhancement, we examine in Figure 5.10(a) and (b) the magnitude of the cross-polarization reflection coefficient $R_{sp}$ and the reference ellipsometric phase angle $\Delta_{REF}$ near the SPR angle for both systems. The magnitude of $R_{sp}$ characterizes the degree of chiral-induced rotation in the polarization of the reflected beam, while the reference ellipsometric phase angle $\Delta = \mathrm{Arg}(R_{pp} + R_{ps}\tan 45°) - \mathrm{Arg}(R_{ss} + R_{sp}\cot 45°)$ can provide information about the sensitivity of the SPR system to perturbations, such as changes in the chiral parameter. Both plots in Figure 5.10 show that the magnitude of $R_{sp}$ reaches a peak value at the resonance angle of the corresponding SPR system, while the phase angle $\Delta$ undergoes a sharp transition. These results verify that chiral effects on the ellipsometric response are enhanced as a result of the SPP excitation. We also observe that compared to the Kretschmann system, the Otto system based on LR-SPR excitation provides a much stronger cross-polarization reflection and a steeper phase transition slope at the resonance angle. Both of these features can be exploited to achieve enhanced ellipsometric detection of OR chirality using the Otto configuration.

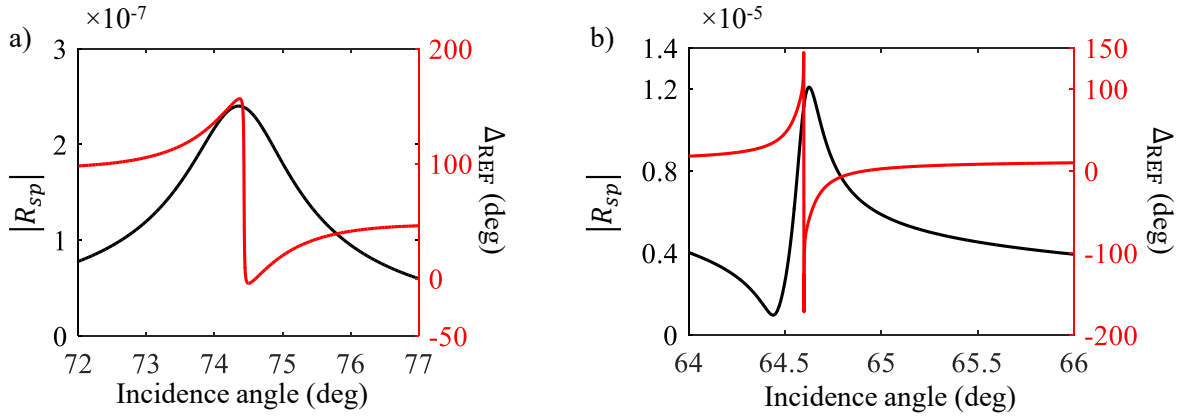


Figure 5.10 Plots of the magnitude of the cross-polarization reflection $|R_{sp}|$ and the reference ellipsometric phase angle $\Delta_{REF}$ vs. the incidence angle for (a) the Kretschmann SPR system and (b) the Otto SPR system. The chiral sample is a transparent medium with OR chirality and the wavelength is fixed at 589nm.

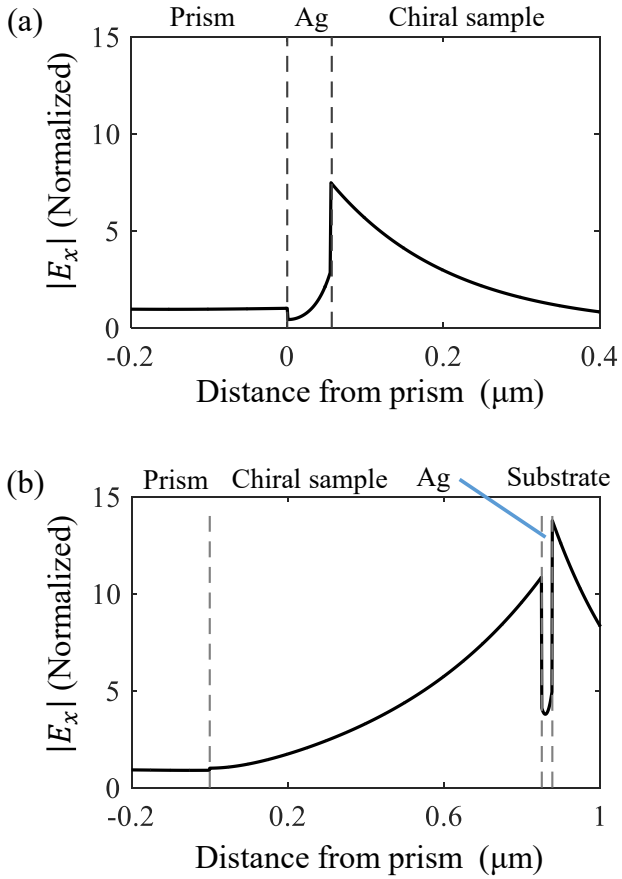


Figure 5.11. Distribution of the normal field component ($E_x$) in (a) the Kretschmann multi-layer structure and (b) the Otto multi-layer structure. The chiral sample is a transparent medium with OR chirality. The SP mode is excited at the incidence angle corresponding to the maximum phase angle difference response.

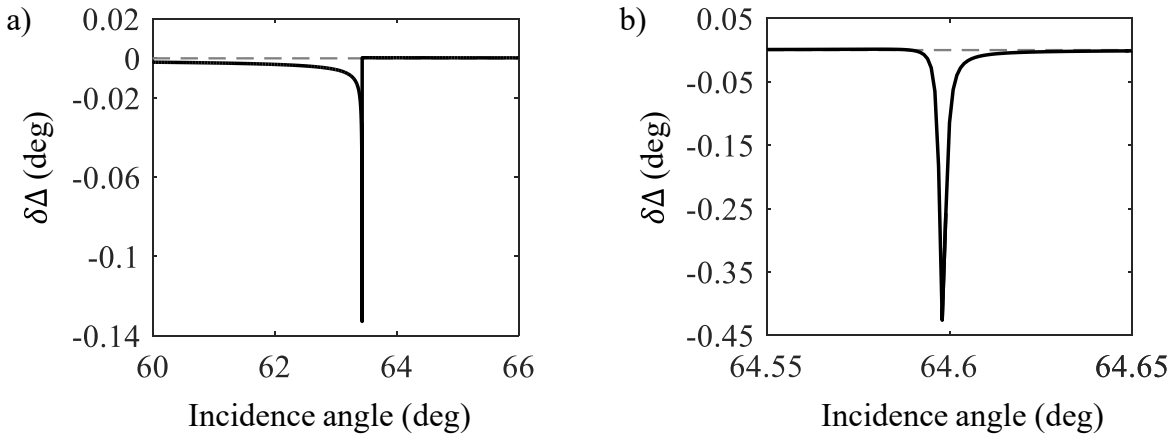


Figure 5.12 Plot of the phase angle difference δΔ vs. incidence angle for (a) ellipsometry based on reflection from a dielectric-chiral interface and (b) SPR-enhanced ellipsometry based on the Otto configuration. The chiral sample is a transparent medium with OR chirality. The analyzer angle A is set at 85˚ for both cases.

It is also instructive to compare the distributions of the normal field component $E_x$ in the two SPR multi-layer structures. The SP field distributions normalized with respect to the incident field are plotted in Figure 5.11(a) for the Kretschmann system and (b) for the Otto system. It can be seen that a much stronger electric field exists at the chiral-metal interface in the Otto system than in the Kretschmann system. This amplified electric field leads to stronger interaction with the chiral medium, resulting in the strong cross-polarization reflection observed in Figure 5.11(b).

Surface plasmon enhanced chiral effects have been observed previously in metal nanoparticles (NPs) coated with chiral molecules. For example, a strong SPP enhancement in the CD signal of bimane chromophore is observed when the CD band of the attached chiral molecule overlaps with the resonance spectrum of the plasmonic NPs [124, 133]. In the case where there is no overlap between the CD band of the chiral molecule and the plasmon resonance of the NPs, a new CD band can appear at the SP frequency, as observed for NPs dressed with various molecules [91, 133]. However, enhanced chiral effects due to SP waves at a chiral-metal planar interface embedded in SPR systems have not been reported before.

Finally, we compare the ellipsometric phase angle response of reflection from a dielectric-chiral interface at critical incidence angle with that of reflection from a metal-chiral interface at the SP resonance angle. The dielectric medium in the former structure is assumed to be the prism ($n_d = 1.670$). The ellipsometric phase angle difference is shown in Figure 5.12(a) for the dielectric-chiral interface and in Figure 5.12(b) for the Otto SPR system. We observe that the peak

value of |δΔ| obtained at the metal-chiral interface is three times larger than that at the dielectric-chiral interface. These results illustrate the superior performance of SP-enhanced ellipsometry compared to conventional ellipsometry based on reflection from a dielectric interface for chiral detection.

### *5.3.2 SPR-enhanced ellipsometric measurement of a CD chiral sample*

Next we examine the performance of SPR-enhanced ellipsometry for measuring an absorbing chiral sample with CD chirality. The chiral sample is assumed to have complex refractive index $n_c = 1.51 - 6.08\times10^{-4}j$ and imaginary chiral parameter $\chi = 5.0822\times10^{-7}j$ around 400nm wavelength. For the Kretschmann system, we chose Al as the metal layer with a thickness of 19nm for optimized SPR response at this wavelength. We used the same N-BAF10 prism as in the previous simulation study. The *p*-polarization reflection coefficient amplitude $|R_{pp}|$ as a function of the incidence angle is plotted in Figure 5.13(a), showing a SPR resonance dip around 70.2˚. Figure 5.15(a) shows the plot of the ellipsometric phase angle difference vs. the incidence angle for various values of analyzer angle *A*. The reference analyzer angle $A_{REF}$ is fixed at 45˚. We observe that as in the case of a transparent OR medium, the angle |δΔ| also peaks at the SP resonance angle of 70.22˚ for this structure, indicating that CD chiral effect is also enhanced by the excitation of SPPs.

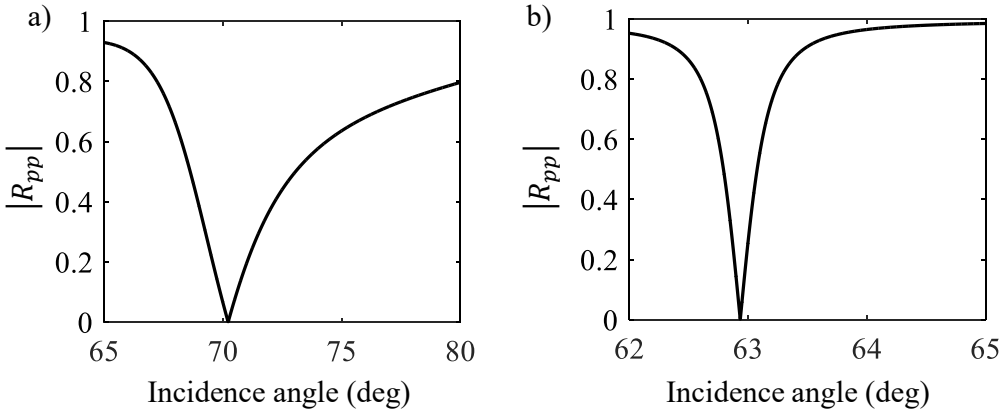


Figure 5.13 Plots of the magnitude of the *p*-polarization reflection $|R_{pp}|$ vs. the incidence angle for (a) the Kretschmann SPR system and (b) the Otto SPR system. The chiral sample is an absorbing chiral medium with CD chirality and the wavelength is fixed at 400nm.

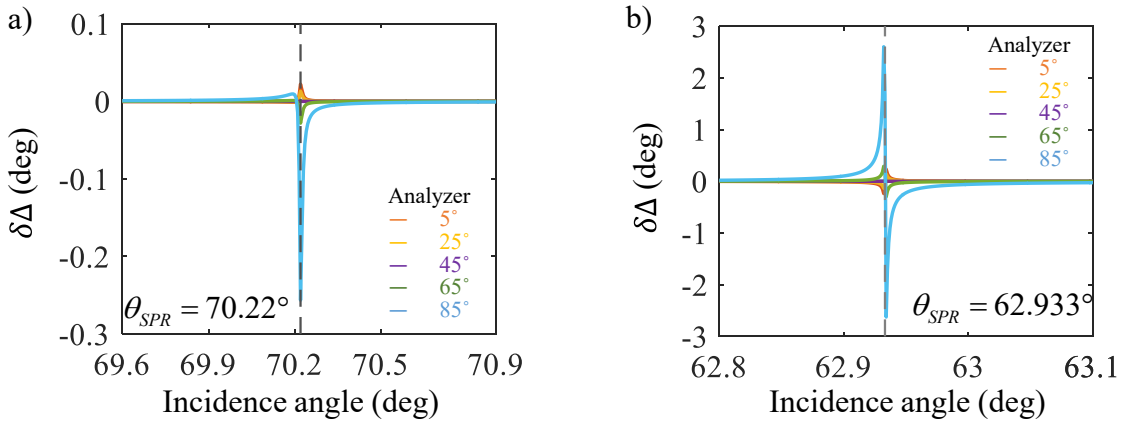


Figure 5.14 Simulation results for the phase angle difference δΔ of an absorbing chiral sample with CD chirality at various analyzer angle settings: (a) the Kretschmann SPR system and (b) the Otto SPR system. The wavelength is fixed at 400 nm.

For the Otto system, we employed a multi-layer structure consisting of an N-BAF10 prism, an Al film of 12nm thickness, and Borofloat glass as the support substrate. The chiral sample layer had a thickness of 495 nm, with the same index and chiral parameter as in the Kretschmann system. $|R_{pp}|$ of this Otto system is plotted in Figure 5.13(b) vs. the incidence angle, showing a SPR resonance dip with similar extinction ratio to that of the Kretschmann configuration (Figure 5.13(a)). The plots of $|\delta\Delta|$ vs. the incidence angle at different analyzer angles are given in Figure 5.15(b). We observe that the angle $|\delta\Delta|$ also peaks at the corresponding resonance angle of 62.933˚ for this SPR system; however, the magnitudes of the peak $|\delta\Delta|$ angle are almost an order of magnitude larger than those obtained in the Kretschmann system.

Figure 5.15(a) and (b) compare the magnitude of the cross-polarization reflection coefficient $|R_{sp}|$ and the reference ellipsometric phase angle $\Delta_{REF}$ near the resonance angle for the Kretschmann and Otto systems, respectively. Again, we observe that the Otto configuration provides over an order of magnitude enhancement in $|R_{sp}|$ and a larger jump in the phase angle near the SP resonance compared to the Kretschmann configuration. Figure 5.16(a) and (b) show the normal electric field distributions of the SP modes in the Kretschmann and Otto multi-layer structures. These field distributions are similar to those shown in Figures 5.10(a) and (b) for a transparent OR sample, indicating that the presence of loss in the chiral medium does not significantly alter the field distributions in these SPR structures.

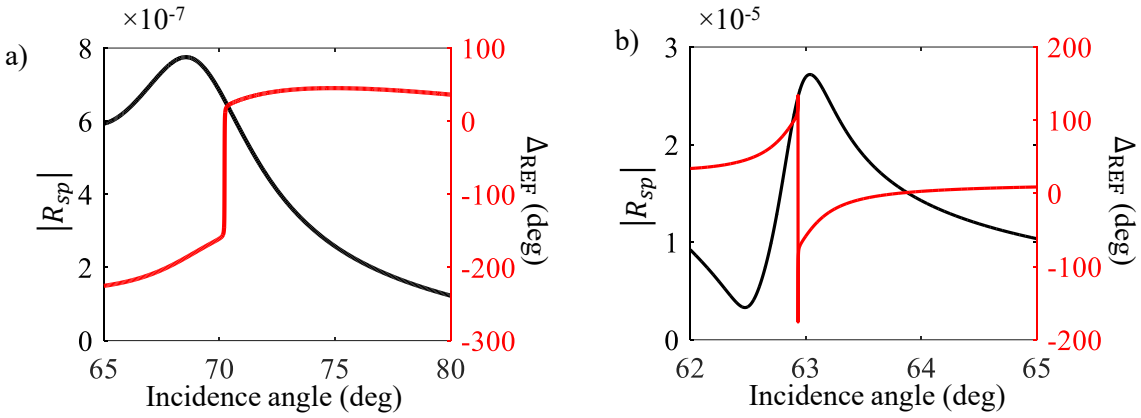


Figure 5.15 Plots of the magnitude of the cross-polarization reflection $|R_{sp}|$ and the reference ellipsometric phase angle $\Delta_{REF}$ vs. the incidence angle for (a) the Kretschmann SPR system and (b) the Otto SPR system. The chiral sample is a lossy medium with CD chirality and the wavelength is fixed at 400 nm.

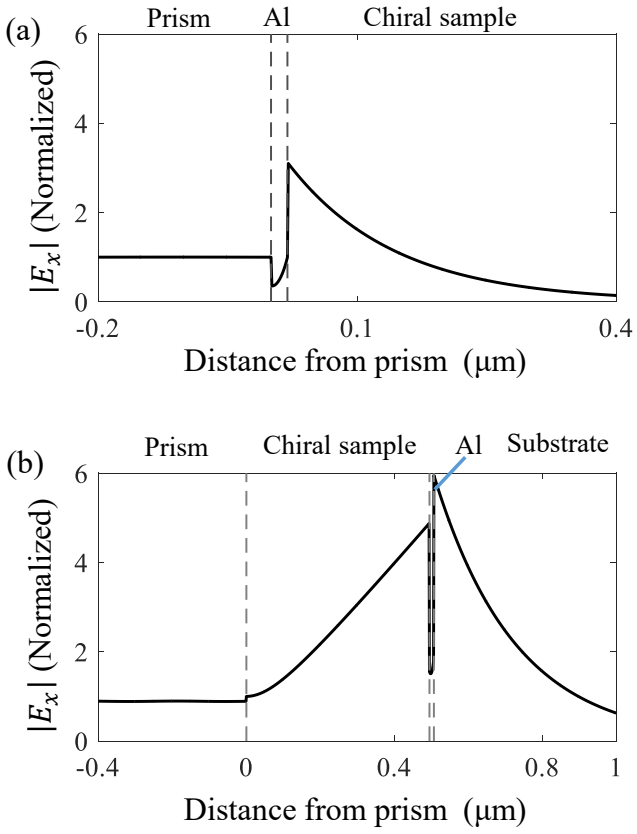


Figure 5.16 Distribution of the normal field component ($E_x$) in (a) the Kretschmann multi-layer structure and (b) the Otto multi-layer structure. The chiral sample is a lossy medium with CD chirality. The SP mode is excited at the incidence angle corresponding to the maximum phase angle difference response.

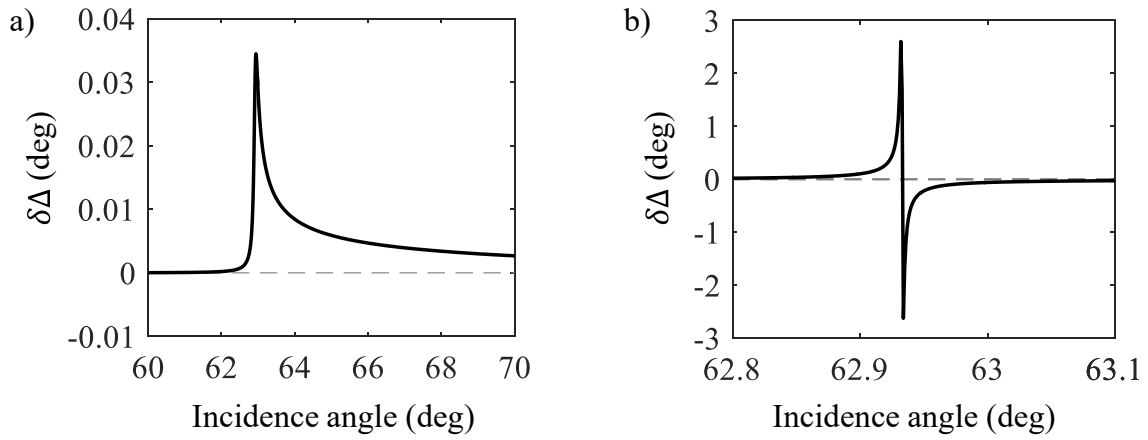


Figure 5.17 Plot of the phase angle difference δΔ vs. incidence angle for (a) ellipsometry based on reflection from a dielectric-chiral interface and (b) SPR-enhanced ellipsometry based on the Otto configuration. The chiral sample is a lossy medium with CD chirality. The analyzer angle A is set at 85˚ for both cases.

We also compare the ellipsometric phase angle response of the Otto structure with that of a dielectric-chiral interface for a CD chiral sample. The response of the latter is shown in Figure 5.17(a) while that of the former is shown in Figure 5.17(b). In both structures we used the same refractive index $n_c$ and chiral parameter $\chi$ for the CD sample as those in Table 5.1. We observe that the peak |δΔ| angle is enhanced by nearly two orders of magnitude in the Otto system compared to the dielectric-chiral structure, indicating SPR-enhanced ellipsometry should have much better SNR and hence detection resolution than conventional ellipsometry for chiral measurement of CD sample.

Finally, we investigate the dependence of the phase angle difference δΔ of SPR-enhanced ellipsometry on the OR and CD chiral parameters. Figure 5.18(a) and (b) show the plot of δΔ vs the real and imaginary part of the chiral parameter, respectively, for the Kretschmann (black curve) and Otto (red curve) configurations. In both systems, the analyzer angles are $A_{\mathrm{REF}} = 45^{\circ}$ and $A = 85^{\circ}$, and the incidence angle is set at the angle for SPR excitation, which corresponds to the peak δΔ response. We see from the plots that for both SPR systems, the phase angle difference has a strong correlation to the chiral parameter, with its sign depending on the sign of the chiral parameter and hence the handedness of the enantiomer. We also note that the Otto system has a higher sensitivity to the chiral strength for both OR and CD samples, making it the preferred configuration for SPR-enhanced ellipsometric measurement of chirality.

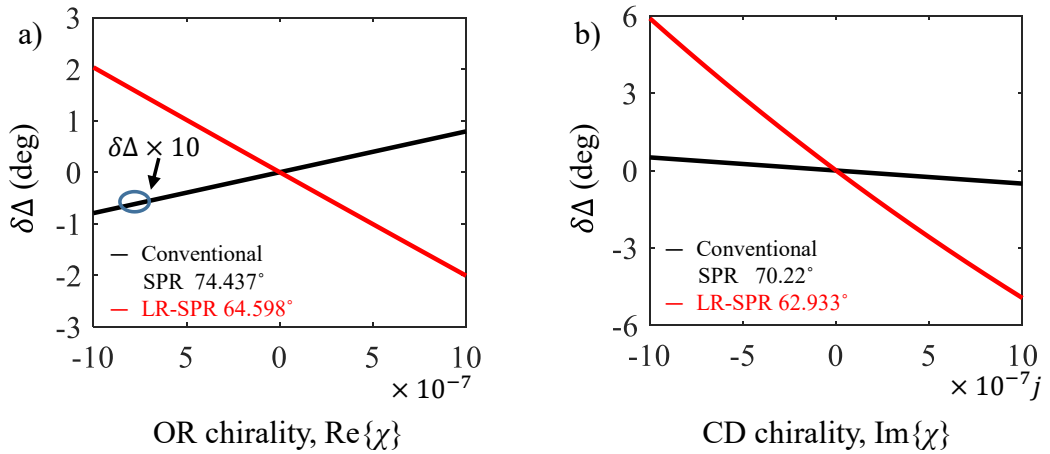


Figure 5.18 Simulated phase angle difference δΔ vs. the chiral parameter for (a) OR chirality and (b) CD chirality. The red lines are the responses of the Otto system; the black curves are the responses of the Kretschmann system. The incidence angle is set to provide the maximum response in each case and the analyzer angle A is fixed at 85˚.

To summarize the results of this section, we have shown that the excitation of chiral SPPs at a chiral-metal surface leads to enhancement in the ellipsometric response of both the Kretschmann and Otto multi-layer structures. In particular, thanks to the excitation of LR-SPP waves, the differential ellipsometry method based on the Otto configuration provides better SNR and hence better chiral detection resolution than both ellipsometry based on the Kretschmann structure and conventional ellipsometry based on reflection from a dielectric-chiral interface. We also note that the differential ellipsometric method can also be used to measure the refractive index of the sample, similar to refractometric sensors based on SPR [120] and SPR-enhanced ellipsometry [9]. Thus, the proposed SPR-enhanced ellipsometry method can provide a universal tool for complete characterization of a chiral medium in terms of its refractive index, OR and CD chiralities, which are traditionally profiled using different sensing techniques such as SPR sensor, refractometer, polarimetry, and CD spectroscopy. Furthermore, the Otto configuration uses a chiral sample with sub-micron thickness, thus significantly reducing the required sample volume. Combined with nanofluidics technology, the proposed chiral sensing method can potentially provide an important tool for pharmacokinetic studies of chiral drugs and other biochemical substances.

## 5.4 Preliminary Experiment of SPR-Enhanced Measurement in a Commercial Ellipsometer

We have done some preliminary work to study the feasibility of implementing the LR-SPR enhanced differential ellipsometric method in a commercial ellipsometer. However, it was found that due to the weak broadband light source of the commercial ellipsometer used, the ellipsometric phase angle difference signal could not be accurately measured. We briefly summarize the results of our experiment below and suggest solutions for overcoming the technical challenges in future implementations of SPR-enhanced ellipsometry.

*Sample preparation*

We prepared a LR-SPR multi-layer chip in the Otto configuration with PMMA as the measurement sample. A $20\times20mm^2$ chip was diced from a 1.1mm-thick Borofloat glass wafer and cleaned in a 20-minute Piranha bath, followed by a rinse in DI water and blow-dry with $N_2$. The glass chip was coated with a 12nm-thick Al film using an Electron Beam Evaporation system under $1.6\times10^{-7}$Torr vacuum and at deposition speed of ~0.12nm/sec. The chip was then spin-coated with a ~520nm-thick PMMA layer at a spin speed of 1500RPM. The thicknesses of the Al and PMMA layer were chosen to achieve LR-SPR excitation by light incidence through a BK-7 dove prism. The chip was mounted in contact with the prism via a BK-7 index matching liquid from Cargille Labs.

*Measurement results*

We performed spectroscopic measurements of the ellipsometric amplitude angle $\psi$ and phase angle $\Delta$ using an M-2000v ellipsometer. Before the measurements, the chip was mounted and aligned in the ellipsometer following the alignment procedure specified in the system software. The incidence angle was set at 69˚. Measurements over the wavelength range 400 nm – 900 nm were performed at various analyzer angle settings.

Figure 5.19(a) shows the wavelength variations of the measured phase angle $\Delta$ at analyzer angles of 45˚, 60˚, 75˚ and 85˚. The black curve is the signals collected at the 45˚ analyzer angle setting, which is also the default setting of conventional standard ellipsometry for measuring the refractive index and thickness of thin films. The amplitude angle $\psi$ measured at analyzer angle 45˚ is plotted by the red curve in Figure 5.19(b), showing a sharp dip around 470nm wavelength which corresponds to the excitation of the LR-SPR mode. As shown in the inset in Figure 5.19(a),

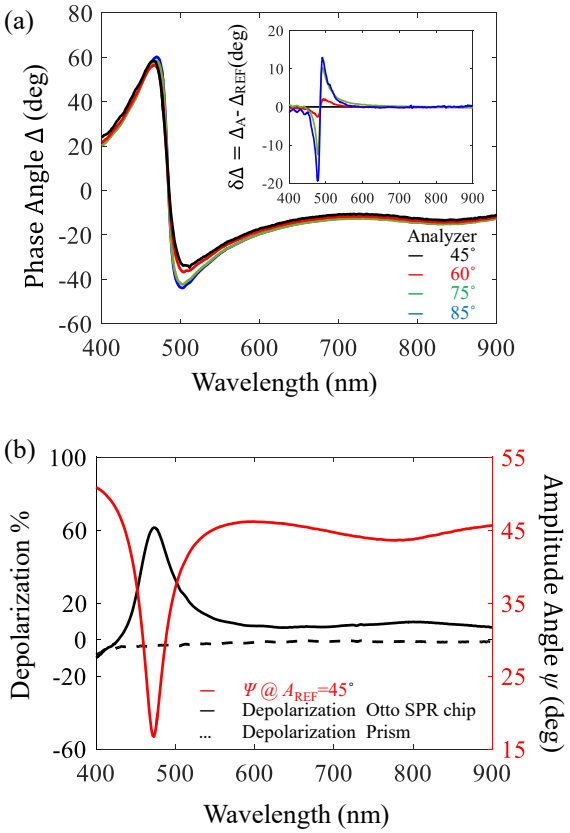


Figure 5.19 Measurement data showing the wavelength dependence of (a) the phase angle Δ of an Otto SPR multi-layer structure obtained at various analyzer angle settings (b) the amplitude angle $\psi$ and Depolarization factor. The black dashed line in (b) shows the Depolarization factor measured with the prism only. The inset in (a) shows the phase angle difference δΔ relative to measurements at the reference analyzer angle of 45˚.

the phase angle Δ measured at different analyzer angles deviates from that measured at $A$=45˚ around the SPR wavelength, and the difference δΔ becomes larger as the analyzer angle is increased. It is interesting to note that the phase angle difference δΔ remains close to zero at frequencies far from the resonance. We recall that for an ideal Otto SPR chip using an achiral sample (PMMA), the phase angle difference δΔ should remain zero for all frequencies. To determine the origin of this non-zero response of the phase angle difference, we plotted the Depolarization factor vs. wavelength in Figure 5.19(b) for the Otto SPR system (solid black line) and the prism alone (dashed black line). Depolarization characterizes the depolarization effect of the sample system, and is defined by [140]

$$\text{Depolarization} = 1 - P, \tag{5.32}$$

where $P$ is the degree of polarization. For an ideal isotropic sample, $P$ can be written as [140]

$$P = \cos^2(2\psi) + \sin^2(2\psi)\cos^2\Delta + \sin^2(2\psi)\sin^2\Delta, \tag{5.33}$$

thus its Depolarization is zero. For a depolarizing sample, $P$ becomes less than unity, and Depolarization becomes non-zero. Common sources of depolarization effect include sample surface roughness, non-uniformity of thin film thickness, and incoherent backside reflection from transparent substrates [140, 141]. Since the observed depolarization effect of the SPR chip shows a strong correlation to SPR excitation, we can draw the conclusion that one major cause of this non-ideal phenomenon is the non-ideality defects of the metal thin film such as grain size and surface roughness. For Al thin films prepared using E-beam Evaporation technology, typical grain size is 20-50nm and the surface roughness is commonly >1nm [142]. Another contributing source to the depolarization effect is the thickness non-uniformity in the PMMA thin film and the Refractive Index Matching Liquid layer.

Besides the depolarization effect at the SPR excitation, the *p*-polarization reflection from the SPR system is significantly reduced so that measurement of the reflected *p*-polarization is less accurate, which also contributes to the large deviations in the phase angle difference as the analyzer angle approaches the *s*-polarization (or 90˚). On the other hand, at the off-resonance frequencies, both *p*- and *s*- polarization components are strongly reflected from the SPR multi-layer so that there is a considerable amount of light intensity from both polarizations reaching the detector, which ensures accurate determination of the ellipsometric angles ($\psi$, $\Delta$) at these off-resonance frequencies.

*Suggested solution for future implementations*

Since the observed phase angle difference $\delta\Delta$ of the SPR chip appears to be closely related to the depolarization effect at SP resonance excitation, we may minimize this non-ideal behaviour by suppressing the depolarization effect. One solution is to employ smoother metal thin films to provide near ideal planar surface, which can be obtained by deposition technologies such as Atomic Layer Deposition [143] and co-sputtering [144]. On the other hand, we also note this strong depolarization effect observed at SPR condition may have applications in characterizing the quality of metal thin films. Though depolarization effect has been employed in conventional ellipsometry data fitting to reduce unwanted cross-polarization reflection [140, 141], the use of SPR-induced depolarization effect for metal thin film quality check has not been reported.

It may also be possible to develop an analysis algorithm that can take into account the depolarization effect, where phase angle difference $\delta\Delta$ is assumed to consist of an off-set response due to depolarization and a chiral-induced response. By subtracting the depolarization response from the measured phase angle difference, we could then extract the chiral parameter of the sample.

Also since commercial ellipsometers typically employ broadband lamps with low spectral power density, we suggest that using a tunable laser light source along with a precision phase angle interrogation setup may help improve the SNR of the measurements, especially near the SPR excitation frequency. Ellipsometer systems equipped with laser sources and specialize angle interrogation setups have been developed by other groups for specific applications with different configurations [145-147]. These systems commonly use an electro-optic modulator to vary the phase or amplitude of the incident LP light, a high-precision angle rotation stage to sweep the incidence angle, and a phase-sensitive amplifier to resolve the output signal. However, the use of such an SPR-enhanced ellipsometry system for chiral measurement has not been reported.

### 5.5 Summary

In this chapter we investigated the possibility of using surface plasmons to enhance the sensitivity of the differential ellipsometric method for measurement of both OR and CD chirality. We first studied the excitation and propagation of chiral SPPs at the interface between a metal and a chiral medium, and found that unlike conventional SPPs, chiral SP waves are hybrid in nature, meaning that they consist of both *s*- and *p*-polarizations. This hybrid nature gives rise to a cut-off condition which is highly dependent on the chiral strength of the chiral medium. In particular, we showed that the propagation length of chiral SPP is very sensitive to the chiral parameter near cut-off, which could potentially be exploited to perform chiral sensing on an integrated platform.

We also analyzed two multi-layer systems for exciting chiral SPPs, namely the Kretschmann and Otto systems, and investigated the sensitivity of the ellipsometric response of each system to both OR and CD chirality. We found that the LR-SPR (Otto) system provides better sensitivity to both types of chirality than the conventional Kretschmann SPR system, due to the higher quality factor of the LR-SPR mode and the stronger electric field existing at the chiral-metal interface. For a lossy chiral medium exhibiting CD chirality, simulation results showed that the LR-SPR system can provide one to two orders of magnitude enhancement in the ellipsometric angle

response when compared to ellipsometry based on reflection from a dielectric-chiral interface. We also performed preliminary experiments to study the feasibility of implementing the LR-SPR enhanced ellipsometric method in a commercial spectroscopic ellipsometer, and proposed potential solutions to overcome the SNR issue in future implementations of the method.

# Chapter Six.

# Conclusion

## 6.1 Summary and Contributions of Research

Optical sensing and measurement technology provides one of the most accurate tools for detecting and characterizing materials. Compared to other sensing technologies, they also offer the advantages of providing information more than the simple existence of the sample, such as optical properties, chemical composition and biological activities. In this thesis, we investigated novel optical sensing and measurement methods for two important applications, namely environmental greenhouse gas monitoring and chiral compound analysis for pharmaceutical and biochemical research.

With the alarming rate of increase in the atmospheric $CO_2$ concentration level, the world is facing a growing threat of irreversible climate change. Along with urgent actions to reduce greenhouse gas emission, there is a need for developing compact, accurate and low-cost solutions for greenhouse gas sensors that can be deployed in large-area sensor networks for environmental monitoring. Motivated by this, we have taken important steps in the first part of the thesis towards realizing an integrated silicon photonic gas sensing system on a chip that can perform parallel detection of greenhouse gases.

The second part of the thesis also aims to develop novel optical sensing technology, but focusing on a different type of applications. Here we explore the use of ellipsometry as a robust tool for measuring the optical rotation and circular dichroism of chiral compounds, exploiting especially the unique properties of chiral surface plasmon polaritons for enhancing the detection sensitivity of these methods. This research is motivated by the important role of chirality in

governing the biological functionalities of biochemical compounds. Measurement of chirality provides information about molecule conformation, enantiomeric purity or excess, and chiral compound concentrations, which are important in pharmaceutical research and other biomedical fields. The ellipsometric methods developed in this thesis could offer crucial advantages over existing techniques in terms of accuracy, small sample size and the ability to measure multiple optical quantities in the same setup.

Below we describe the key contributions in each part of the research.

*Development of silicon photonic multi-gas sensor system*

Although integrated photonic sensors have been widely employed for developing biosensors and are well known for their high sensitivity and compact size, their application to multi-gas sensing has rarely been reported, especially for $CO_2$ and other greenhouse gas detection. The challenge mainly resides in searching for a suitable functional material that can provide reversible optical response to the target gas without requiring special operating conditions such as high temperature and humidified environment. Our contributions to the development of a multi-gas sensor include the followings:

- We proposed and demonstrated the use of the polyhexamethylene biguanide (PHMB) polymer as a novel functional material for refractometric $CO_2$ gas sensing. PHMB has the advantage of reacting readily with $CO_2$ molecules without requiring catalysis by heat or humidity. We also showed that the polymer exhibits reversible refractive index change upon absorbing and releasing of $CO_2$ molecules. In addition, it can be easily deposited onto a silicon waveguide or other type optical waveguides simply by spin-coating. These features make PHMB an attractive functional material for developing refractometric $CO_2$ sensors.
- We demonstrated a compact silicon refractometric $CO_2$ sensor based on a microring resonator functionalized with the PHMB polymer. The sensor exhibited a linear response in terms of the resonance wavelength shift to the $CO_2$ gas concentration, with a sensitivity of $3.54\times10^{-3}$ pm/ppm over the 0 - 500ppm range of gas concentrations. It was also shown to have a detection limit of 20ppm, which is among the lowest LOD values reported for $CO_2$ sensors. To our knowledge, this is the first

integrated optics refractometric sensor that is capable of detecting $CO_2$ gas concentrations at the atmospheric level.

- We designed and implemented a silicon photonic dual-gas sensor for parallel detection of $CO_2$ and $H_2$ gases using a wavelength multiplexed microring array. One of the main contributions here is to develop a procedure for functionalizing the microring sensors with different types of functional materials, namely metal (Pd) and polymer (PHMB). We performed sensing experiments to evaluate the performance of the dual-gas sensor in the presence of multiple gases. In particular, we found that Pd, which is a commonly used functional material for $H_2$ sensing, has significant cross-sensitivity to $CO_2$ gas, a behaviour which has not been reported before. Nevertheless, by taking into account this cross-sensitivity, we showed that the dual-gas sensor could still be used to obtain accurate measurements of both $CO_2$ and $H_2$ gas concentrations. The dual-gas sensor system developed can be extended to include sensor elements for other greenhouse gases on the same chip.

We have published part of this work in the following journals and conferences:

- [148] Guangcan Mi, Cameron Horvath, Mirwais Aktary, and Vien Van, "Silicon microring refractometric sensor for atmospheric $CO_2$ gas monitoring," Optics Express, Vol. 24, No. 2, pp. 1773-80, 2016.
- [149] Guangcan Mi, Cameron Horvath, Mirwais Aktary, and Vien Van. "Compact silicon photonic refractometric sensor for atmospheric $CO_2$ gas monitoring," IEEE Photonics Conference 2015, pp. 619-620, 2015.

*Development of ellipsometric methods for chirality measurement*

Ellipsometry is a widely-used tool in both research and industry for measuring the refractive index, extinction coefficient and thickness of thin film materials. However, the use of the method for characterizing chiral compounds is much less reported. Our work contributed to the development of new ellipsometric techniques that could potentially provide a robust tool for chirality measurement in drug analysis and related biomedical research. The key contributions in this part of the research include the followings:

- We proposed and demonstrated a differential ellipsometric method for chirality measurement based on reflection from a dielectric-chiral interface at the critical angle

of incidence. By suppressing common noise sources and eliminating systematic errors related to the use of a reference sample, the method was shown to be robust enough that it could be implemented in a commercial ellipsometer, allowing broadband measurements of the chiral parameter without requiring expensive tunable laser sources and delicate setup.

- We showed that chiral SPPs supported by a chiral-metal interface have unique properties not found in conventional SPPs at an achiral-metal interface. In particular, chiral SPPs have a cut-off condition due to the coupling of TM and TE waves. As a result, it was found that the transmission loss of chiral SPPs near the cut-off is very sensitive to the chiral parameter, an effect which can potentially be exploited to realize integrated chiral sensors based on chiral plasmonic waveguides.
- We investigated the ellipsometric response of light reflected from chiral SPR multi-layer structures based on the Kretschmann and Otto configurations. We found that the excitation of chiral SPPs strongly enhances the ellipsometric signals in both cases, although the Otto SPR system provides a much stronger enhancement due to the large field at the chiral surface and the high quality factor of the excited LR-SPR mode. These results show that SPR-enhanced ellipsometry based on the Otto configuration can be used for accurate measurement of both the optical rotation and circular dichroism of chiral compounds.

We have published part of this work in the following journals and conferences:

- [150] Guangcan Mi and Vien Van, "Characteristics of surface plasmon polaritons at a chiral–metal interface," Optics Letters, Vol. 39, No. 7, pp. 2028-2031, 2014.
- [151] Guangcan Mi and Vien Van, “Chiral surface plasmon polaritons and their application for chirality detection,” in Photonics North 2014, SPIE: Montreal, Quebec, 2014.
- [152] Guangcan Mi and Vien Van, “A differential ellipsometric method for accurate chirality measurement” in IEEE Photonics Conference 2016, IEEE: Waikoloa, HI, 2016.
- [153] Guangcan Mi and Vien Van, "Surface plasmon resonance enhanced ellipsometric method for chirality detection," [in preparation].

## 6.2 Recommendation for Future Research Directions

### *6.2.1 Photonic multi-gas sensing system based on microring resonator arrays*

A research direction for the immediate future is to integrate more sensing channels for other target gases that are of interest for environmental monitoring. For example, methane is also a greenhouse gas that contributes to global warming. It is also an important source of clean [154] and has been employed in the industrial production of $H_2$. Another greenhouse gas is carbon monoxide, which is known to be toxic and dangerous and can be produced by many industrial processes as well as incomplete combustion of carbon-containing fuels. One of the key challenges in the incorporation of these gas sensors is to identify suitable functional materials that are compatible with each other and can provide sufficient selectivity to the target analytes. Considering these requirements, Metal Organic Frameworks (MOFs) could provide an array of promising functional materials for developing photonic multi-gas sensing systems. MOFs are highly porous materials synthesized by a wide selection of metal ions and organic ligands, providing advantages of structural diversity and configurable physical and chemical properties [155]. MOFs have been widely explored in recent years for gas separation and chemical sensing applications, exploiting the physical and chemical selectivity for various gases such as $CO_2$ [156], CO [157], $H_2S$ [158], $H_2$ [155], etc. Selective gas-permeable polymer membranes [159], could also be employed as an additional coating to enhance the selectivity of the sensing channel for the target gas.

From the system point of view, future work should also focus on increasing the degree of system integration in order to accommodate larger number of sensing channels, as well as provide signal conditioning, light source and detector on the same chip. To include more signal channels, multiple wavelength-multiplex sensor arrays could be built on a single chip that are spatially separated as shown in Figure 6.1. The arrays share the same input so that only one light source is required, while each array has a designated output and detector. This spatial division design is also convenient for employing various sensing mechanisms on the same chip, for example, by assigning a separate microring array to each sensing mechanism, since different sensing mechanisms can result in different types of output signal that may require separate operation and signal processing procedures. For example, in refractometric sensing and absorption spectroscopy, the dominant responses of a microring resonator are the shift of resonance wavelength and the

change in the spectrum shape respectively. These output signals require different fitting algorithms to extract the desired measurement results.

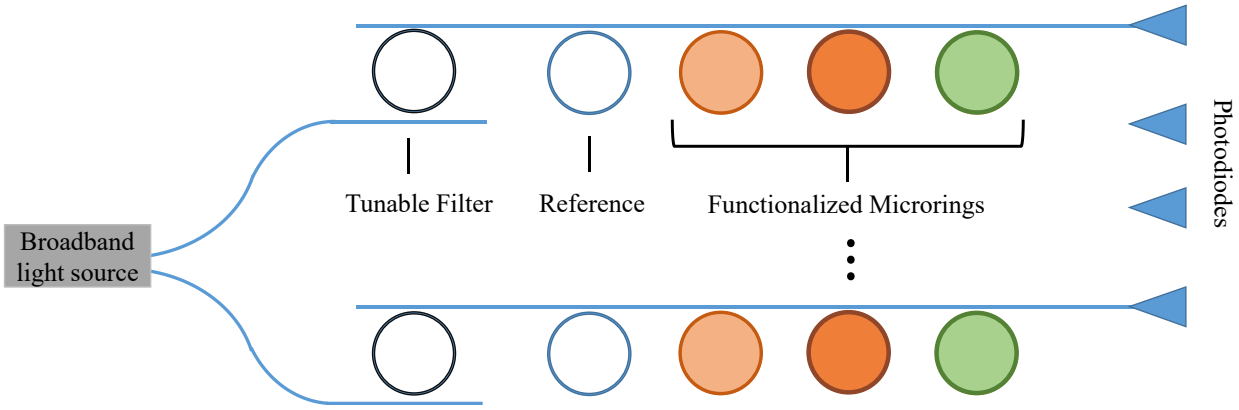


Figure 6.1. Schematic of multiplexed optical gas sensing system

To address the wavelength-multiplexed channels in each microring array, a tunable microring resonator filter could be integrated into each array for switching among signal channels in the array, with the output signal from the filter sent to the functionalized microrings. In this way the sensing system could employ a broadband light source such as superluminescent LEDs [160] and thin film photodiodes [161], both of which can be directly bonded and packaged onto the silicon photonic chip. This will further reduce the dimension and cost of the sensing system.

### *6.2.2 Surface plasmon enhanced ellipsometry for chiral measurement*

An extension of the work on SP-enhanced ellipsometric method for chirality detection is to construct an ellipsometry system using a laser source and high-resolution angle measurement capability, since a more intense light source could overcome the issue of weak SNR encountered in our attempt to implement the method in a commercial ellipsometer with a lamp source. Examples of such ellipsometric systems have been reported by some groups [145-147] for other applications such as metal thin film characterization.

An important direction in chiral measurement technology is to develop chirality detection techniques based on chiral SPPs on an integrated platform. We have shown that chirality influences the propagation loss of chiral SPPs, which can be determined by measuring the intensity of the transmitted light from a chiral plasmonic waveguide. Since the propagation loss is most sensitive to chirality when the chiral parameter approaches the cut-off value, the challenge is to construct a chiral plasmonic structure so that the cut-off chirality value occurs in the range of the

chiral strengths to be measured. We have also shown that enhanced chiral effect can be achieved from the strong electric field of LR-SPP in the Otto multi-layer structure. Such a structure can be realized on an integrated optic platform using the hybrid plasmonic waveguide structure described in [162], where the low-index buffer layer sandwiched between the metal and high-index core is replaced by the chiral layer. It will be interesting to investigate the influence of chirality to the hybrid plasmonic mode, which may be employed for chirality detection. Furthermore, owing to the small footprint of integrated photonic structures, plasmonic waveguides can be easily integrated with photonic sensors based on microring resonators on the same chip. This presents an attractive solution toward realizing a portable "optical characterization lab on a chip", which can provide multi-parameter analysis of micro-sized biochemical samples including refractometry, absorption spectroscopy, optical rotation and circular dichroism spectroscopy.

# Bibliography


1. M. P. Silverman, "Reflection and refraction at the surface of a chiral medium: comparison of gyrotropic constitutive relations invariant or noninvariant under a duality transformation," Journal of the Optical Society of America A, Vol. 3, No. 6, pp. 830-837, 1986.

2. E. U. Condon, "Theories of optical rotatory power," Reviews of Modern Physics, Vol. 9, No. 4, pp. 432-457, 1937.

3. M. Trojanowicz, "Enantioselective electrochemical sensors and biosensors: A mini-review," Electrochemistry Communications, Vol. 38, pp. 47-52, 2014.

4. S. M. Kelly, T. J. Jess, and N. C. Price, "How to study proteins by circular dichroism," Biochimica et Biophysica Acta, Vol. 1751, pp. 119-139, 2005.

5. A. L. Margolin, "Enzymes in the synthesis of chiral drugs," Enzyme and Microbial Technology, Vol. 15, No. 4, pp. 266-280, 1993.

6. J. H. W. G. d. Boer, G. M. W. Kroesen, and F. J. d. Hoog, "Spectroscopic rotating compensator ellipsometry in the infrared: retarder design and measurement," Measurement Science and Technology, Vol. 8, No. 5, pp. 484-492, 1997.

7. S.-G. Lim, S. Kriventsov, T. N. Jackson, J. H. Haeni, D. G. Schlom, A. M. Balbashov, R. Uecker, P. Reiche, J. L. Freeouf, and G. Lucovsky, "Dielectric functions and optical bandgaps of high-K dielectrics for metal-oxide-semiconductor field-effect transistors by far ultraviolet spectroscopic ellipsometry," Journal of Applied Physics, Vol. 91, No. 7, pp. 4500, 2002.

8. P. Nagpal, N. C. Lindquist, S. H. Oh, and D. J. Norris, "Ultrasmooth patterned metals for plasmonics and metamaterials," Science, Vol. 325, No. 5940, pp. 594-597, 2009.

9. H. Arwin, M. Poksinski, and K. Johansen, "Total internal reflection ellipsometry: Principles and applications," Applied Optics, Vol. 43, No. 15, pp. 3028, 2004.

10. D. van Noort, S. Welin-Klintström, H. Arwin, S. Zangooie, I. Lundström, and C.-F. Mandenius, "Monitoring specific interaction of low molecular weight biomolecules on oxidized porous silicon using ellipsometry," Biosensors and Bioelectronics, Vol. 13, No. 3-4, pp. 439-449, 1998.

11. P. Tans and R. Keeling. *Trends in atmospheric carbon dioxide*. [Online] Available from: www.esrl.noaa.gov/gmd/ccgg/trends/ [Accessed 2016.06].

12. F. M. Cox and A. A. C. J. Large1, "Liquid-filled hollow core microstructured polymer optical fiber," Optics Express, Vol. 14, No. 9, pp. 4135-4140, 2006.

13. J. H. Butler and S. A. Montzka. *The NOAA annual greenhouse gas index (AGGI)*. [Online] Available from: http://esrl.noaa.gov/gmd/aggi/aggi.html [Accessed 2016 06].

14. NOAA-ESRL Global Monitoring Division. *Full Mauna Loa $CO_2$ record and asnnual mean growth rate for Mauna Loa, Hawaii*. [Online] Available from: http://www.esrl.noaa.gov/gmd/ccgg/trends/gr.html [Accessed 2015 09].

15. Canadian Centre for Occupational Health and Safety (CCOHS). *Health effects of carbon dioxide gas. Summary of occupational risks, effects, and standards for $CO_2$*. [Online] Available from: www.ccohs.ca/oshanswers/. [Accessed 2016 06].

16. International Volcano Health Hazard News (IVHHN). *Volcanic gases and aerosols guidelines: Carbon dioxide* [Online] Available from: http://www.ivhhn.org/index.php?option=com_content&view=article&id=84 [Accessed 2016 06].

17. S. A. Rice, "Human health risk assessment of $CO_2$: Survivors of acute high-level exposure and populations sensitive to prolonged low-level exposure," Environments, Vol. 3, No. 5, pp. 7-15, 2014.

18. R. Prill, "Why measure carbon dioxide inside buildings". Publishded by W. 3, 2000.

19. L. B. Mendes, N. W. Ogink, N. Edouard, H. J. van Dooren, F. Tinoco Ide, and J. Mosquera, "NDIR gas sensor for spatial monitoring of carbon dioxide concentrations in naturally ventilated livestock buildings," Sensors (Basel), Vol. 15, No. 5, pp. 11239-11257, 2015.

20. J. Y. Wong and M. Schell, "Zero drift NDIR gas sensors," Sensor Review, Vol. 31, No. 1, pp. 70-77, 2011.

21. J. Hodgkinson, R. Smith, W. O. Ho, J. R. Saffell, and R. P. Tatam, "Non-dispersive infra-red (NDIR) measurement of carbon dioxide at 4.2μm in a compact and optically efficient sensor," Sensors and Actuators B: Chemical, Vol. 186, pp. 580-588, 2013.

22. D. Gibson and C. MacGregor, "A novel solid state non-dispersive infrared $CO_2$ gas sensor compatible with wireless and portable Deployment," Sensors, Vol. 13, No. 6, pp. 7079-7103, 2013.

23. A. Prim, E. Pellicer, E. Rossinyol, F. Peiró, A. Cornet, and J. R. Morante, "A novel mesoporous CaO-Loaded $In_2O_3$ Material for $CO_2$ sensing," Advanced Functional Materials, Vol. 17, No. 15, pp. 2957-2963, 2007.

24. N. Miura, S. Yao, Y. Shimizu, and N. Yamazoe, "Carbon dioxide sensor using sodium ion conductor and binary carbonate auxiliary electrode," Journal of the Electrochemical Society, Vol. 139, No. 5, pp. 1384-1388, 1992.

25. T. Yoshioka, N. Mizuno, and M. Iwamoto, "$La_2O_3$-loaded $SnO_2$ element as a $CO_2$ gas sensor," Chemistry Letters, Vol. 7, pp. 1249-1252, 1991.

26. S. Akbar, P. Dutta, and C. Lee, "High-temperature ceramic gas sensors: A review," International Journal of Applied Ceramic Technology, Vol. 3, No. 4, pp. 302-311, 2006.

27. M. Cajlakovic, A. Bizzarria, M. Suppana, C. Konrada, and V. Ribitscha, "Continuous monitoring of pO2 and pCO2 by microdialysis indicates physiologic status of the critically ill patients," Sensors and Actuators B: Chemical, Vol. 139, No. 1, pp. 181-186, 2009.

28. P. Puligundla, J. Jung, and S. Ko, "Carbon dioxide sensors for intelligent food packaging applications," Food Control, Vol. 25, No. 1, pp. 328-333, 2012.

29. Z. Xia, A. A. Eftekhar, Q. Li, and A. Adibi. "On-chip multiplexed photonic gas sensing for the detection of volatile organic compounds," IEEE Photonics Conference 2012, IEEE, pp. 548-549, 2012.

30. N. A. Yebo, S. P. Sree, E. Levrau, C. Detavernier, Z. Hens, J. A. Martens, and R. Baets, "Selective and reversible ammonia gas detection with nanoporous film functionalized silicon photonic micro-ring resonator," Optics Express, Vol. 20, No. 11, pp. 11855–11862, 2012.

31. N. A. Yebo, P. Lommens, Z. Hens, and R. Baets, "An integrated optic ethanol vapor sensor based on a silicon-on-insulator microring resonator coated with a porous ZnO film," Optics Express, Vol. 18, No. 11, pp. 11859-11866, 2010.

32. J. T. Robinson, L. Chen, and M. Lipson, "On-chip gas detection in silicon optical microcavities," Optics Express, Vol. 16, No. 6, pp. 4296–4301, 2008.

33. A. Yalcın, K. C. Popat, J. C. Aldridge, T. A. Desai, J. Hryniewicz, N. Chbouki, B. E. Little, O. King, V. Van, S. Chu, D. Gill, M. Anthes-Washburn, and M. S. Unlu, "Optical sensing of biomolecules using microring resonators," IEEE Journal of Selected Topics in Quantum Electronics, Vol. 12, No. 1, pp. 148-155, 2006.

34. I. M. White and X. Fan, "On the performance quantification of resonant refractive index Sensors," Optics Express, Vol. 16, No. 2, pp. 1020-1028, 2008.

35. B. N. Shivananju, S. Yamdagni, R. Fazuldeen, A. K. Sarin Kumar, G. M. Hegde, M. M. Varma, and S. Asokan, "$CO_2$ sensing at room temperature using carbon nanotubes coated core fiber Bragg grating," Review of Scientific Instruments, Vol. 84, No. 6, pp. 065002, 2013.

36. T. Lang, T. Hirsch, C. Fenzl, F. Brandl, and O. S. Wolfbeis, "Surface plasmon resonance sensor for dissolved and gaseous carbon dioxide," Analytical Chemistry, Vol. 84, No. 21, pp. 9085-9088, 2012.

37. K. B. Sentell and E. Beaullieu, "Comparison of preservative uptake and release profiles of PHMB from soft contact lens care products by silicone hydrogel contact lenses," Investigative Ophthalmology & Visual Science, Vol. 45, No. 5, pp., 2004.

38. S. Satyapal, T. Filburn, J. Trela, and J. Strange, "Performance and properties of a solid amine sorbent for carbon dioxide removal in space life support applications," Energy & Fuels, Vol. 15, No. 2, pp. 250-255, 2001.

39. F. S. Pereira, E. R. deAzevedo, E. F. da Silva, T. J. Bonagamba, D. L. da Silva Agostíni, A. Magalhães, A. E. Job, and E. R. Pérez González, "Study of the carbon dioxide chemical fixation—activation by guanidines," Tetrahedron, Vol. 64, No. 43, pp. 10097-10106, 2008.

40. H. J. Lee, K. K. Park, M. Kupnik, and B. T. Khuri-Yakub, "Functionalization layers for $CO_2$ sensing using capacitive micromachined ultrasonic transducers," Sensors and Actuators B: Chemical, Vol. 174, pp. 87-93, 2012.

41. M. Born and E. Wolf, *Principles of optics: electromagnetic theory of propagation, interference and diffraction of light*. CUP Archive, 2000.

42. Q. Li, T. Wang, Y. Su, M. Yan, and M. Qiu, "Coupled mode theory analysis of mode-splitting in coupled cavity system," Optics Express, Vol. 18, No. 8, pp. 8367-8382, 2010.

43. B. E. Little, J. Laine, and S. T. Chu, "Surface-roughness-induced contradirectional coupling in ring and disk resonators," Optics Express, Vol. 22, No. 1, pp. 4-6, 1997.

44. Scientific Committee on Consumer Safety, "Opinion of the scientific committee on consumer safety (SCCS) – 2nd Revision of the safety of the use of poly(hexamethylene) biguanide hydrochloride or polyaminopropyl biguanide (PHMB) in cosmetic products," Regulatory Toxicology and Pharmacology, Vol. 73, No. 3, pp. 885-886, 2015.

45. G. F. Fine, L. M. Cavanagh, A. Afonja, and R. Binions, "Metal oxide semi-conductor gas sensors in environmental monitoring," Sensors (Basel), Vol. 10, No. 6, pp. 5469-5502, 2010.

46. T. Allsop, R. Arif, R. Neal, K. Kalli, V. Kundrát, A. Rozhin, P. Culverhouse, and D. J. Webb, "Photonic gas sensors exploiting directly the optical properties of hybrid carbon nanotube localized surface plasmon structures," Light: Science & Applications, Vol. 5, No. 2, pp. e16036, 2016.

47. C. Gouveia, A. Markovics, J. M. Baptista, B. Kovacs, and P. A. S. Jorge. "Measurement of $CO_2$ using refractometric fiber optic sensors," Proceedings of the 3rd WSEAS International Conference on Advances in Sensors, Signals and Materials, Stevens Point, WI, pp. 169-173, 2010.

48. J. Zou and W. S. W. Ho, "$CO_2$-selective polymeric membranes containing amines in crosslinked poly(vinyl alcohol)," Journal of Membrane Science, Vol. 286, No. 1-2, pp. 310-321, 2006.

49. Radiant Innovation Inc. *ZG1683RU 3 IN 1 $CO_2$ Monitor ($CO_2$ + Temp. + RH) Operating Instructions* [Online] Available from: http://www.zyaura.com/support/support_Manual.htm [Accessed 2010 06].

50. M. I. Cheema, U. A. Khan, A. M. Armani, and A. G. Kirk, "Towards more accurate microcavity sensors: maximum likelihood estimation applied to a combination of quality factor and wavelength shifts," Optics Express, Vol. 21, No. 19, pp. 22817-22828 2013.

51. L. Zhang, Z. Hu, and J. Jiang, "Metal–organic framework/polymer mixed-matrix membranes for $H_2/CO_2$ separation: A fully atomistic simulation study," The Journal of Physical Chemistry C, Vol. 116, No. 36, pp. 19268-19277, 2012.

52. C. Rameshan, W. Stadlmayr, C. Weilach, S. Penner, H. Lorenz, M. Hävecker, R. Blume, T. Rocha, D. Teschner, G. A. Knop, and R. Schlög, "Subsurface-controlled $CO_2$ selectivity of PdZn near-surface alloys in $H_2$ generation by methanol steam reforming," Angewandte Chemie International Edition, Vol. 49, No. 18, pp. 3224-3227, 2010.

53. S. Y. Yang, J. A. DeFranco, Y. A. Sylvester, T. J. Gobert, D. J. Macaya, R. M. Owens, and G. G. Malliaras, "Integration of a surface-directed microfluidic system with an organic electrochemical transistor array for multi-analyte biosensors," Lab Chip, Vol. 9, pp. 704-708, 2009.

54. J. I. Hong and B. Chang, "Development of the smartphone-based colorimetry for multi-analyte sensing arrays," Lab Chip, Vol. 14, pp. 1725-1732, 2014.

55. X. Zhang, S. Rehm, M. M. Safont-Sempere, and F. Würthner, "Vesicular perylene dye nanocapsules as supramolecular fluorescent pH sensor systems," Nature chemistry, Vol. 1, No. 8, pp. 623-629, 2009.

56. C. C. You, O. R. Miranda, B. Gider, P. S. Ghosh, B. I. Kim, B. Erdogan, S. A. Krovi, U. H. Bunz, and V. M. Rotello, "Detection and identification of proteins using nanoparticle-fluorescent polymer 'chemical nose'sensors," Nature Nanotechnology, Vol. 2, No. 5, pp. 318-323, 2007.

57. K. De Vos, I. Bartolozzi, E. Schacht, P. Bienstman, and R. Baets, "Silicon-on-insulator microring resonator for sensitive and label-free biosensing," Optics Express, Vol. 15, No. 12, pp. 7610-7615, 2007.

58. C. F. Carlborg, K. B. Gylfason, A. Kazmierczak, F. Dortu, M. J. Banuls Polo, A. Maquieira Catala, G. M. Kresbach, H. Sohlstrom, T. Moh, L. Vivien, J. Popplewell, G. Ronan, C. A. Barrios, G. Stemme, and W. van der Wijngaart, "A packaged optical slot-waveguide ring resonator sensor array for multiplex label-free assays in labs-on-chips," Lab Chip, Vol. 10, No. 3, pp. 281-290, 2010.

59. M. Iqbal, M. A. Gleeson, B. Spaugh, F. Tybor, W. G. Gunn, M. Hochberg, T. Baehr-Jones, R. C. Bailey, and L. C. Gunn, "Label-free biosensor arrays based on silicon ring resonators and high-speed optical scanning instrumentation," IEEE Journal of Selected Topics in Quantum Electronics, Vol. 16, No. 3, pp. 654-661, 2010.

60. D. X. Xu, A. Densmore, A. Delâge, P. Waldron, R. McKinnon, S. Janz, J. Lapointe, G. Lopinski, T. Mischki, E. Post, P. Cheben, and J. H. Schmid, "Folded cavity SOI microring sensors for high sensitivity and real time measurement of biomolecular binding," Optics Express, Vol. 16, No. 19, pp. 15137-15148, 2008.

61. C. Chung-Yen and L. J. Guo, "Design and optimization of microring resonators in biochemical sensing applications," Journal of Lightwave Technology, Vol. 24, No. 3, pp. 1395-1402, 2006.

62. J. T. Kirk, G. E. Fridley, J. W. Chamberlain, E. D. Christensen, M. Hochberg, and D. M. Ratner, "Multiplexed inkjet functionalization of silicon photonic biosensors," Lab Chip, Vol. 11, No. 7, pp. 1372-1377, 2011.

63. A. Sridhar, T. Blaudeck, and R. R. Baumann, "Inkjet printing as a key enabling technology for printed electronics," Material Matters, Vol. 6, No. 1, pp. 12-15, 2011.

64. B. Derby, "Inkjet printing of functional and structural materials: Fluid property requirements, feature stability, and rsesolution," Annual Review of Materials Research, Vol. 40, No. 1, pp. 395-414, 2010.

65. D. X. Xu, M. Vachon, A. Densmore, R. Ma, A. Delage, S. Janz, J. Lapointe, Y. Li, G. Lopinski, D. Zhang, Q. Y. Liu, P. Cheben, and J. H. Schmid, "Label-free biosensor array based on silicon-on-insulator ring resonators addressed using a WDM approach," Optics Letters, Vol. 35, No. 16, pp. 2771-2773, 2010.

66. K. De Vos, J. Girones, T. Claes, Y. De Koninck, S. Popelka, E. Schacht, R. Baets, and P. Bienstman, "Multiplexed antibody detection with an array of silicon-on-insulator microring resonators," IEEE Photonics Journal, Vol. 1, No. 4, pp. 225-235, 2009.

67. R. R. J. Maier, B. J. S. Jones, J. S. Barton, S. McCulloch, T. Allsop, J. D. C. Jones, and I. Bennion, "Fibre optics in palladium-based hydrogen sensing," Journal of Optics A: Pure and Applied Optics, Vol. 9, No. 6, pp. S45-S59, 2007.

68. C. Edwards, S. J. McKeown, J. Zhou, G. Popescu, and L. L. Goddard, "In situ measurements of the axial expansion of palladium microdisks during hydrogen exposure using diffraction phase microscopy," Optical Materials Express, Vol. 4, No. 12, pp. 2559, 2014.

69. N. Carriere, M. Z. Alam, M. Mojahedi, and J. S. Aitchison, "An integrated optical hydrogen sensor on a silicon-on-insulator platform: Effects of palladium film thickness," Sensors and Actuators B: Chemical, Vol. 216, pp. 6-10, 2015.

70. M. Eryürek, Y. Karadag, N. Taşaltın, N. Kılınç, and A. Kiraz, "Optical sensor for hydrogen gas based on a palladium-coated polymer microresonator," Sensors and Actuators B: Chemical, Vol. 212, pp. 78-83, 2015.

71. C. Peng and W. A. Challener, "Input-grating couplers for narrow Gaussian beam: influence of groove depth," Optics Express, Vol. 12, No. 26, pp. 6481-6490, 2004.

72. D. Taillaert, F. Van Laere, M. Ayre, W. Bogaerts, D. Van Thourhout, and P. Bienstman, "Grating couplers for coupling between optical fibers and nanophotonic waveguides," Japanese Journal of Applied Physics, Vol. 45, No. 8R, pp. 6071.

73. Y. Wang, X. Wang, J. Flueckiger, H. Yun, W. Shi, R. Bojko, N. A. Jaeger, and L. Chrostowski, "Focusing sub-wavelength grating couplers with low back reflections for rapid prototyping of silicon photonic circuits," Optics Express, Vol. 22, No. 17, pp. 20652-20662, 2014.

74. R. Waldhäusl, B. Schnabel, P. Dannberg, E. B. Kley, A. Bräuer, and W. Karthe, "Efficient coupling into polymer waveguides by gratings," Applied Optics, Vol. 36, No. 36, pp. 9383-9390, 1997.

75. F. Van Laere, T. Claes, J. Schrauwen, S. Scheerlinck, W. Bogaerts, D. Taillaert, L. O'Faolain, D. Van Thourhout, and R. Baets, "Compact Focusing Grating Couplers for Silicon-on-Insulator Integrated Circuits," IEEE Photonics Technology Letters, Vol. 19, No. 23, pp. 1919-1921, 2007.

76. T. Hübert, L. Boon-Brett, G. Black, and U. Banach, "Hydrogen sensors - a review," Sensors and Actuators B: Chemical, Vol. 157, No. 2, pp. 329-352, 2011.

77. S. K. Arya, S. Krishnan, H. Silva, S. Jean, and S. Bhansali, "Advances in materials for room temperature hydrogen sensors," Analyst, Vol. 137, No. 12, pp. 2743-2756, 2012.

78. M. Z. Alam, N. Carriere, F. Bahrami, M. Mojahedi, and J. S. Aitchison, "Pd-based integrated optical hydrogen sensor on a silicon-on-insulator platform," Optics Letters, Vol. 38, No. 9, pp. 1428-1430, 2013.

79. A. D. Rakić, A. B. Djurišić, J. M. Elazar, and M. L. Majewski, "Optical properties of metallic films for vertical-cavity optoelectronic devices," Applied Optics, Vol. 37, No. 22, pp. 5271-5283, 1998.

80. D. L. Olynick, B. Cord, A. Schipotinin, D. F. Ogletree, and P. J. Schuck, "Electron-beam exposure mechanisms in hydrogen silsesquioxane investigated by vibrational spectroscopy and in situ electron-beam-induced desorption," Journal of Vacuum Science & Technology B: Microelectronics and Nanometer Structures, Vol. 28, No. 3, pp. 581, 2010.

81. S. Choi, M. J. Word, V. Kumar, and I. Adesida, "Comparative study of thermally cured and electron-beam-exposed hydrogen silsesquioxane resists," Journal of Vacuum Science & Technology B: Microelectronics and Nanometer Structures, Vol. 26, No. 5, pp. 1654, 2008.

82. P. V. McKinney, "The adsorption of gases on palladium oxide," Journal of the American Chemical Society, Vol. 55, No. 9, pp. 3626-3632, 1933.

83. G. T. Reed and A. P. Knights, *Silicon Photonics : An Introduction*. West Sussex, England: John Wiley and Sons, 2004.

84. E. Lee, J. M. Lee, E. Lee, J. Noh, J. H. Joe, B. Jung, and W. Lee, "Hydrogen gas sensing performance of Pd–Ni alloy thin films," Thin Solid Films, Vol. 519, pp. 880-884, 2010.

85. P. Ball. Nature News. *A handle on handedness*. [Online] Available from: http://www.nature.com/news/2000/000622/full/news000622-10.html [Accessed 2014 04].

86. C. Decarvalho and M. Dafonseca, "Carvone: Why and how should one bother to produce this terpene," Food Chemistry, Vol. 95, No. 3, pp. 413-422, 2006.

87. L. A. Nguyen, H. He, and C. Pham-Huy, "Chiral drugs: An overview," International Journal of Biomedical Science, Vol. 2, No. 2, pp. 85-100, 2006.

88. K. M. Rentsch, "The importance of stereoselective determination of drugs in the clinical laboratory," Journal of Biochemical and Biophysical Methods, Vol. 54, No. 1-3, pp. 1-9, 2002.

89. J. Lin and D. Su, "A new method for measuring the chiral parameter and the average refractive index of a chiral liquid," Optics Communications, Vol. 218, No. 4-6, pp. 317-323, 2003.

90. D. Sofikitis, L. Bougas, G. E. Katsoprinakis, A. K. Spiliotis, B. Loppinet, and T. P. Rakitzis, "Evanescent-wave and ambient chiral sensing by signal-reversing cavity ringdown polarimetry," Nature, Vol. 514, No. 7520, pp. 76-79, 2014.

91. B. M. Maoz, Y. Chaikin, A. B. Tesler, O. B. Elli, Z. Fan, A. O. Govorov, and G. Markovich, "Amplification of chiroptical activity of chiral biomolecules by surface plasmons," Nano Letters, Vol. 13, No. 3, pp. 1203-1209, 2013.

92. W. Yan, L. Xu, W. Ma, L. Liu, L. Wang, H. Kuang, and C. Xu, "Pyramidal sensor platform with reversible chiroptical signals for DNA detection," Small, Vol. 10, No. 21, pp. 4293-4297, 2014.

93. F. Vollmer and P. Fischer, "Ring-resonator-based frequency-domain optical activity measurements of a chiral liquid," Optics Letters, Vol. 31, No. 4, pp. 453-455, 2006.

94. S. Abbate, E. Castiglioni, F. Gangemi, R. Gangemi, and G. Longhi, "NIR - VCD, vibrational circular dichroism in the near-infrared: Experiments, theory and calculations," Chirality, Vol. 21, No. 1E, pp. E242 - E252, 2009.

95. B. Kieser, C. Fietzek, R. Schmidt, G. Belge, U. Weimar, V. Schurig, and G. Gauglitz, "Use of a modified cyclodextrin host for the enantioselective detection of a halogenated diether as chiral guest via optical and electrical transducers," Analytical Chemistry, Vol. 74, No. 13, pp. 3005-3012, 2002.

96. K. Haupt, K. Noworyta, and W. Kutner, "Imprinted polymer-based enantioselective acoustic sensor using a quartz crystal microbalance," Analytical Communications, Vol. 36, No. 11-12, pp. 391, 1999.

97. M. M. Wanderley, C. Wang, C. D. Wu, and W. Lin, "A chiral porous metal-organic framework for highly sensitive and enantioselective fluorescence sensing of amino alcohols," Journal of the American Chemical Society, Vol. 134, No. 22, pp. 9050-9053, 2012.

98. X. Yin, J. Ding, S. Zhang, and J. Kong, "Enantioselective sensing of chiral amino acids by potentiometric sensors based on optical active polyaniline films," Biosensors and Bioelectronics, Vol. 21, No. 11, pp. 2184-2187, 2006.

99. S. Bassiri, C. H. Papas, and N. Engheta, "Electromagnetic wave propagation through a dielectric-chiral interface and through a chiral slab," Journal of the Optical Society of America A, Vol. 5, No. 9, pp. 1450-1459, 1989.

100. D. L. Jaggard and X. Sun, "Theory of chiral multilayers," Journal of the Optical Society of America A, Vol. 9, No. 5, pp. 804-813, 1992.

101. E. Georgieva, "Reflection and refraction at the surface of an isotropic chiral medium: eigenvalue–eigenvector solution using a 4 × 4 matrix method," Journal of the Optical Society of America A, Vol. 12, No. 10, pp. 2203-2212, 1995.

102. A. I. Lvovsky, "Fresnel Equations," in *Encyclopedia of Optical Engineering*. 2013, New York: Taylor and Francis. pp. 1-6.

103. Sigma-Aldrich Inc. *Sucrose. MSDS S8501.* . [Online] Available from: http://www.sigmaaldrich.com/catalog/product/sigma/s8501?lang=en&region=CA [Accessed 2016 04].

104. "Concentrative Properties of Aqueous Solutions: Density, Refractive Index, Freezing Point Depression, and Viscosity," in *CRC Handbook of Chemistry and Physics*, W.M. Haynes, Editor. 2014-2015, Boca Raton, FL: CRC Press. pp. 145.

105. M. P. Silverman and J. Badoz, "Large enhancement of chiral asymmetry in light reflection near critical angle," Optics Communications, Vol. 74, No. 3-4, pp. 129-133, 1989.

106. M. P. Silverman, N. Ritchie, G. M. Cushman, and B. Fisher, "Experimental configurations using optical phase modulation to measure chiral asymmetries in light specularly reflected from a naturally gyrotropic medium," Journal of the Optical Society of America A, Vol. 5, No. 11, pp. 1852-1862, 1988.

107. M. P. Silverman, "Differential amplification of circularly polarised light by enhanced internal reflection from an active chiral medium," Optics Communications, Vol. 74, No. 3-4, pp. 134-138, 1989.

108. M. P. Silverman and J. Badoz, "Interferometric enhancement of chiral asymmetries: ellipsometry with an optically active Fabry–Perot interferometer," Journal of the Optical Society of America A, Vol. 11, No. 6, pp. 1894-1917, 1994.

109. J. A. Woollam Co. Inc, *M-2000® Specifications*. Lincoln, NE, 2007.

110. J. A. Woollam Co. Inc, *Getting to use WVASE32®*. Lincoln, NE, 2010.

111. H. G. Tompkins and E. A. Irene, *Handbook of ellipsometry*, H.G. Tompkins and E.A. Irene, Editors.: William Andrew. pp. 3-91, 2005.

112. Y. F. Chao, C. S. Wei, and W. C. Lee. "Polarizer-sample-analyzer intensity quotient ellipsometry," U.S. Patent 5 706 088, Jan 06, 1998.

113. Therapeutic Products Programme Health Canada. *Guidance for Industry: Stereochemical Issues in Chiral Drug Development*. [Online] Available from: http://www.hc-sc.gc.ca/dhp-mps/prodpharma/applic-demande/guide-ld/chem/stereo-eng.php [Accessed 2016 06].

114. B. D. Johs and D. W. Thompson. "Regression calibrated spectroscopic rotating compensator ellipsometer system with photo array detector," U.S. Patent 5 872 630, Feb 16, 1999.

115. S. E. Green, C. M. Herzinger, B. D. Johs, and J. A. Woollam. "System and method for improving data acquisition capability in spectroscopic ellipsometers," U.S. Patent 5 757 494, May 26, 1998.

116. P. S. Hauge, "Generalized rotating-compensator ellipsometry," Surface Science, Vol. 56, pp. 148-160, 1976.

117. "Physical constants of organic compounds," in *CRC Handbook of Chemistry and Physics*, W.M. Haynes, Editor. 2014-2015, Boca Raton, FL: CRC Press. pp. 137.

118. R. N. Compton, S. M. Mahurin, and R. N. Zare, "Demonstration of optical rotatory dispersion of sucrose," Journal of Chemical Education, Vol. 76, No. 9, pp. 1234, 1999.

119. T. M. Lowry and E. M. Richards, "The rotatory dispersive power of organic compounds. Part XIII. The significance of simple rotatory dispersion. Rotatory dispersion of camphorquinone and of sucrose," Journal of the Chemical Society, Transactions, Vol. 125, pp. 2511-2524, 1924.

120. J. Homola, S. S. Yee, and G. Gauglitz, "Surface plasmon resonance sensors: review," Sensors and Actuators B: Chemical, Vol. 54, No. 1-2, pp. 3-15, 1999.

121. T. Liebermann and W. Knoll, "Surface-plasmon field-enhanced fluorescence spectroscopy," Colloids and Surfaces A: Physicochemical and Engineering Aspects, Vol. 171, No. 1-3, pp. 115-130, 2000.

122. M. Osawa, "Dynamic processes in electrochemical reactions studied by surface-enhanced infrared absorption spectroscopy (SEIRAS)," Bulletin of the Chemical Society of Japan, Vol. 70, No. 12, pp. 2861-2880, 1997.

123. X. Qian, X. H. Peng, D. O. Ansari, Q. Yin-Goen, G. Z. Chen, D. M. Shin, L. Yang, A. N. Young, M. D. Wang, and S. Nie, "In vivo tumor targeting and spectroscopic detection with surface-enhanced Raman nanoparticle tags," Nature Biotechnology, Vol. 26, No. 1, pp. 83-90, 2008.

124. I. Lieberman, G. Shemer, T. Fried, E. M. Kosower, and G. Markovich, "Plasmon-resonance-enhanced absorption and circular dichroism," Angewandte Chemie International Edition, Vol. 47, No. 26, pp. 4855-4857, 2008.

125. P. Pelet, "The theory of chirowaveguides," IEEE Transactions on Antennas and Propagation, Vol. 38, No. 1, pp. 90-98, 1990.

126. M. G. Blaber, M. D. Arnold, and M. J. Ford, "Search for the ideal plasmonic nanoshell: the effects of surface scattering and alternatives to gold and silver," The Journal of Physical Chemistry, Vol. 113, No. 8, pp. 3041-3045, 2009.

127. S. J. Orfanidis, "Multilayer structures," in *Electromagnetic Waves and Antenna*. 2016, New Brunswick, NJ: Rutgers University. pp. 186-240.

128. P. Berini, "Long-range surface plasmon polaritons," Advances in Optics and Photonics, Vol. 1, No. 3, pp. 484, 2009.

129. V. Chabot, Y. Miron, M. Grandbois, and P. G. Charette, "Long range surface plasmon resonance for increased sensitivity in living cell biosensing through greater probing depth," Sensors and Actuators B: Chemical, Vol. 174, pp. 94-101, 2012.

130. S. Isaacs and I. Abdulhalim, "Long range surface plasmon resonance with ultra-high penetration depth for self-referenced sensing and ultra-low detection limit using diverging beam approach," Applied Physics Letters, Vol. 106, No. 19, pp. 193701, 2015.

131. T. Iwata and Y. Mizutani, "Ellipsometric measurement technique for a modified Otto configuration used for observing surface-plasmon resonance," Optics Express, Vol. 18, No. 14, pp. 14480-14487, 2010.

132. Applied Photophysics. *Units of CD Measurement*. [Online] Available from: https://www.photophysics.com/resources/7-cd-units-conversions [Accessed 2015 09].

133. A. O. Govorov, Z. Fan, P. Hernandez, J. M. Slocik, and R. R. Naik, "Theory of circular dichroism of nanomaterials comprising chiral molecules and nanocrystals: plasmon enhancement, dipole interactions, and dielectric effects," Nano Letters, Vol. 10, No. 4, pp. 1374-1382, 2010.

134. M. Iga, A. Seki, and K. Watanabe, "Hetero-core structured fiber optic surface plasmon resonance sensor with silver film," Sensors and Actuators B: Chemical, Vol. 101, No. 3, pp. 368-372, 2004.

135. K. Diest, V. Liberman, D. M. Lennon, P. B. Welander, and M. Rothschild, "Aluminum plasmonics: Optimization of plasmonic properties using liquid-prism-coupled ellipsometry," Optics Express, Vol. 21, No. 23, pp. 28638-28650, 2013.

136. P. R. West, S. Ishii, G. V. Naik, N. K. Emani, V. M. Shalaev, and A. Boltasseva, "Searching for better plasmonic materials," Laser & Photonics Reviews, Vol. 4, No. 6, pp. 795-808, 2010.

137. S. K. Jha, Z. Ahmed, M. Agio, Y. Ekinci, and J. F. Loffler, "Deep-UV surface-enhanced resonance Raman scattering of adenine on aluminum nanoparticle arrays," Journal of the American Chemical Society, Vol. 134, No. 4, pp. 1966-1969, 2012.

138. A. Ono, M. Kikawada, R. Akimoto, W. Inami, and Y. Kawata, "Fluorescence enhancement with deep-ultraviolet surface plasmon excitation," Optics Express, Vol. 21, No. 15, pp. 17447-17453, 2013.

139. X.-f. Pan, W.-d. Tao, F.-b. Yan, and G.-r. Bai, "Fabrication of PMMA doped with griseofulvin material and its optical rotatory dispersion,″ Optoelectronics Letters, Vol. 2, No. 1, pp. 41-43, 2006.

140. B. D. Johs, J. A. Woollam, C. M. Herzinger, J. N. Hilfiker, R. A. Synowicki, and C. L. Bungay. "Overview of variable-angle spectroscopic ellipsometry (VASE): II. Advanced applications,″ Optical Metrology, pp. 29-58, 1999.

141. H. Fujiwara, "Depolarization Effect of Samples," in *Spectroscopic ellipsometry: principles and applications*. 2007, West Sussex, England: John Wiley & Sons. pp. 139-141.

142. K. Bordo and H.-G. Rubahn, "Effect of Deposition Rate on Structure and Surface Morphology of Thin Evaporated Al Films on Dielectrics and Semiconductors,″ Materials Science, Vol. 18, No. 4, pp. 313-317, 2012.

143. Y. J. Lee and S.-W. Kang, "Atomic Layer Deposition of Aluminum Thin Films Using an Alternating Supply of Trimethylaluminum and a Hydrogen Plasma,″ Electrochemical and Solid-State Letters, Vol. 5, No. 10, pp. C91, 2002.

144. E. Luber, R. Mohammadi, C. Ophus, Z. Lee, N. Nelson-Fitzpatrick, K. Westra, S. Evoy, U. Dahmen, V. Radmilovic, and D. Mitlin, "Tailoring the microstructure and surface morphology of metal thin films for nano-electro-mechanical systems applications,″ Nanotechnology, Vol. 19, No. 12, pp. 125705, 2008.

145. M. S. Islam, H. M. Cho, A. K. Dutta, W. Chegal, Y. J. Cho, Y.-p. Kim, and H.-s. Kim. "Enhancement of biomolecular detection sensitivity by surface plasmon resonance ellipsometry,″ Optics East 2005, International Society for Optics and Photonics, pp. 60081F, 2005.

146. B. Ramanujam, "Incorporation of achromatic compensator into a dual rotating compensator multichannel ellipsometer " M.S. thesis, Electrical Engineering University of Toledo, Toledo, OH, 2012.

147. A. Furchner, G. Sun, H. Ketelsen, J. Rappich, and K. Hinrichs, "Fast IR laser mapping ellipsometry for the study of functional organic thin films,″ Analyst, Vol. 140, No. 6, pp. 1791-1797, 2015.

148. G. Mi, C. Horvath, M. Aktary, and V. Van. "Compact silicon photonic refractometric sensor for atmospheric CO2 gas monitoring,″ IEEE Photonics Conference 2015, Reston, VI, IEEE, pp. 619-620, 2015.

149. G. Mi, C. Horvath, M. Aktary, and V. Van, "Silicon microring refractometric sensor for atmospheric $CO_2$ gas monitoring,″ Optics Express, Vol. 24, No. 2, pp. 1773-1780, 2016.

150. G. Mi and V. Van, "Characteristics of surface plasmon polaritons at a chiral–metal interface,″ Optics Letters, Vol. 39, No. 7, pp. 2028-2031, 2014.

151. G. Mi and V. Van. "Chiral surface plasmon polaritons and their application for chirality detection ″ Photonics North 2014, Montreal, Quebec, SPIE, 2014.

152. G. Mi and V. Van. "A differential ellipsometric method for accurate chirality measurement ″ IEEE Photonics Conference 2016, Waikoloa, HI, IEEE, 2016.

153. G. Mi and V. Van, "Surface Plasmon Resonance Enhanced Ellipsometric Method for Chirality Detection,″ [*in preparation*].

154. D. P. Chynoweth, J. M. Owens, and R. Legrand, "Renewable methane from anaerobic digestion of biomass,″ Renewable Energy, Vol. 22, No. 1-3, pp. 1-8, 2001.

155. L. E. Kreno, K. Leong, O. K. Farha, M. Allendorf, R. P. Van Duyne, and J. T. Hupp, "Metal-organic framework materials as chemical sensors,″ Chemical Reviews, Vol. 112, No. 2, pp. 1105-1125, 2012.

156. J. J. Gassensmith, J. Y. Kim, J. M. Holcroft, O. K. Farha, J. F. Stoddart, J. T. Hupp, and N. C. Jeong, "A metal-organic framework-based material for electrochemical sensing of carbon dioxide," Journal of the American Chemical Society, Vol. 136, No. 23, pp. 8277-8282, 2014.

157. X. Zou, J.-M. Goupil, S. Thomas, F. Zhang, G. Zhu, V. Valtchev, and S. Mintova, "Detection of harmful gases by copper-containing metal–organic framework films," The Journal of Physical Chemistry C, Vol. 116, No. 31, pp. 16593-16600, 2012.

158. C. Zong, X. Liu, H. Sun, G. Zhang, and L. Lu, "A new type of nanoscale coordination particles: Toward modification-free detection of hydrogen sulfide gas," Journal of Materials Chemistry, Vol. 22, pp. 18418-18425, 2012.

159. M. Carta, R. Malpass-Evans, M. Croad, Y. Rogan, J. C. Jansen, P. Bernardo, F. Bazzarelli, and N. B. McKeown, "An efficient polymer molecular sieve for membrane gas separations," Science, Vol. 339, No. 6117, pp. 303-307, 2013.

160. U. T. Schwarz, F. Kopp, T. Weig, C. Eichler, and U. Strauss. "Superluminescent light emitting diodes of 100mW output power for pico-projection," Conference on Lasers and Electro-Optics Pacific Rim, Kyoto Japan, Optical Society of America, pp. MH2_3, 2013.

161. L. Sang, M. Liao, and M. Sumiya, "A comprehensive review of semiconductor ultraviolet photodetectors: from thin film to one-dimensional nanostructures," Sensors (Basel), Vol. 13, No. 8, pp. 10482-10518, 2013.

162. M. Wu, Z. Han, and V. Van, "Conductor-gap-silicon plasmonic waveguides and passive components at subwavelength scale," Optics Express, Vol. 18, No. 11, pp. 11728-11736, 2010.

163. N. Clark, A. Vanderslice, R. Grove, and R. R. Krchnavek, "Time-dependent exposure dose of hydrogen silsesquioxane when used as a negative electron-beam resist," Journal of Vacuum Science & Technology B: Microelectronics and Nanometer Structures, Vol. 24, No. 6, pp. 3073, 2006.

164. V. Delft and C. M. J. M. Falco, "Delay-time and aging effects on contrast and sensitivity of hydrogen silsesquioxane," Journal of Vacuum Science & Technology B: Microelectronics and Nanometer Structures, Vol. 20, No. 6, pp. 2932-2936, 2002.

165. Electron Beam Lithography Facility Georgia Institute of Tech IEN. *HSQ resist process*. [Online] Available from: http://nanolithography.gatech.edu/HSQ1.htm [Accessed 2016 06].

# Appendix I.

The fabrication of the SOI sensor chip was done at the U. of Alberta's NanoFAB fabrication and characterization center. Due to the sub-micron dimensions of the silicon waveguides, the chips were fabricated using Electron Beam Lithography (EBL). The fabrication process flow is as shown in Figure I.1 and is described below.

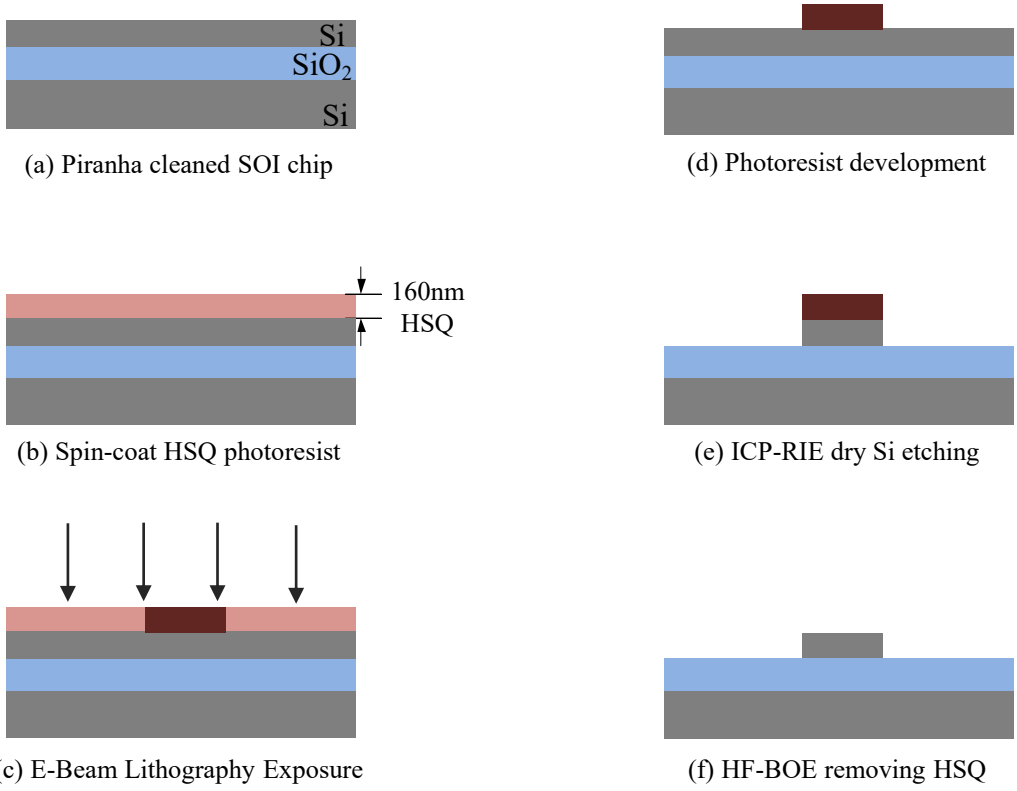


(a) Piranha cleaned SOI chip

(b) Spin-coat HSQ photoresist

(c) E-Beam Lithography Exposure

(d) Photoresist development

(e) ICP-RIE dry Si etching

(f) HF-BOE removing HSQ

Figure I.1 SOI fabrication process for microring resonator sensor chip.

a) **Piranha clean.** A 1cm$^2$ SOI chip was first immersed in a piranha bath ($H_2SO_4 : H_2O_2 = 3:1$) for 20mins to remove organic residues from the surface of the chip. The chip is subsequently rinsed in De-Ionized (DI) water and blow-dried with $N_2$. The actual Si device layer is then measured using Filmetrics Reflectometer to be 210nm, as shown in Figure I.1.

b) **Photoresist coating.** We used hydrogen silsequioxane e-beam photoresist (HSQ, Dow Corning XR-1541 E-Beam resist 6%), which is a negative-toned photoresist widely used for high-resolution EBL fabrication of sub-100nm features. This negative photoresist offers the advantages of shorter EBL write time and better etching resistance compared to the conventionally used positive-toned photoresist PMMA. The resist was let sit in ambient temperature for 30minutes after taken from the storage fridge. The cleaned SOI chip was first prebaked 10minutes at 180˚C on a contact hot plate for surface dehydration. Spin-coating of HSQ was performed at 3000RPM for 35seconds, and followed by a soft-bake procedure (4mins @ 150˚C) The resist layer thickness was measured to be approximately 160nm as shown in Figure I.1 (b).

c) **EBL exposure.** After coating of HSQ resist, the chip is immediately exposed using the Raith-150 Two EBL system at 20kV and 20μm aperture, because HSQ resist is known to be very sensitive to pre-exposure delay in air that changes the exposure dose and contrast [163, 164]. The device pattern was drawn up using the Raith-150 Two mask software. The chip after exposure is as depicted in Figure I.1(c).

d) **Photoresist development.** After exposure, the resist was developed in tetramethyl-ammonium hydroxide (TMAH) 25% solution for 4 minutes at room temperature. This step is followed by rinsing in DI-water with flowing water running into the beaker for 1 minute. The flowing water is important in this step to reduce residue from unexposed HSQ and developer solution [165]. The chip is then rinsed in IPA and dried by gently blowing $N_2$ through the surface. Using this negative-tone resist, the exposed resist remains on the surface for pattern transfer to the Si layer, as shown in Figure I.1(d).

e) **Dry Si etching.** The SOI chip is submitted to dry etching process to transfer the HSQ pattern unto the silicon layer, i.e. the E-beam exposed HSQ serves as a mask protecting the underneath silicon from etching. Dry silicon etching is performed using an Oxford Estrelas Inductively Coupled Plasma Reactive Ion Etching (ICP-RIE) system, which provides anisotropic etch by using both chemical and ion-induced (physical) etching. For dry silicon

etching, a mixture of $SF_6$ and $CF_4$ gases are used as etching precursors. The chip is bonded to a 6" $SiO_2$/Si carrier wafer and loaded on to a helium-cooled chuck table to help prevent heating of the chip surface due to ion bombardment. The etching speed and profile can be controlled by tuning various parameters, including chamber pressure, flow rate and ratio of etchant gases, RF forward and ICP power, and substrate temperature. Using an etch of ~5.8nm/sec, we performed dry etching for 38second to etch through the 210nm-thick Si layer. At this point, the Si photonic structures have been patterned on the chip, but are covered by the exposed HSQ photoresist, as shown in Figure I.1(e).

f) **Photoresist removing.** After E-beam exposure, HSQ becomes similar to $SiO_2$ [80], thus the remaining resist on the etched device can be removed by wet etching using hydrofluoric (HF) acid solutions. Though HF wet etching is isotropic and will etch $SiO_2$ laterally underneath the Si structure from the exposed areas, we have tested a $SiO_2$etch rate of the used HF acid solutions to be ~55nm/min, while a 160nm-thick HSQ residue can be fully removed by BOE in 25 seconds. Therefore, it is still safe to remove the residue resist by a quick-dip in the etchant, because HSQ has a much higher etch rate in HF than $SiO_2$ [165]. After this step, the SOI microring chip is ready for functionalization process and is as depicted in Figure I.1(f).

# Appendix II.

In this appendix, we present the mathematical derivation for the tangential field expression in a chiral medium described in section 4.4.1, with refractive index $n_c$ and chiral parameter $\chi$. Recall that the constitutive relation of a chiral medium is

$$\mathbf{D} = \varepsilon_c \mathbf{E} - j\xi \mathbf{B}, \quad \mathbf{H} = -j\xi \mathbf{E} + \mathbf{B}/\mu_0 , \tag{II-34}$$

where $\varepsilon_c$ is the permittivity of the chiral medium ( $\varepsilon_c = n_c \varepsilon_o$ ), $\xi = \chi \eta_c$ is the chiral admittance ($\eta_c = n_c \eta_0$), and $\mu_0$ is the free space permeability. Consider forward (+$x$ direction) LCP and RCP planewaves propagating in the x-y plane, with electric $E_i(x,y)$ and magnetic field $H_i(x,y)$ dependence of $\exp[-j(\beta y + k_{x\pm} x)]$, where $i = x, y, z$, $k_{x\pm} = \sqrt{k_\pm^2 - \beta^2}$ and $k_\pm = n_\pm k_0$. $n_+$ and $n_-$ are the refractive indices seen by the LCP and RCP plane waves respectively. Substitute Equation (I-1) into the Maxwell curl equations

$$\nabla \times \mathbf{E} = -\frac{\partial \mathbf{B}}{\partial t}, \quad \nabla \times \mathbf{H} = -\frac{\partial \mathbf{D}}{\partial t}, \tag{II-35}$$

We can get

$$-j\beta E_z = -j\omega\mu_0 \left( H_x + j\xi E_x \right), \tag{II-36}$$

$$-j\beta H_z = -j\omega\varepsilon(1+\chi^2) E_x + \omega\mu_0 \xi H_x , \tag{II-37}$$

$$jk_{x\pm} E_z = -j\omega\mu_0 \left( H_y + j\xi E_y \right), \tag{II-38}$$

$$jk_{x\pm} H_z = j\omega\varepsilon(1+\chi^2) E_y + \omega\mu_0 \xi H_y , \tag{II-39}$$

$$-jk_{x\pm} E_y + j\beta E_x = -j\omega\mu_0 \left( H_z + j\xi E_z \right), \tag{II-40}$$

$$-jk_{x\pm}H_y + j\beta H_x = j\omega\varepsilon(1+\chi^2)E_z + \omega\mu_0\xi H_z\,, \tag{II-41}$$

where $\omega$ is the frequency, $E_i$ and $H_i$ ($i = x, y, z$) are the amplitudes of the electric and magnetic field components. Next, we use the above equations to solve for the amplitudes of field components in terms of $E_z$. from Equations (II-3) and (II-4), we can get

$$E_x = \frac{1}{\omega\varepsilon_c}\left(j\beta\xi E_z - \beta H_z\right), \tag{II-42}$$

$$H_x = \frac{1}{\omega\mu_0}\left[\beta\left(1+\chi^2\right)E_z + j\frac{\mu_0}{\varepsilon_c}\beta\xi H_z\right]. \tag{II-43}$$

From Equations (II-5) – (II-6), we have

$$-k_{x\pm}H_z + jk_{x\pm}\xi E_z = -\omega\varepsilon E_y\,, \tag{II-44}$$

together with Equation (II-7), we can get the expression of $H_z$ and $E_y$

$$H_z = -j\chi\eta_c\frac{k_c^2 + k_{x\pm}^2}{k_c^2 - k_{x\pm}^2}E_z\,, \tag{II-45}$$

$$E_y = \frac{k_{x\pm}}{\omega\varepsilon}\left(\pm j\eta_c\sqrt{1+\chi^2} - j\chi\eta_c\right)E_z\,. \tag{II-46}$$

By substituting $H_z$ and $E_y$ into Equation (II-8), we have the expression of $H_y$,

$$H_y = -\frac{k_{x\pm}\sqrt{1+\chi^2}}{\omega\mu_0\left(\sqrt{1+\chi^2}\pm\chi\right)}E_z\,. \tag{II-47}$$

Now if we denote $\eta_c\sqrt{1+\chi^2}$ as $\eta_{ce}$, and let $E_z = E_{1,\pm}^{(c)}$ for forward electric field amplitude, we arrive at the tangential fields of forward CP waves shown in Equation (4.22)

$$\mathbf{E}_{1,\pm\mathrm{T}}^{(c)} = \begin{bmatrix} 1 \\ \pm j\dfrac{k_{x+}}{k_+} \end{bmatrix}E_{1,\pm}^{(c)},\quad \mathbf{H}_{1,\pm\mathrm{T}}^{(c)} = \begin{bmatrix} -\dfrac{k_{x+}}{k_+}\eta_{ce} \\ \pm j\eta_{ce} \end{bmatrix}E_{1,\pm}^{(c)}, \tag{II-48}$$

For backward CP waves propagating in the -*x* direction, the field dependence becomes $E_i(x,y) \sim$ $\beta y - k_{x\pm}x)]$ and $H_i(x,y) \sim$ $\beta y - k_{x\pm}x)]$. By following the math described above and let $E_z = E_{2,\pm}^{(c)}$ for backward electric field amplitude, we will arrive at the tangential fields of backward CP waves shown in Equation (4.23)

$$\mathbf{E}_{2,\pm\mathrm{T}}^{(c)} = \begin{bmatrix} 1 \\ \mp \\ \end{bmatrix} E_{2,\pm}^{(c)}, \quad \mathbf{H}_{2,\pm\mathrm{T}}^{(c)} = \begin{bmatrix} \dfrac{k_{x+}}{k_+}\eta_{ce} \\ \pm j\eta_{ce} \end{bmatrix} E_{2,\pm}^{(c)}, \tag{II-49}$$